Application of Magnetic Resonance Imaging to Investigate New Theranostic Nanomaterials for Drug Delivery in Ischemic Stroke

mgr inż. Kamil Stachurski

Supervisor:
dr hab. Władysław Węglarz, *Institute of Nuclear Physics Polish Academy of Sciences*

Auxiliary supervisor:
dr Krzysztof Jasiński, *Institute of Nuclear Physics Polish Academy of Sciences*

A thesis submitted in fulfilment
of the requirements for the degree of

Doctor of Philosophy

in the
Henryk Niewodniczański Institute of Nuclear Physics
Polish Academy of Sciences

Kraków, 2025

Acknowledgments

Firstly, I would like to express my sincere gratitude to dr hab. Władysław Węglarz and dr Krzysztof Jasiński for their invaluable guidance and support throughout the preparation of this Ph.D. thesis. Without their supervision, this thesis couldn't come true.

I want to express my thanks to my colleagues from the Department of Magnetic Resonance Imaging - dr hab. Barbara Błasiak, dr Katarzyna Kalita, dr Katarzyna Byk, dr Natalia Łopuszyńska and Wojciech Rutkowski for their support and valuable advices.

I want to express my gratitude to my parents Jadwiga and Maciej and grandparents Zofia and Zygmunt for their unwavering support and encouragement throughout my science journey. During difficult moments, you were the source of motivation. Thank you very much.

Last but not least, I would like to express my gratitude to Katarzyna Krupska - my beloved, for being my greatest support and for being here.

My Ph.D. Thesis was prepared during
Cracow School of Interdisciplinary PhD Studies
under grants projects:
GRIEG 1 / TheraforNerv / Norwegian Financial Mechanism
Theranostic nanocarriers for drug delivery in central nervous system disorders
(project nr 2019/34/H/ST5/00578)
and
OPUS 20
Next-generation theranostic nanocarriers for detection, diagnostics and neuroprotective treatment of ischemic brain damage
(project nr 2020/39/B/NZ7/01913)

Table of Contents

List of Abbreviations

- MRI - Magnetic Resonance Imaging
- CT - Computed Tomography
- PET - Positron Emission Tomography
- MR - Magnetic Resonance
- FID - Free Induction Decay
- RF - Radio Frequency
- CEST - Chemical Exchange Saturation Transfer
- MCAO - Middle Cerebral Artery Occlusion
- NMR - Nuclear Magnetic Resonance
- PD - Proton Density
- USG - Ultrasonography
- SPECT - Signle Photon Emission Computed Tomography
- CA - Contrast Agent
- SBM - Solomon-Bloembergen-Morgan Theory
- PRE - Paramagnetic Relaxation Enhancement
- IS - Inner-Sphere
- ZFS - Zero-Field Splitting Interaction
- SNR - Signal-to-Noise Ratio
- PFC - perfluorocarbons
- PGSE - Pulsed Gradient Spin Echo
- DWI - Diffusion-Weighted Imaging
- STIR - Short-TI Inversion Recovery

- DW - Diffusion-weighting
- ADC - Apparent Diffusion Coefficient
- DSC - Dynamic Susceptibility Contrast
- DCE - Dynamic Contrast Enhanced
- ASL - Arterial Spin Labeling
- BBB - Blood-Brain Barrier
- AT - Arrival Time
- TTP - Time to Peak
- NEI - Negative Enhacement Integral
- AUC - Area Under Curve
- MTE - Mean Time to Enhance
- PBP - Percent Baseline at Peak
- PSR - Percent Signal Recovery
- EES - Tissue Extracellular Extravascular Space
- AOT - Dioctyl Sodium Sulfosuccinate
- PLL - Poly-L-lysine Hydrobromide
- PGA - Poly-L-glutamic Acid Sodium Salt
- PEG - Polyethylene Glycol
- NC - Nanocapsule
- PCL - Poly(ϵ-caprolactone)
- DMF - Dimethylformamide
- CQD - Quantum Dots
- POSS - Polyhedral Oligomeric Silsesquioxane

- PBS - Phosphate-Buffered Saline
- PAA - Polyacrylic Acid
- MCA - Middle Cerebral Artery
- ECA - External Carotid Artery
- ICA - Internal Carotid Artery
- CCA - Common Carotid Artery
- FLASH - Fast Low Angle Shot
- MSME - Multi Slice Multi Echo
- CPMG - Carr-Purcell-Meiboom-Gill
- ROI - Region of Interest
- RARE - Rapid Acquisition with Relaxation Enhancement
- VTR - Variable Repetition Time
- FA - Flip Angle
- FOV - Field of View
- fMRI - Functional Magnetic Resonance Imaging
- EPI - Echo Planar Imaging
- MBEST - Modulus-Blipped Echo-Planar Single-Pulse
- DTI - Diffusion Tensor Imaging
- FAIR - Flow-Sensitive Alternating Inversion Recovery
- W-MSA - Window-Based Multi-Head Self Attention
- SW-MSA - Shifted Window-Based Multi-Head Self Attention
- MLP - Multi-Layer Perceptron
- GELU - Gaussian Error Linear Units

- LOD - Limit of Detection
- CSF - Cerebrospinal Fluid

List of Symbols

- L_z - nuclear spin projection on the selected axis
- $\hbar$ - reduced Planck's constant
- m - magnetic spin quantum number
- s - spin quaantum number
- $\overrightarrow{B_0}$ external magnetic field vector
- $\overrightarrow{\mu}$ - magnetic momentum vector
- γ - giromagnetic ratio
- E - energy at a specific energy level
- N_m - distribution of the occupations of energy levels
- N - number of nuclei per unit volume
- k_B - Boltzmann constant
- T - absolute temperature
- $\overrightarrow{M}$ - nuclear magnetization vector
- V - volume of the sample
- $\overrightarrow{L_V}$ - angular momentum vector per unit volume
- $\overrightarrow{\omega}$ - angular velocity vector
- $\overrightarrow{B_eff}$ - effective magnetic field vector
- $\overrightarrow{B_1}$ - RF magnetic field vector
- T_1 - longitudinal relaxation time
- T_2 - transverse relaxation time
- T_2^* - T_2 star relaxation time
- $\overrightarrow{R}$ - relaxation matrix

- $\overrightarrow{M_{eq}}$ - magnetization vector at equilibrium
- t - time
- α - excitation angle, flip angle
- ϵ - electromotive force
- Φ_B - magnetic flux
- V(t) - coil voltage
- F(t) - signal in time domain
- G(ω) - signal in frequency domain
- i - imaginary unit
- $\overrightarrow{G}$ - magnetic field gradient vector
- k_x - x-axis of K-Space
- k_y - y-axis of K-Space
- ϕ_y - phase of transverse magnetization
- ω_x - precession frequency of amgnetic moments on the position along the x-axis
- $\overrightarrow{r}$ - position in the sample
- T_R - repetition time
- T_E - echo time
- S - MRI signal
- ρ - spin density
- r_i - molar relaxivity
- c - concentration
- q - water molecules in the inner-sphere
- k_{ex} - exchange rate

- τ_m - mean residency time of water ligand
- τ_R - rotational correlation time
- S - electron spin
- T_{1e}, T_{2e} - electronic relaxation times
- P_m - mole fraction of bound solvent nuclei
- $\Delta\omega$ - chemical shift difference
- r_{MH} - distance between the metal ion and hydrogen atom
- g_e - electron g factor
- μ_B - Bohr magneton
- μ_0 - vacuum permeability
- τ_v - correlation time for the modulation of the zero-field splitting interaction
- Δ^2 - mean square zero-field splitting energy
- N_A - Avogadro's number
- a - distance of the closest approach of the water molecule and the complex
- V^* - volume fraction
- MTR_{asym} - magnetization transfer asymmetry
- $\overrightarrow{D}$ - diffusion tensor
- η - medium's viscosity
- r - radius of particle
- $\overrightarrow{v}$ - flow velocity vector
- g - diffusion gradient intensity
- δ - duration of diffusion gradient
- Δ - interval time of diffusion gradients

- K^{trans} - influx mass transfer rate
- v_e - tissue extracellular extravascular space
- C_t - concentration in tissue
- C_p - concentration in plasma
- $I(t)$ - signal intensity
- $[H]$ - proton density
- G - ground thruth brain region
- P - image segmentation result
- p - probability
- ϕ_k - GMM component weight
- σ_k - GMM variance
- μ_k - GGM mean
- T_I - inversion time

1 Introduction

The ischemic stroke is one of the biggest challenges of the modern medicine. This is a pathology with high mortality and significant frequeny of occurrence, being one of the main reasons of disability in world. In Europe, the age-standardized incidence of stroke ranges from 95 to 290/100000 per year with monthly mortality rated from 13% to 35%. About 1.1 million people, who live in Europe, suffered a stroke per year and ischemic stroke accounted for about 80% of all cases. It is also worrying that the amount of stroke in young people is still increasing [1]. The Figure 1 below shows annual age-standardized stroke incidence rates in European population-based registries at the beginning of the 21st century.

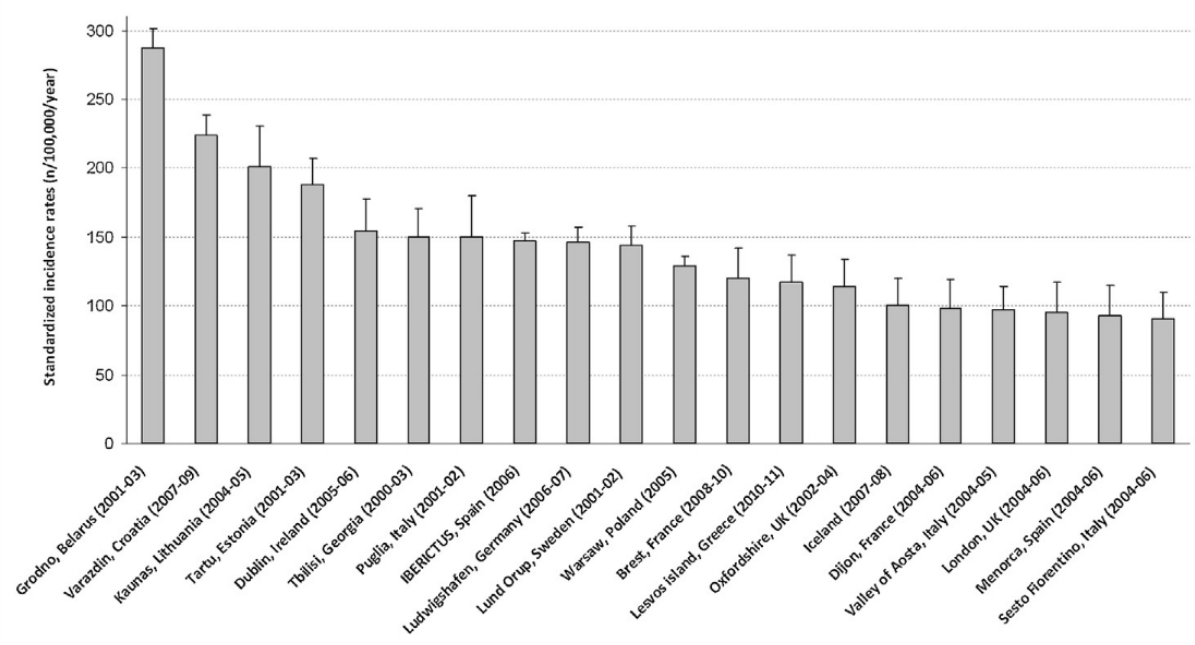

Figure 1: Annual age-standardized (to the European population) stroke incidence rates in European population-based registries at the beginning of the 21st century. Reproduced from [1]. Copyright © 2016.

In recent decades, medicine has made a huge progress in the treatment of ischemic strokes. Introduce of intravenous thrombolysis and mechanical thrombectomy methods lead to significantly improved patient prognosis. The usage of advanced neuroimaging techniques, like magnetic resonance imaging MRI, allows for faster and more precise diagnosis of the ischemic area, which is crucial in the treatment of stroke effects. However, despite big progress in understanding the pathophysiology of ischemic stroke and advances in imaging and therapeutic technologies, treating the effects of stroke is a huge challenge. Effective treatment of stroke symptoms requires rapid intervention, which can be difficult when symptoms are not clear.

What's more, access to specialized facilities with stroke units and rehabilitation may be limited, especially in rural areas. All of these challenges underscore the need for preclinical research in stroke treatment to improve outcomes.

In the ischemic stroke treatment, the worth of considering is targeted therapy. To enable effective action, therapeutic agents should be delivered into their special target, which is the ischemic area in the brain in this case. Integration of nanotechnology and drug design offers nanoplatforms with unique physiochemical properties in stroke. Usage of nanocarriers for drug delivery have some advantages: it prevents rapid degradation of the drug, which results in an extended half-life of the drug in the circulation system, appropriate design of the nanocarrier improves the solubility and stability of neuroprotective drugs and accelerates drug distribution [99]. Delivery of neuroprotective drugs to the brain in the nanoparticle platform can be realized passively or actively. In active targeting, particles are coupled with a ligand element like peptides, antibodies and another small molecules, which can be selectively recognized by specific receptors. On the other hand, passive targeting is accomplished by enhanced permeability and retention effect, where nanoparticles accumulation is increased due to leaky vasculature. At this stage, it is worth to note that nanotechnology offers possibility to combine therapeutic and biomedical imaging agents to overcome the challenges associated with stroke diagnosis and therapy. This combination of diagnostics and therapy on a single nanocarrier platform is called theranostics. Well-designed theranostics enable simultaneous delivery of therapeutics and imaging agents in a single dose with the possibility overcoming differences in biodistribution and selectivity that occur during traditional, two-step procedures. The main effect of the theranostics application is to enable imaging of the anatomy and physiology of diseased tissue, as well as to study kinetics of drug delivery and its efficacy. The most commonly used *in vivo* imaging techniques are CT, MRI and PET. These methods are characterized by different sensitivity and resolution. In the case of MRI, which will be considered in the doctoral dissertation, the observation of the biodistribution of nanocarriers is achieved by attaching contrast agents to the nanocarrier's structure, which modify the relaxation rates of surrounding tissue.

The aim of this doctoral dissertation was to assess the theranostic potential of various nanoparticles designed to deliver neuroprotective drugs in terms of their contrast efficiency for MRI, characterize an animal model of ischemic stroke and its temporal evolution and optimize imaging protocol for biodistribution studies.

The synthesis of nanocarriers for *in vitro* MR studies and *in vivo* stroke characterization was carried out in cooperation between several research groups: the Institute of Nuclear Physics

Polish Academy of Sciences, the Institute of Catalysis and Surface Chemistry Polish Academy of Sciences, SINTEF Industry (Oslo, Norway) the Institute of Pharmacology Polish Academy of Sciences and the Jagiellonian University Collegium Medicum.

The main hypothesis of this work is that it is possible to use MRI imaging to asses efficiency of delivery of the theranostic neuroprotective agents to the tissue affected by the ischemic episode in stroke. To confirm this hypothesis, the MR contrast properties of different nanoparticles were studied. In this case, the contrast properties of different nanoparticles with gadolinium were assessed using MR relaxometry. Moreovwer imaging studies of water phantoms with nanoparticles suspensions were performed to visualize their MRI contrast properties and to determine the optimal sequence parameters. In the case of an animal model, imaging studies of stroke brains were performed to characterize and statistically describe the used model. Biodistribution studies and BBB permeability were also performed using MR imaging.

This doctoral dissertation consists of 10 chapters. The first introduction chapter outlines the research problem. The second chapter described theory of the nuclear magnetic resonance phenomenon. It focuses on aspects such as physics of spin, magnetic moment and magnetization vector. In the next part, it describes the Larmor precession together with the Bloch equations. The final stage of this chapter is the description of the FID signal and the description of RF pulses. The third chapter focuses on the theory of imaging using the phenomenon described in the previous chapter. First, it presents construction of image, the K-Space data matrix and describes the principle of magnetic field gradients. In the rest of this chapter, it describes the method of creating an MR image and image weighting. The fourth chapter is devoted to the theory of MR contrast agents. It describes paramagnetic, superparamagnetic, direct detection agents as well as the CEST agents. Chapters five and six describe the theory of diffusion and perfusion. In the case of clinical diagnosis of ischemic strokes, measurements of diffusion and perfusion in the brain are used. Chapter seven describes the used nanoparticles, as well as the animal model of ischemic stroke MCAO. It also describes the MRI equipment used in this work and used software. The final part of this chapter contains description of used MRI sequences. Finally, chapter eight presents the results of the contrast properties of various nanoparticles of *in vitro* measurements. This chapter also includes a statistical analysis of the MCAO model as well as its time evolution based on the *in vivo* measurements. This chapter also include an analysis of the detection limit of theranostics using MRI, as well as the application of deep learning methodology to extract the brain for future analysis and the optimization of imaging protocol for biodistribution studies. Chapter nine contain discussion of the obtained results

and presents their interpretation. The last chapter ten, the conclusions summarizes the most important results of this doctoral dissertation.

2 Theory of Nuclear Magnetic Resonance

Nuclear magnetic resonance (NMR) is a fascinating physical phenomenon, which occurs, when atomic nuclei with non-zero value of spin selectively absorb electromagnetic radiation of a certain resonant frequency. This absorption happens, when the nuclei are placed in an external magnetic field. The discovery of this phenomenon is credited to Felix Bloch, Edward Purcell and Robert Pound, who made this increadible discovery in 1945 [2].

In 1953, Jacek Hennel obtained the first NMR signal in the Jagiellonian University in Poland using equipment he designed himself. This achievement was a critical milestone in the development of NMR spectroscopy in Poland, which is an essential tool in various scientific fields like chemistry, physics and medicine, especially in imaging.

2.1 Spin Physics

In classical physics, angular momentum is a fundamental property of rotating objects, which characterizes their inertial behavior. It is proportional to angular velocity and moment of inertia. On the other hand, atomic and subatomic particles don't exhibit this property, but instead they have another physical property known as a spin. Nuclear spin is a quantum mechanical property, which describes the intrinsic angular momentum of a particle, which isn't associated with any physical rotation. It is a fascinating phenomenon, which highlights the fundamental differences in the behavior of particles at the atomic scale compared to macroscopic scale [3].

The NMR phenomeon is observed in atomic nuclei with a non-zero value of spin. In short, nuclei with an odd number of nucleons have a non-zero nuclear spin, which allows them to interact with magnetic fields and produce detectable NMR signals. In many atoms, these spins are paired, resulting that nucleus has no overall spin. However, in certain atoms like ^{1}H, ^{13}C and ^{19}F, the nucleus has an overall nuclear spin. The spin projection on the selected axis is quantized, meaning that for the selected coordinate system the allowed values of nuclear spin L in the z-axis direction are equal:

$$L_z = \hbar * m \tag{1}$$

where: $\hbar$ is reduced Planck's constant and m is magnetic spin quantum number, which describes the eigenstate of the atomic nucleus.

The magnetic spin quantum numbers m are related to the spin quantum number s of the nucleus, according to the following relationship:

$$m = -s, -s+1, ..., s-1, s \tag{2}$$

The value of the spin quantum number of the proton s is $\frac{1}{2}$. That means that it's magnetic quantum numbers m have only values $m = 1/2$ and $m = -1/2$. So proton has only two stationary states donated as $|+\frac{1}{2}\rangle$ and $|-\frac{1}{2}\rangle$ and it is known as magnetic dipole [4] [5] [36]. In the Figure 2, energy states of the proton in external magnetic field was presented.

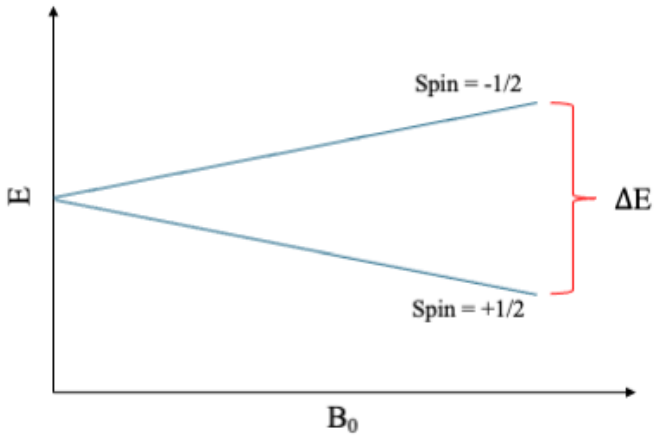

Figure 2: Two magnetic energy states of single proton in magnetic field. Own elaboration.

Some atomic nucleus have a different spin quantum number. The Table 1 below shows some of the these values for some nuclei.

Table 1: Values of net spin for different nuclei. Reprinted from [6].

Nuclei	**Unpaired protons**	**Unpaired neutrons**	**Spin quantum number**
^{1}H	1	0	1/2
^{2}H	1	1	1
^{31}P	1	0	1/2
^{23}Na	1	2	3/2
^{14}N	1	1	1
^{13}C	0	1	1/2
^{19}F	1	0	1/2

Spin is a fundamental property of nature, which is similar to mass and doesn't arise from more basic mechanisms. Unlike classic angular momentum, which interacts with gravitational fields, spin interacts with electromagnetic fields. One of the most important thing to note about nuclear spin is that its magnitude is quantized, meaning it can only take a discrete values [3]. Understanding the basics of spin physics is key to understanding both NMR and MRI.

2.2 Magnetic Moment in External Magnetic Field

The phenomenon of NMR needs to be analysed at the energy level. Initially, the nucleus is in the nuclear ground state. When an external magnetic field $\overrightarrow{B_0}$ is applied, it splits to degenerate $2s+1$ energy levels of the nucleus. When the external magnetic field $\overrightarrow{B_0}$, which determines the quantization axis, is aligned with the z axis of the laboratory coordinate system, the energy of the interaction between the magnetic moment of the nucleus and the external magnetic field can be calculated using the following equation:

$$E = -\overrightarrow{\mu} * \overrightarrow{B_0} = -\gamma \hbar m B_0 \tag{3}$$

where: $\overrightarrow{\mu}$ is magnetic momentum and γ is a giromagnetic ratio, which is characteristic of every atomic nucleus.

When an atomic nucleus is placed in this magnetic field, it causes a phenomenon called Zeeman effect - nuclear splitting. This phenomenom leads to splitting of energy levels, where energy difference can be calculated using a specific relationship [6]:

$$\Delta E = E(m+1) - E(m) = -(m+1)\gamma \hbar B_0 + m\gamma \hbar B_0 = -\gamma \hbar B_0 \tag{4}$$

The Figure 3 below presents the Zeeman effect and allowed energy levels of an nucleus placed in external magnetic field $\overrightarrow{B_0}$, based on the magnetic spin quantum number of the nucleus.

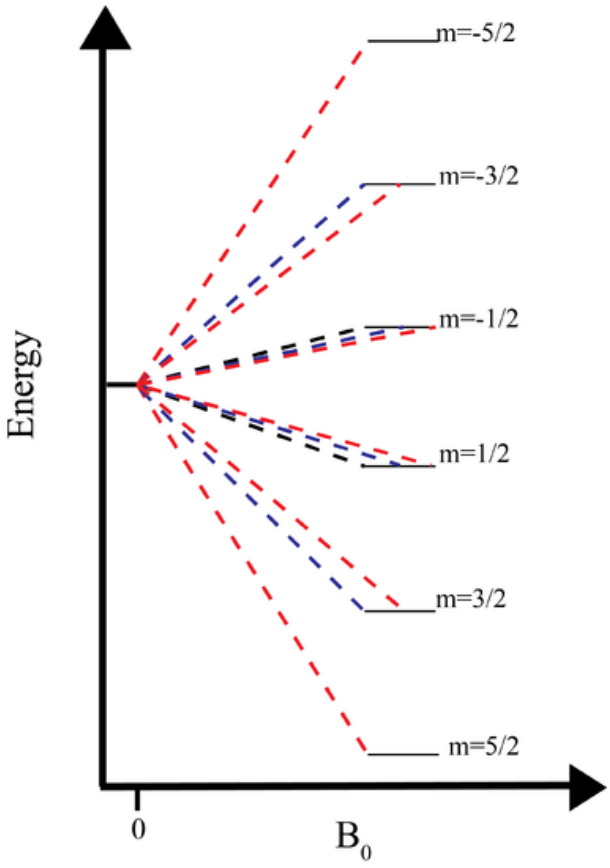

Figure 3: Allowed energy levels for atomic nuclei with different values of magnetic spin quantum number. Reprinted from [6] under a CC By 4.0 license.

2.3 Magnetization Vector

If a sample is in thermodynamic equilibrium with its surroundings, then the occupations of the energy levels will have the Boltzmann distribution. That means that the higher energy levels will be less occupied than the lower energy levels and the distribution of the occupations N_m will be proportional to the exponential of the negative energy divided by the thermal energy:

$$N_m = \frac{N}{2s+1} * exp[-\frac{E_m}{k_B T}] \tag{5}$$

where: N - number of nuclei per unit volume, k_B - Boltzmann constant and T - absolute temperature of the sample. The Figure 4 shows ground and excitated NMR energy levels.

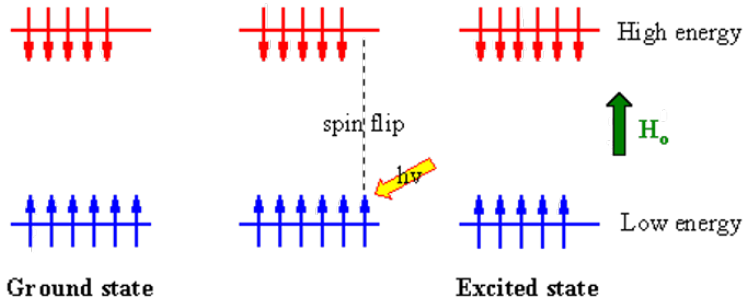

Figure 4: Ground and excited dipole energy levels in NMR. Reprinted from [68].

It is possible to describe the ratio of occupation of energy levels E_1 and E_2 using the following relationship:

$$\frac{N_{E_2}}{N_{E_1}} = exp[-\frac{E_2 - E_1}{k_B T}] \tag{6}$$

The principle of correspondence is a fundamental concept in quantum mechanics and it plays an important role in NMR. This principle relates two physical theories, one of which is a more advanced version of an earlier classical theory. Essentially, it establishes a connection between the classical and quantum mechanical worlds [22]. By applying the principle of correspondence, people can better understand the behavior of atoms and molecules in complex systems. The principle of correspondence helps us describe the magnetic moment of a macroscopic sample in a classical way. Nuclear magnetization vector $\overrightarrow{M}$ represents the net magnetic moment per unit volume of the sample V [23]. The equation of nuclear magnetization is given below:

$$\overrightarrow{M} = \frac{\sum_{n=1}^{n} \overrightarrow{\mu_i}}{V} \tag{7}$$

In the Figure 5, the illustrated definition of net magnetization as averaged sum of spins was presented.

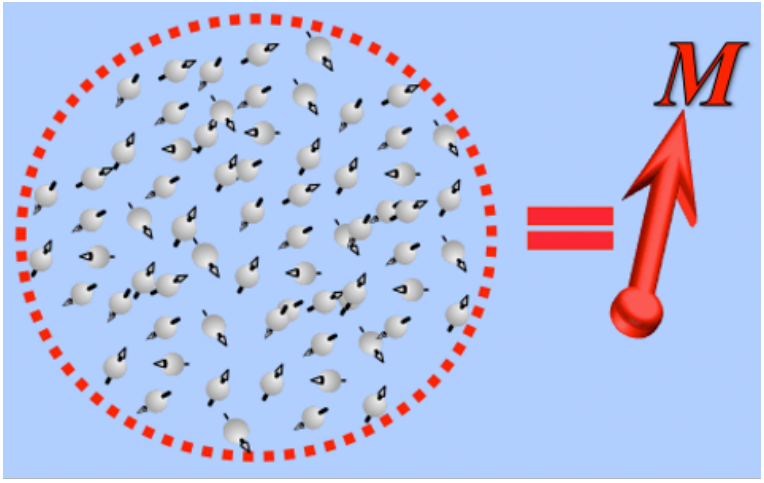

Figure 5: Net magnetization of averaged sum of many individual spins. Courtesy of Allen D. Elster, MRIquestions.com.

When there is no external magnetic field and temperature is absolute zero, the magnetic moments of the nuclei are distributed in all directions, leading to an isotropic distribution. In this situation net magnetization is equal zero. The situation changes when the nucleus is placed in an external magnetic field and a temperature differs from absolute zero. In this case, the magnetic moments of the nuclei begin to precess (also knows as Larmor precession), which will be described in detail in the next section. In the absence of local fields, magnetic moments precess with the same Larmor precession frequency, but they are out of phase. The result is that the magnetization component $\overrightarrow{M_z}$ becomes non-zero, while the components $\overrightarrow{M_x}$ and $\overrightarrow{M_y}$ cancel each other. In a state of thermodynamic equilibrium, the magnetization of the sample is non-zero and directed along the direction of the external magnetic field $\overrightarrow{B_0}$. The Figure 6 shows a distribution of spins in absence and presence of external magnetic field.

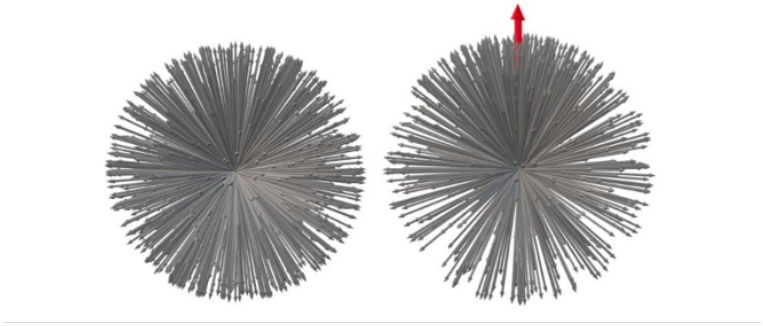

Figure 6: Distribution of spins orientation in the absence (left) and presence (right) of magnetic field B_0. Reprinted from [9].

2.4 Larmor Precession

To have a deep understanding of the phenomenon of NMR, it is essential to delve into the mechanics of Larmor precession. This concept describes the precession of nuclei angular momentum around an external magnetic field. The relation between the magnetization vector and the magnetic moment of the nucleus is described as follows:

$$\overrightarrow{M} = \gamma * \overrightarrow{L_V} \tag{8}$$

where: $\overrightarrow{L_V}$ is the angular momentum vector per unit volume. In turn, the change in angular momentum over time is equal to the torque $\overrightarrow{M}$, according to the principles of classical dynamics. This relationship is presented in the equation below:

$$\overrightarrow{M} = \frac{d}{dt}\overrightarrow{L_V} \tag{9}$$

The motion of the magnetization vector in an external magnetic field can be described mathematically using a differential equation. This relationship looks like this:

$$\frac{d}{dt}\overrightarrow{M} = \gamma\overrightarrow{M} \times \overrightarrow{B_0} \tag{10}$$

It is worth presenting the above equation in a rotating system with angular velocity $\overrightarrow{\omega}$. We assume that the z axis of the laboratory system coincides with the z' axis of the rotating system. This equation takes the following form:

$$(\frac{d}{dt}\overrightarrow{M})' = \gamma\overrightarrow{M} \times (\overrightarrow{B_0} + \frac{\overrightarrow{\omega}}{\gamma}) \tag{11}$$

After introducing a rotating reference system, the magnetization vector interacts with the effective magnetic field:

$$\overrightarrow{B_{eff}} = \overrightarrow{B_0} + \frac{\overrightarrow{\omega}}{\gamma} \tag{12}$$

If the angular velocity of the magnetization vector is equal to the Larmor frequency of precession, the magnetization vector $\overrightarrow{M}$ will be stationary in the rotating reference frame. However, in a laboratory system, the magnetization vector will precess around the direction of the external magnetic field $\overrightarrow{B_0}$. Larmor frequency is equal:

$$\omega_0 = -\gamma\overrightarrow{B_0} \tag{13}$$

where γ is a gyromagnetic ratio, characteristic for each nuclei. In the Table 2 below, some gyromagnetic ratios were presented.

Table 2: Gyromagnetic ratio for some nuclei and particles. Reprinted from [69] [109].

Nucelus or Particle	**Gyromagnetic Ratio γ [MHz/T]**
^{1}H	42.58
^{3}He	-32.43
^{13}C	10.71
^{19}F	40.05
^{23}Na	11.26
^{31}P	17.24
$Electrons$	-28025

In this situation, the equation of motion of the magnetization vector takes the following equation form:

$$(\frac{d}{dt}\overrightarrow{M}) = \gamma\overrightarrow{M} \times (\overrightarrow{B_0} - \frac{\gamma\overrightarrow{B_0}}{\gamma}) \tag{14}$$

Moving to the laboratory reference system allows us to describe the movement of the magnetization vector using three components:

$$\begin{cases} M_x = M_\perp \cos(\omega_0 t) \\ M_y = M_\perp \sin(\omega_0 t) \\ M_z = \text{const.} \end{cases} \tag{15}$$

where $M_\perp$ is the projection of the magnetization vector into the XY plane [2] [7].

2.5 Bloch Equations and Relaxation Process

To observe the NMR signal from a sample, an additional variable magnetic field $\overrightarrow{B_1}$ must be generated with the frequency equal Larmor frequency. This field is perpendicular to the external magnetic field $\overrightarrow{B_0}$ and causes the sample turn out of thermodynamic equilibrium due to the absorption of energy. After the magnetic field $\overrightarrow{B_1}$ disappears, the sample will naturally reback to its original state of thermodynamic equilibrium state. The magnetization vector will start moving around the external magnetic field $\overrightarrow{B_0}$, as per the Bloch's equations that describe the motion of the magnetization vector in a magnetic field. In this situation, relaxation processes take place, including the longitudinal spin-lattice relaxation process and the transverse spin-spin relaxation process, which are described by the relaxation times T_1 and T_2, respectively [8].

In 1946, Felix Bloch proposed a set of equations that describe the time dependence of the net magnetization during an each NMR experiment. These equations are known as the Bloch

equations and they are widely used in the field of NMR. The Bloch equations provide insights into many processes in NMR, like the relaxation of spins and the effects of magnetic field gradients and the behavior of chemical shifts. The equations are essential for understanding the complex behavior of nuclear spins in external strong magnetic fields [6] [7].

As known, net magnetization uses Boltzmann statistics and magnetization vector precessing with this Larmor frequency. Assuming that the magnetic field $\overrightarrow{B_0}$ is along the $z - axis$, it is possible to describe time dependence of the magnetization vector, using equation:

$$\frac{dM}{dt} = \omega(t)xM(t) - [R](M(t) - M_{eq}) \tag{16}$$

where: R is a relaxation matrix and M_{eq} is the magnetization at equilibrium along the $z-axis$. The rotation matrix has information about relaxation processes and it is described by equation:

$$R = \begin{pmatrix} \frac{1}{T_2} & 0 & 0 \\ 0 & \frac{1}{T_2} & 0 \\ 0 & 0 & \frac{1}{T_1} \end{pmatrix} \tag{17}$$

Term on the right side of equation 16 describes decay and growth of magnetization, due to longitudal and transverse relaxation, described by T_1 and T_2 times. Equation 16 in static magnetic field can be extended in each direction:

$$\begin{pmatrix} \frac{dM_x^*(t)}{dt} \\ \frac{dM_y^*(t)}{dt} \\ \frac{dM_z^*(t)}{dt} \end{pmatrix} = \begin{pmatrix} -\omega_0 M_y(t) - \frac{M_x(t)}{T_2} \\ \omega_0 M_x(t) - \frac{M_y(t)}{T_2} \\ -\frac{M_z(t) - M_{\text{eq}}}{T_1} \end{pmatrix} \tag{18}$$

Time dependance will follow an oscillatory pattern which can be described with trigonometric functions. So our magnetization in each direction can be described as:

$$\begin{pmatrix} M_x(t) \\ M_y(t) \\ M_z(t) \end{pmatrix} = \begin{pmatrix} [M_x(0)\cos(\omega_0 t) - M_y(0)\sin(\omega_0 t)]e^{-t/T_2} \\ [M_y(0)\cos(\omega_0 t) - M_x(0)\sin(\omega_0 t)]e^{-t/T_2} \\ M_z(0)e^{-t/T_1} + M_{\text{eq}}(1 - e^{-t/T_1}) \end{pmatrix} \tag{19}$$

where $M_{x,y,z}(0)$ is the magnetization at $t = 0$ [6].

The analysis of Bloch's equations allows us to describe the relaxation processes taking place in the NMR phenomenon. We can distinguish two types of relaxations: T_1 relaxation and T_2 relaxation. T_1 relaxation, which is called as spin-lattice relaxation or longitudinal relaxation, is the process in which the net magnetization $\overrightarrow{M}$ returns to the equilibrium state $\overrightarrow{M_0}$. This

process is described by a T_1 time, reflecting the time it takes for the longitudinal magnetization component $\overrightarrow{M_z}$ recover approximately to 63% of initial value [9]. As the longitudinal component $\overrightarrow{M_z}$ grows toward $\overrightarrow{M_0}$, the energy of the spin system decreases. The energy leaves the spin system and it represents transfer of heat between spins and their external environment. The amount of energy transferred from the nuclei is very small compared to normal molecular kinetic energies, so it is quickly dispersed and goes largely unnoticed at body temperatures [37]. The Figure 7 below shows the reconstruction of the magnetization component $\overrightarrow{M_z}$.

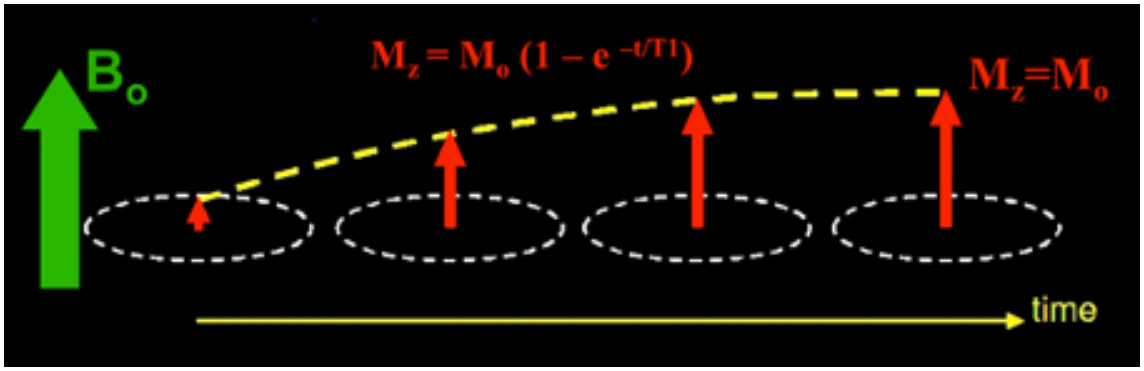

Figure 7: T1 relaxation is the process by which the net magnetiztion (M) returns to its initial maximum value (Mo). Courtesy of Allen D. Elster, MRIquestions.com.

On the other hand, T2 relaxation is known as spin-spin relaxation or transverse relaxation. Transverse relaxation describes the disappearance of the magnetization component $\overrightarrow{M_{xy}}$. The process of this relaxation is based on interactions between individual spins and inhomogeneities of the external magnetic field, which leads to out-phase precession of the spin system and loss of coherence. The parameters characterizing spin-spin relaxation are the times T_2 and T_2^*. The T_2 time depends very little on the field heterogeneity. However, the time T_2^* depends equally on the interactions between the spins and on the measurement parameters, i.e. on the degree of uniformity of the magnet or local field inhomogeneities in the sample. The relaxation time T_2^* is related to the T_2 time by the following relationship:

$$\frac{1}{T_2^*} = \frac{1}{T_2} + \frac{\gamma}{2\pi}\Delta B_0 \tag{20}$$

The Figure 8 below shows a schematic representation of transverse relaxation.

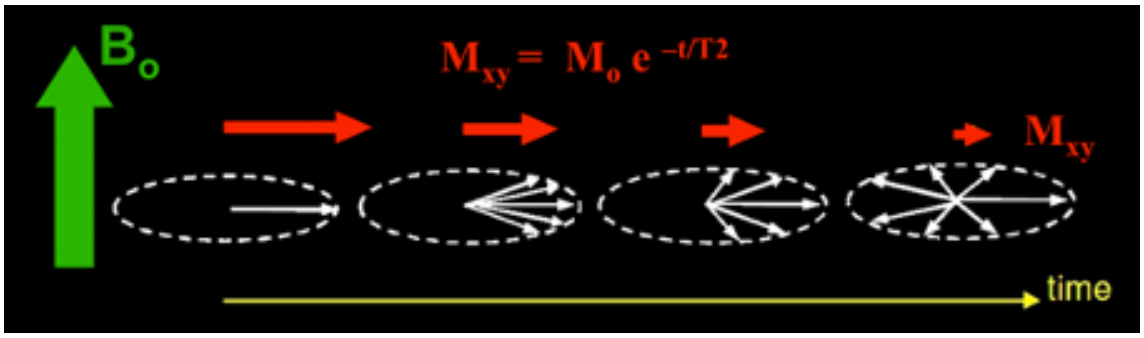

Figure 8: Diagram showing loss of Mxy component of magnetization and T2. Courtesy of Allen D. Elster, MRIquestions.com.

Relaxation processes are a fundamental phenomenon in NMR and understanding them is crucial to understanding the basis of NMR. Bloch's equations make this task easier because they allow the movement of magnetization to be described mathematically [10] [11] [4].

2.6 FID Signal and Fourier Transform

The pulsed method is currently used during NMR nuclear magnetic resonance studies. It involves applying pulses of an alternating magnetic field $\overrightarrow{B_1}$ orthogonal to the external field $\overrightarrow{B_0}$. This action allows to manipulate the behavior of the magnetization vector. The magnetization vector rotates around the $\overrightarrow{B_1}$ field, tracing an angle α in the rotating reference frame, which is directly proportional to the operating time of the $\overrightarrow{B_1}$ field. Selecting the appropriate value of the magnetic field and its operation time allows you to obtain the intended angle of rotation of the magnetization vector. The value of this angle can be calculated using the formula below:

$$\alpha = \gamma B_1 t \tag{21}$$

In order to obtain the maximum amplitude of the received signal, an angle $\alpha = 90^o$ is used. The pulse that tilts the magnetization vector by such an angle is called the $\frac{\pi}{2}$ pulse. This impulse is the basis for many sequences used in both NMR and MRI.

When the magnetic field vector $\overrightarrow{B_1}$ is turned off, the magnetization vector will trace a spiral in the laboratory system, returning to its original position where thermodynamic equilibrium prevails. This situation is presented in the Figure 9 below.

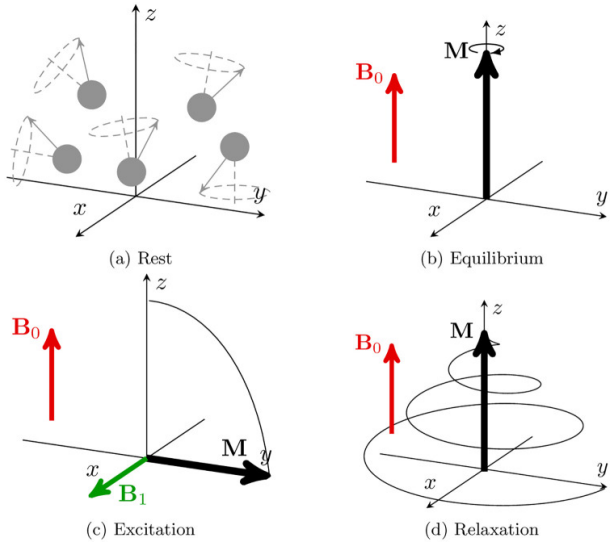

Figure 9: Illustration of the NMR experiment, (a) – no magnetic field is applied, (b) - B_0 field is applied along the z-axis, (c) - RF-excitation is released, (d) – relaxation. Reprinted from [70] under the terms of Creative Commons Attribution License.

According to Faraday's law of electromagnetic induction, a change in the transverse component of the magnetization vector induces an electromotive force in the transmitting and receiving coil. Faraday's law of induction is one of Maxwell's four main equations [80], which can be represented by the following formula:

$$\epsilon = -\frac{d\Phi_B}{dt} \tag{22}$$

where: ϵ is the electromotive force, and Φ_B is the magnetic flux. In this case, the transmitting and receiving coil registers an exponential signal with decay time T_2. This is a signal of the disappearance of free precession FID (Free Induction Decay). The equation describing the FID signal has the following form:

$$V(t) = M_0 * exp[-\frac{t}{T_2}] * \cos(\omega_0 t) \tag{23}$$

A graphical representation of the above function is shown in the Figure 10 below.

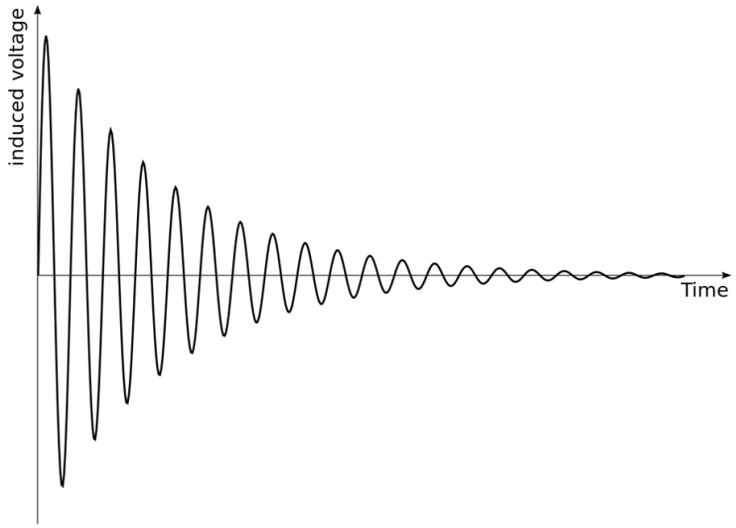

Figure 10: Free induction decay signal. Reprinted from [71] under the CC BY-SA 3.0 license.

The signal above is presented in the time domain F(t). However, when analyzing experimental results, absorption spectra in the frequency domain G(ω) are examined. In order to convert the signal domain from time to frequency, a mathematical operation called the Fourier transform is used. This operation allows to obtain information about the frequency of a given electromagnetic wave. Signals in the time and frequency domains take the following forms [12] [13]:

$$F(t) = \frac{1}{2\pi} \int_{-\infty}^{+\infty} G(\omega) \exp(i\omega t) d\omega \tag{24}$$

$$G(\omega) = \int_{-\infty}^{+\infty} F(t) \exp(-i\omega t)\, dt \tag{25}$$

2.7 RF Pulse

The radiofrequency pulse RF plays an important role in exciting the sample and causing the magnetization vector to deflect from its position in thermodynamic equilibrium. This deflection is achieved by applying a specific induction magnetic field $\overrightarrow{B_1}$, which is always perpendicular to the magnetic field $\overrightarrow{B_0}$. The angle of deflection is directly proportional to the magnitude and duration of the $\overrightarrow{B_1}$ field. By controlling the amplitude, frequency and timing of the RF pulse, it is possible to manipulate the magnetization vector. RF pulses may differ in shape in the time domain. The result, of course, will be a difference in the shape of the pulses in the frequency domain after the Fourier transform. The main shapes used are long rectangular pulse, regular square pulse, Gaussian pulse and sincus pulse. The spectrum of pulses in the time domain and frequency domain used in NMR is presented below on the Figure 11.

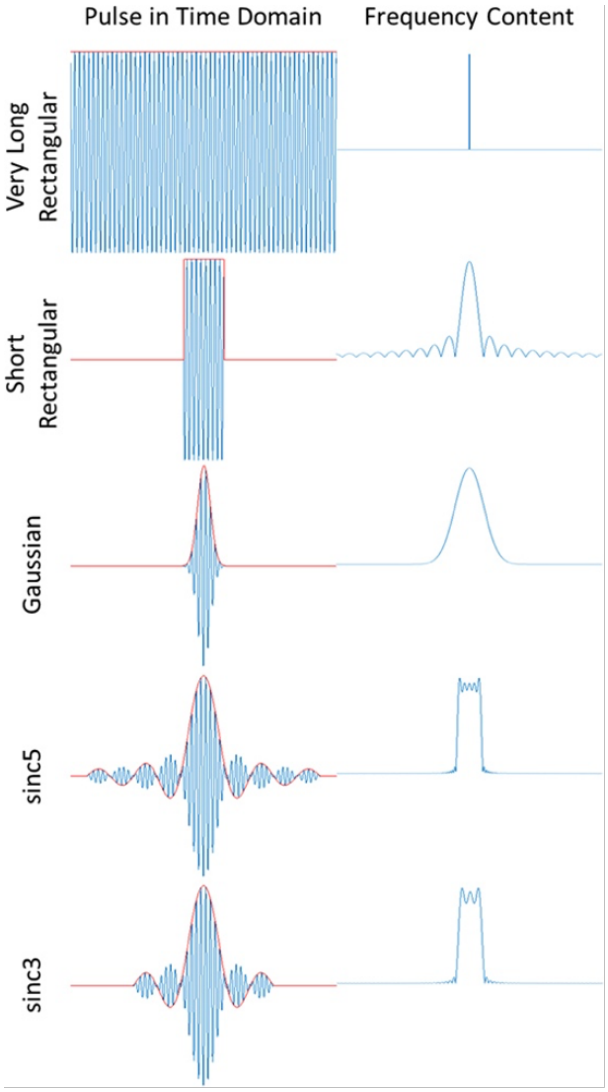

Figure 11: Spectrum of RF pulses in the time domain and frequency domain. Reprinted from [74] with permission of the Morgan & Claypool Publishers.

3 Theory of Magnetic Resonance Imaging

Magnetic resonance imaging (MRI) is a non-invasive imaging technology, which provides detailed anatomical images using nuclear magnetic resonance phenomenon. Unlike computed tomography (CT), MRI doesn't utilize harmful ionizing radiation. The MRI method is particularly useful for imaging soft tissues within the body such as the brain, spinal cord, muscles, ligaments and tendons, which are not clearly visible in plain X-rays and CT scans [14]. Knee and shoulder injuries can be effectively diagnosed using MRI and in the brain case, MRI can distinguish white matter and gray matter and also diagnose aneurysms and tumors. The MRI was invented by two renowned scientists Paul C. Lauterbur and Sir Peter Mansfield [33] [34]. In recognition of their groundbreaking work, both scientists were awarded the Nobel Prize in Physiology or Medicine in 2003 [12]. In 1986, a significant event took place at the Institute of Nuclear Physics Polish Academy of Sciences in Cracow. Andrzej Jasiński was the first person in Poland, who received an MRI image [15] [35]. This revolutionary technology transformed medical imaging in Poland, allowing for more accurate diagnoses and precise treatments. This event marked a turning point in the history of Polish medicine and the impact of this breakthrough continues to be felt today. As we can see, nuclear magnetic resonance is used in many applications, including structural analysis, chemical composition determination and medical imaging.

3.1 Image Contruction

At the beginning, MRI imaging requires to use gradient of magnetic fields generated by specialized gradient coils. These gradient fields are responsible for creating three distinct types of perpendicular magnetic field gradients: the $\overrightarrow{G_z}$ slice selection gradient, the $\overrightarrow{G_x}$ frequency encoding gradient and the $\overrightarrow{G_y}$ phase encoding gradient. These gradients work by inducing a linear change in the external magnetic field $\overrightarrow{B_0}$ relative to a given axis and introduce a corresponding linear change in the resonance frequency [16]. The Figure 12 below shows a graphical representation of the mentioned three different gradients of magnetic field.

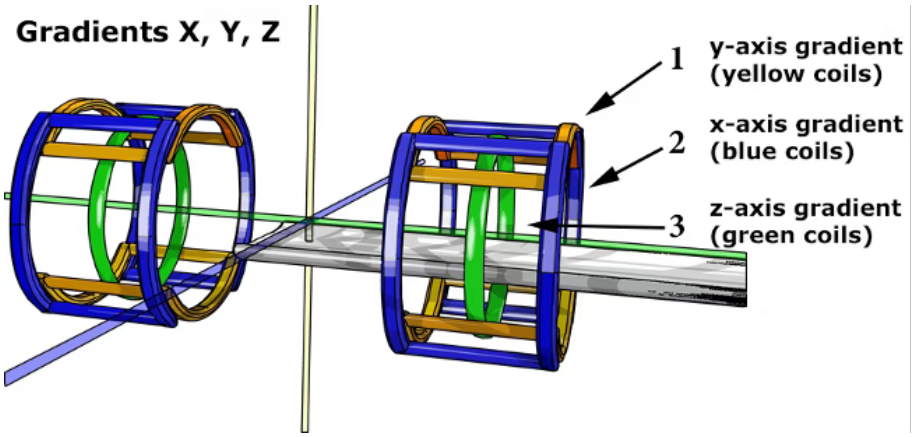

Figure 12: Representation of three different magnetic field gradients used in MRI examination. Reprinted from [72].

3.2 K-Space

Inversion space is a coordinate system used in MRI imaging data. It is represented by a two or three dimensional matrix known as K-Space. This space is used to record spatial frequency information of the examined object in two or three dimensions. The relation between K-Space data and an image data is established through the Fourier transformation. The data acquisition matrix has raw data before image processing. In 2D Fourier transform imaging, a line of data corresponds to the MR signal with specific phase encoding level. The gradient applied across the object determines the position in k-space. By changing the gradient over time, K-Space data are sampled in a trajectory through the Fourier space, which is then used to generate real image [17]. K-Space cells are typically represented on a Cartesian grid with two main axes k_x and k_y. In a 2D image, k_x and k_y axes correspond to the images horizontal and vertical axes. However, it's essential to note that the k-axes represent spatial frequencies not locations. Here's the definition of k_x and k_y:

$$k_x = \frac{\gamma}{2\pi} \int_0^t G_x(t')\, dt' \tag{26}$$

$$k_y = \frac{\gamma}{2\pi} \int_0^t G_y(t')\, dt' \tag{27}$$

Each individual points (k_x, k_y) in the K-Space don't correspond one-to-one with individual pixels in the real image [18]. Each point in K-Space contains information about the spatial frequency and phase of every pixel in the final image. After applying the Fourier transform, it is possible to obtain the mentioned real image [19]. The Figure 13 below presents K-space matrix and real image after Fourier transform.

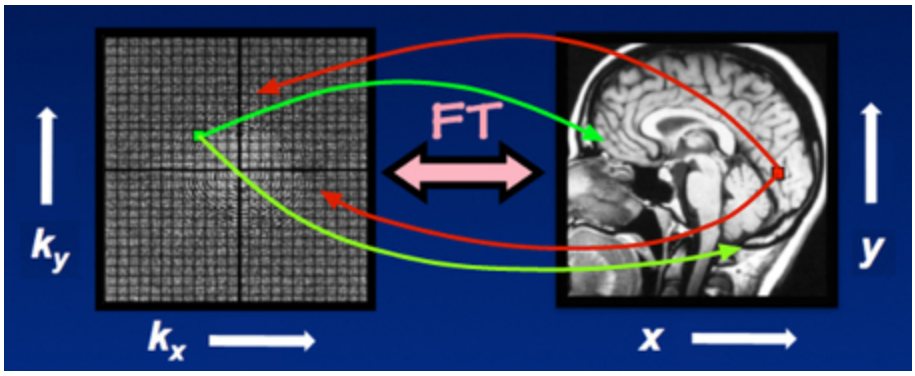

Figure 13: K-space and obtained real image after Fourier transformation. Courtesy of Allen D. Elster, MRIquestions.com.

3.3 Slice Selection Gradient

The images obtained through MRI techniques often show one or multiple slices of the sample being examined. To selected a specific slice, a $\overrightarrow{B_1}$ field pulse is applied at the resonance frequency, while simultaneously applying a $\overrightarrow{B_0}$ magnetic field gradient on the nuclear spin system. This is a slice selection gradient, labelled as $\overrightarrow{G_z}$. This gradient works perpendicular to the measured layer along the longitudinal axis. It introduces a linear dependence of the spin precession frequency along the z axis of the laboratory frame. It's worth noting the fact that $\overrightarrow{B_1}$ pulse of magnetic field contains a range of frequency distributed symmetrically to the resonance frequency $\overrightarrow{\omega_0}$. This magnetic field pulse isn't therefore monochromatic. The pulse of $\overrightarrow{B_1}$ field will cause resonance only for spins located along the z axis, for which the Larmor precession frequency corresponds to the frequencies occurring in the $\overrightarrow{B_1}$ field spectrum. Applying this $\overrightarrow{B_1}$ magnetic field, the magnetic moments of nuclear spins will be deflected only in a specific slice of the measured sample. The thickness of the selected layer is equal to:

$$d = \frac{\Delta\omega}{\gamma G_z} \tag{28}$$

where G_z is layer selection gradient, $\Delta\omega$ is spectral width of B_1 magnetic field. When slice is selected, the layer selection gradient $\overrightarrow{G_z}$ and the $\overrightarrow{B_1}$ pulse of magnetic field are turned off [21]. The Figure 14 below shows the idea of layer selection gradient.

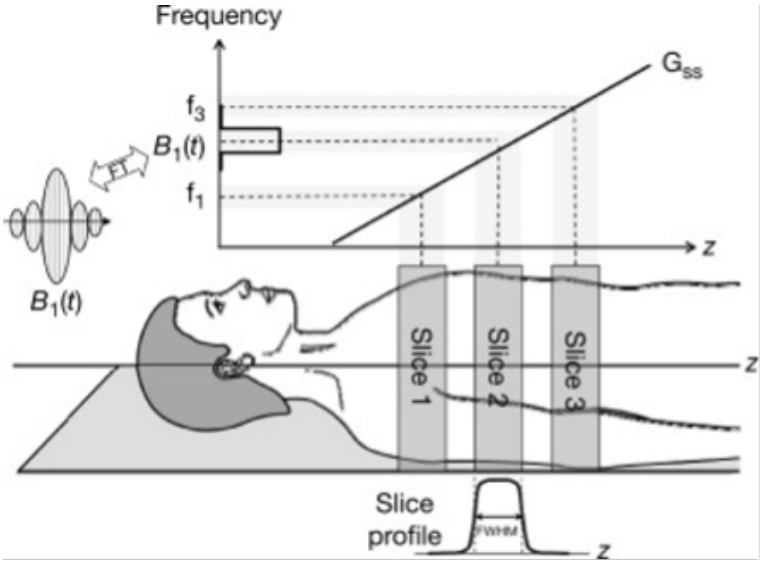

Figure 14: The principle of slice selection gradient. Reprinted from [73], Copyright 2014, with permission from Elsevier.

The next goal is to obtain information about image of the selected slice. The main values to obtain are amplitude and phase of the NMR signal coming from different pixels. Two processes are used to obtain this information, called the phase encoding process and the frequency encoding process.

3.4 Phase Encoding Gradient

In the selected MRI layer, nuclear spins are subjected to an another gradient, which causes a change in the phase of the received NMR signal. To analyse the phase encoding gradient, assume that the phase encoding gradient $\overrightarrow{G_y}$ is applied along the y axis of the laboratory frame (x, y, z), which originates at the isocentre of the magnet. The phase encoding gradient $\overrightarrow{G_y}$ introduces the dependence of the phase ϕ of the transverse magnetization vector versus the position in the y direction of the imaging layer:

$$\phi_y = (B_0 + \gamma G_y)t_y \tag{29}$$

where t_y is a operating time of the $\overrightarrow{G_y}$ gradient. The Figure 15 below shows the principle of the phase encoding gradient [21].

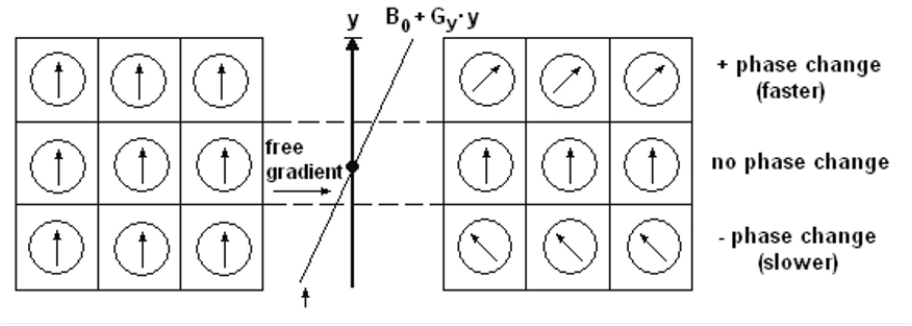

Figure 15: Principle of phase encoding gradient. Reprinted from [75].

3.5 Frequency Encoding Gradient

The frequency encoding gradient, which is also called as the reading gradient is marked as $\overrightarrow{G_x}$. Let's assume that it is applied along the $x - axis$ of the imaged layer. Its task is to introduce the dependence of the precession frequency of magnetic moments on the position along the $x - axis$ direction of the laboratory system [21], in accordance with the following equation:

$$\omega_x = (B_0 + xG_x) \tag{30}$$

The Figure 16 shows the principle of the frequency encoding gradient.

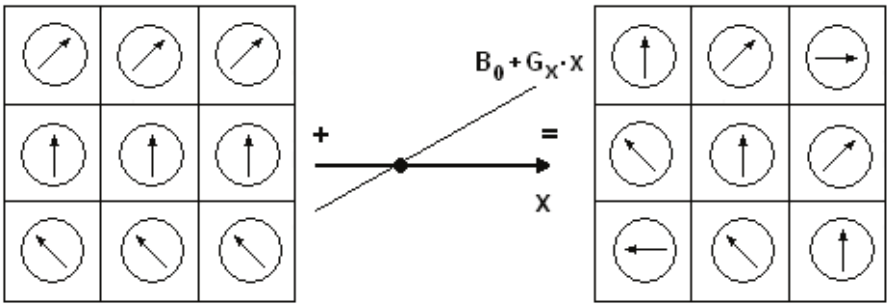

Figure 16: Principle of frequency encoding gradient. Reprinted from [75].

According to the generally accepted agreement, the $\overrightarrow{B_0}$ field works along the z-axis of this system, but the second weak $\overrightarrow{B_1}$ field with Larmor frequency is applied perpendicular to the $\overrightarrow{B_0}$ external magnetic field. They introduce the dependence of the resonance frequency of nuclear spins on their position. The finall static magnetic field, acting on the sample in the z-axis direction has the following value:

$$B = B_0 + \overrightarrow{G} \cdot \overrightarrow{r} \tag{31}$$

where: $\overrightarrow{r} = [x, y, z]$ is a vector describing a position in the sample, while $\overrightarrow{G} = [G_x, G_y, G_z]$ is the gradient, which modifies the original external magnetic field $\overrightarrow{B_0}$. By default, magnetic filed

gradients assume constant values. The shape of the gradient pulses can be any, but it is limited by technical possibilities. The dependence of the Larmor precession frequency on the position is equal:

$$\omega(x, y, z) = (B_0 + G_x x + G_y y + G_z z) \tag{32}$$

The above equation is true only when the direction of the magnetic field gradients coincides with the directions of the laboratory coordinate system [21].

3.6 Creation of MR Image

In the case of MR imaging, the mentioned earlier gradient coils play a key role in MRI. It is a system of three mutually perpendicular coils, each for these of the x, y, z directions. The Figure 17 below shows typical diagram of pulse sequences to two dimensional imaging.

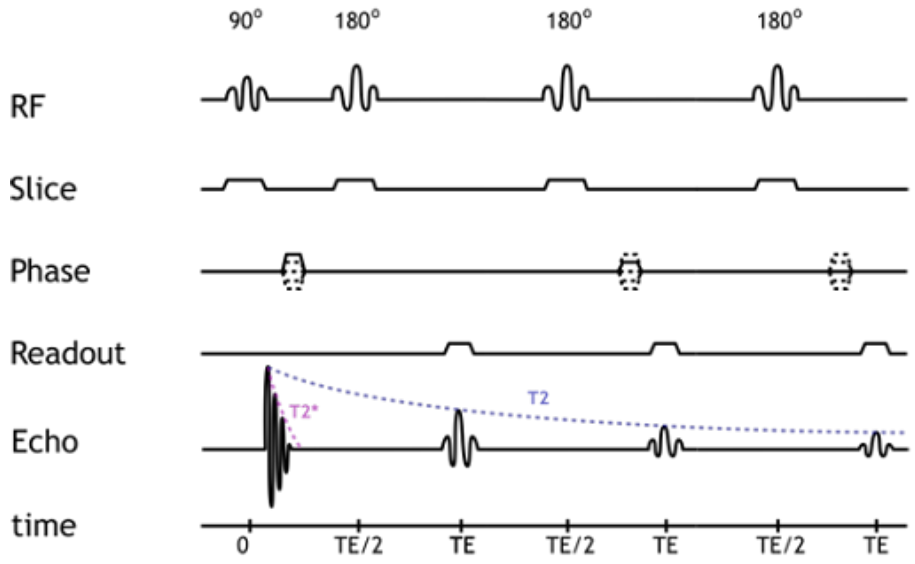

Figure 17: Pulse sequence diagram of two dimensional imaging. Reprinted from [76].

The pulse sequence shown above is typically repeated 128, 256 or 512 times. With each repetition, the amplitude of the phase encoding gradient is changed $\overrightarrow{G_y}$, while the amplitude of the $\overrightarrow{G_x}$ frequency coding gradient has a constant value. The obtained MR signals are subjected to a double Fourier transformation, first in the direction of frequency encoding and then in the direction of phase encoding [21]. The Figure 18 below shows a diagram of creating a tomographic image.

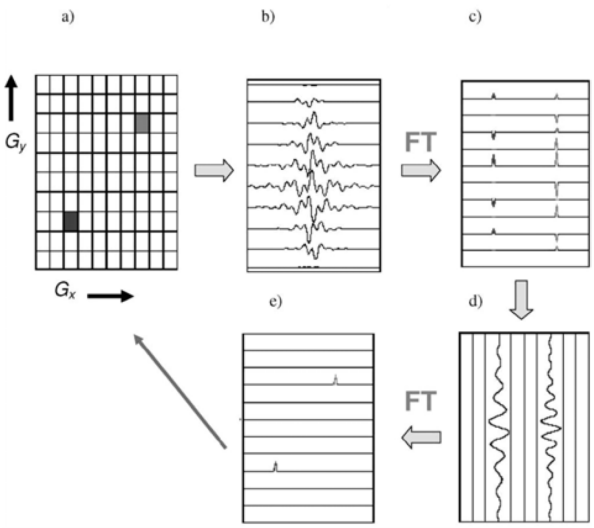

Figure 18: Schematic ilustration of creation MR image. In this example, only two pixels contain protons contributing to the net magnetization (a). For each gradient value G_y, a spin echo signal is recorded during the gradient G_x (b). These data are first Fourier transformed in the direction of frequency encoding. It allows to obtain two series of peaks with frequencies corresponding to the positions of the pixels with spins on the x-axis (c). Their amplitude oscillates in the phase encoding direction, which is better seen when we change the direction of looking at the results (d). Then performing a Fourier transformation in the phase encoding direction and obtaining two maxima, whose positions correspond to the positions of two pixels with spins in the imaged layer (e). Reprinted from [76].

As a result of the double Fourier transform, a tomographic image by changing the intensity of resonance maxima into the intensity of pixels in the image is obtained, which is displayed in shades of gray. The signal with maximum amplitude is assigned the maximum number in the binary representation used, which is white, while the signal with minimum amplitude is assigned the number zero, which is black [21].

3.7 Image Contrast

Magnetic resonance imaging MRI uses a wide range of RF and gradient pulse sequences. The brightness level of each pixel of the final image depends on the intensity of the obtained NMR signal. The brightness of each pixel also depends on two important parameters, repetition time T_R and echo time T_E. The repetition time (T_R) is the amount of time between successive pulse sequences applied to the same slice. On the other hand, the echo time (T_E) represents the time from the center of the RF-pulse to the center of the echo. For pulse sequences with

multiple echoes between each RF pulse, several echo times may be defined and are commonly noted T_{E1}, T_{E2}, T_{E3}, etc. [24] [29]. The Figure 19 below shows the definition of repetition time and echo time.

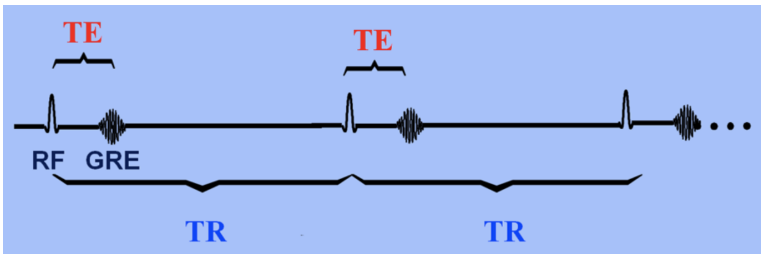

Figure 19: Definition of repetition time and echo time. Courtesy of Allen D. Elster, MRIquestions.com.

The relationship between repetition time, echo time and signal intensity is shown below:

$$S(T_R, T_E) = k\rho(1 - exp[-\frac{T_R}{T_1}])exp[-\frac{T_E}{T_2}] \tag{33}$$

where k is proportionality constant, ρ is spin density.

The selection of appropriate T_R and T_E values makes it possible to highlight the influence of individual parameters such as ρ, T_1 and T_2 in the signal. If we make the signal intensity dependent on one parameter, the influence of other factors will be reduced [29]. This operation allow us to obtain maximum contrast between the imaged tissues. Tissue contrasting includes T_1-weighted imaging, T_2-weighted imaging and proton density imaging. T_1-weighted imaging is obtained for short repetition times and short echo times ($T_R < 500$ ms, $T_E < 30$ ms). T_2-weighted imaging can be obtained for long repetition and echo times ($T_R > 1500$ ms, $T_E > 70$ ms). In turn, proton density imaging is obtained for long repetition times and short echo times ($T_R > 1600$ms, $T_E < 35$ms) [26] [28]. The Figure below 20 presents an example images of T_1-, T_2-wighted and proton density PD images of human brain.

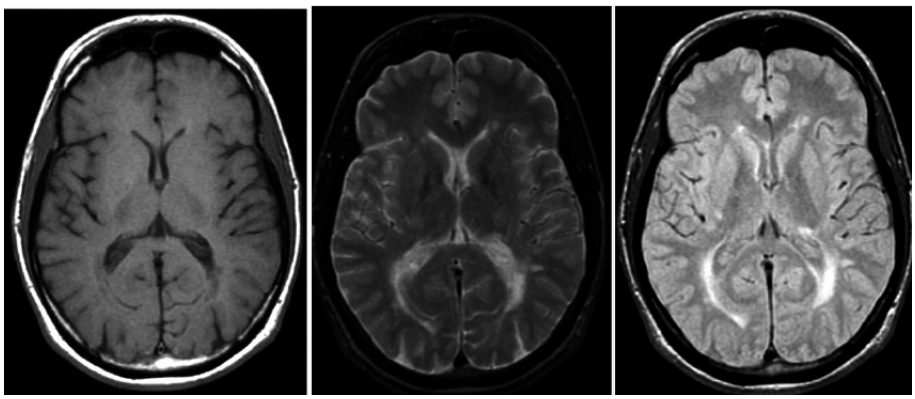

Figure 20: The T_1-, T_2- and proton density weighted axial head scans of a multiple sclerosis patient. Used with permission of SPIE Digital Library, from [61]; permission conveyed through Copyright Clearance Center, Inc.

4 Contrast Agents Theory

To realize the full potential of theranostics, application and understanding of non-invasive medical imaging method is necessary. There are several imaging techniques used in medicine like computed tomography CT, ultrasound USG, positron emission tomography PET, single-photon emission computed tomography SPECT and magnetic resonance imaging MRI. Each of these methods has own unique advantages, limitations and disadvantages. Magnetic resonance imaging has an important advantage of using non-ionizing radiation and making high-resolution tomographic images at any depth in measuring object. However, magnetic resonance imaging technique has limited sensitivity, which leads to insufficient contrast. This problem can be solved by using contrast agents (CAs), to which this chapter is devoted.

Currently available MRI contrast agents may be classified in different ways according to their various features, like the presence or absence of metal atoms, magnetic properties, effects on the magnetic resonance image, chemical structure, biodistribution and application [30] [31].

4.1 Paramagnetic Contrast Agents

The paramagnetic contrast agents are the main type of magnetic resonance contrast agents, because gadolinium-based paramagnetic contrast agents are most often used in clinical applications. In this case, the relaxation in water molecules around the paramagnetic complex e.g. gadolinium complex, is induced by a fluctuating magnetic field, which is generated by the Brownian motion of this complex and is described by the Solomon-Bloembergen-Morgan Theory (SBM) [32] [38] [39] [40]. Related to this theory, the observed relaxation rate of the solvent $(1/Ti)_{obs}$ is the sum of a diamagnetic term $(1/Ti)_d$, which corresponds to the relaxation rate of the solvent nuclei without the contrast agent and the paramegnatic term $(1/Ti)_p$, according to presented equation:

$$\left(\frac{1}{T_i}\right)_{obs} = \left(\frac{1}{T_i}\right)_d + \left(\frac{1}{T_i}\right)_p ; \quad i = \{1, 2\} \tag{34}$$

In this equation above indexes 'd' and 'p' refer to diamagnetic and paramagnetic parts and T_i, where $i = \{1, 2\}$ are spin–lattice (longitudinal) and spin–spin (transverse) nuclear magnetic relaxation times, respectively, described in previous chapter. The important thing is the fact that the paramagnetic contribution is dependent on the concentration of paramagnetic species c. The molar relaxivity r_i, is defined as the slope of the concentration dependence, according to below equation:

$$\left(\frac{1}{T_i}\right)_{obs} = \left(\frac{1}{T_i}\right)_d + r_i \cdot c; \quad i = \{1, 2\} \tag{35}$$

The molar relaxivities r_1 and r_2 directly refer to how effectively the paramagnetic center enhances the relaxation rate of surrounding water protons and contrast efficiency. These are the main metrics, which describe the relaxation and contrast properties of a contrast agent. In equation above, concentration of contrast agent (in this case gadolinium) is given in $mmol/l$, denoted as mM, so the final unit of molar relaxivity is $mM^{-1}s^{-1}$.

The relaxation of water protons arises from the dipole-dipole interactions between the proton nuclear spins and the fluctuating local magnetic field, which has source in unpaired electron spins of paramagnetic centers. There are three separate factors, which have contribution to the relaxation process [38] [39] [41]:

- inner-sphere relaxation;
- second-sphere relaxation;
- outer-sphere relaxation.

The Figure 21 below presents a graphical representation of inner-, second- and outer-spheres, which have contribution in contrast agent relaxivity.

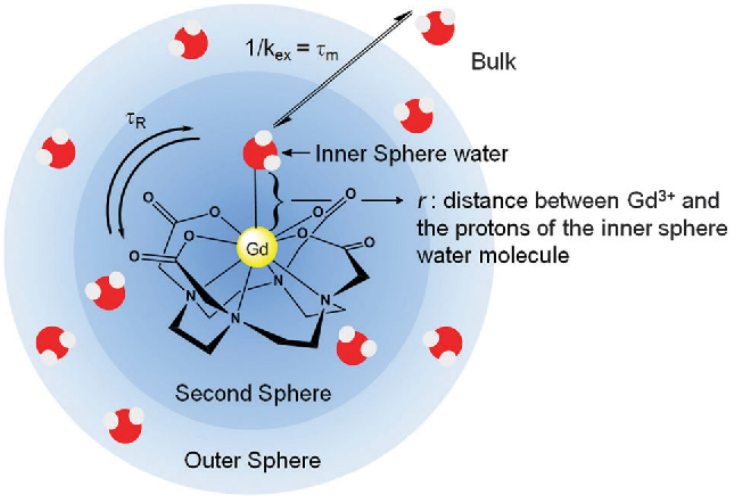

Figure 21: A graphical representation of the contributors in contrast agent's relaxivity. Used with permission of Royal Society of Chemistry, from [48]; permission conveyed through Copyright Clearance Center, Inc.

.

The relaxation of water protons in the inner-sphere occurs, because they are located close to the paramagnetic center. Intra-sphere relaxation involves a water ligand that is directly bound to the metal causing relaxation, which then transmits the effect via exchange with bulk water. In second-sphere relaxation, hydrogen-bonded water molecules in the second coordination sphere

or exchangeable hydrogen atoms (such as O–H, N–H) undergo relaxation and exchange. Lastly, in outer-sphere relaxation, water molecules diffusing near the complex compound also undergo relaxation [31].

Differentiating between second-sphere and outer-sphere is experimentally difficult, so they are often grouped together as outer-sphere. In water solutions, protons exchange between bulk water and the coordination spheres is usually so fast, resulting that the paramagnetic relaxation enhancement is a sum of the inner- and outer-sphere relaxation rates [40]:

$$\left(\frac{1}{T_i}\right)_p = \left(\frac{1}{T_i}\right)_{inner-sphere} + \left(\frac{1}{T_i}\right)_{outer-sphere} ; \quad i = \{1, 2\} \tag{36}$$

MR contrast agents, which contain gadolinium and other metal ions have ability to decrease both T_1 (longitudinal) and T_2 (transverse) relaxation times or increase relaxivities r_1 and r_2 in tissues, where they are accumulated. As mention earlier, this occurs as a result of dipolar interactions between water nuclei in the tissue and the electron spins at the metallic center. This phenomenon is knows as a paramagnetic relaxation enhancement (PRE) [44]. Important fact is that, paramagnetism exhibited by gadolinium-based contrast agents derives from electrons, not protons. Electrons have the same spin values like protons ($\frac{1}{2}$), but they have a much smaller size than protons, so their gyromagnetic ratios are about 657 times larger. If these electrons remain unpaired in shells or bonding orbitals, the unbalanced spins produce a strong magnetic moment capable of inducing magnetic relaxation in the nearest nuclei [46]. The Figure below 22 shows the electron structure of gadolinium atom. There are the 7 unpaired electrons in its 4f subshell, which account for the element's strong paramagnetism of gadolinium.

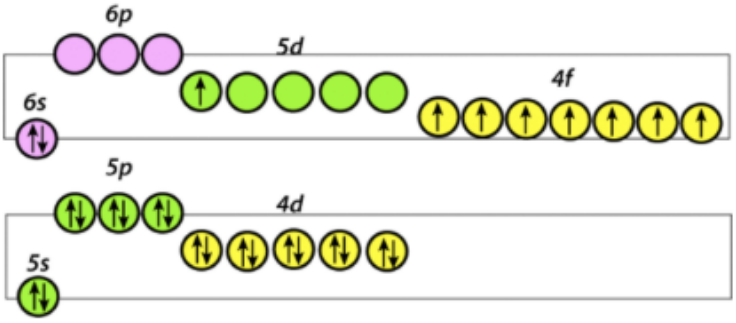

Figure 22: Electron structure of the gadolinium atom. Courtesy of Allen D. Elster, MRIquestions.com.

The above electronic structure of gadolinium allows to draw some conclusions. The ion of gadolinium Gd^{+3} typically has nine coordination sites for bonding and chemical interactions. In clinically available contrast agents, a ligand group accupies eight sites, while the last one,

the ninth is available for transient bonding by a solvent water molecule. Water molecule comes very close to the metallic center and fitting into a crevice of the ligand. This interactions between water and the gadolinium ion are source of earlier mentioned inner-sphere relaxation. However, the gadolinium ion has powerful paramagnetism properties. Therefore, relaxation goes beyond the inner-sphere. Some of water molecules in the second shell are transiently bonded to hydroxyl and carboxyl groups on the surface of the ligand and others are just diffusing by. These molecules are also in continuous in chemical exchange with bulk water much further away. This indirect effect of the gadolinium ion is called the previously mentioned outer-sphere relaxation [44].

4.1.1 Inner-Sphere Relaxation

The inner-sphere relaxation is the first factor, which has contribution to magnetic resonance relaxivity. The inner-sphere contribution to proton relaxivity arises from the chemical exchange of the coordinated water protons with the bulk. The main factors influencing to proton inner-sphere relaxivity are:

1. The number of water molecules in the inner-sphere q;
2. The kinetics of water exchange between the inner-sphere and the bulk, described by exchange rate $k_{ex} = \frac{1}{\tau_m}$, where τ_m is the mean residency time of the water ligand;
3. The rotational dynamics of the molecule, described by a rotational correlation time τ_R;
4. The electron spin S;
5. The electronic relaxation times T_{1e} and T_{2e}.

The equations relating to chemical shift and longitudinal and transverse relaxation rates $1/T_1^{IS}$ and $1/T_1^{IS}$ in the inner-sphere are given:

$$\frac{1}{T_1^{IS}} = \frac{qP_m}{T_{1m} + \tau_m} \tag{37}$$

$$\frac{1}{T_2^{IS}} = qP_m \frac{1}{\tau_m} \left[\frac{T_{2m}^{-1}(\tau_m^{-1} + T_{2m}^{-1}) + \Delta\omega_m^2}{(\tau_m^{-1} + T_{2m}^2)^2 + \Delta\omega_m^2} \right] \tag{38}$$

$$\Delta\omega_{obs}^{IS} = qP_m \left[\frac{\Delta\omega_m}{(1 + \tau_m T_{2m}^{-1})^2 + \tau_m^2 \Delta\omega_m^2} \right] \tag{39}$$

In these equations 'IS' refers to inner-sphere, P_m is the mole fraction of bound solvent nuclei, q is the amount of bound water (or solvent) nuclei per metal ion, τ_m is the mean residency

time of the water ligand. The 'm' index refers to the solvent molecule in the inner-sphere and $\Delta\omega$ refers to chemical shift difference between the paramagnetic complex and a diamagnetic reference [40].

The relaxation of bounded water protons is influenced by the magnetic field-dependent dipole-dipole and scalar interactions. The scalar interaction is affected by electron spin relaxation and water exchange. Its contribution is negligible for T_1 (longitudinal) relaxation. Therefore, the T_1 effect primarily stems from the dipolar contribution, while the T_2 effect arises from both dipolar and scalar interactions [9].

The relaxation rates are described by the SBM equations of paramagnetic relaxation theory. In these equations below, r_{MH} represents the distance between the metal ion and the hydrogen atom, γ_I is the nuclear gyromagnetic ratio, g_e is the electron g factor, μ_B is the Bohr magneton, μ_0 is the vacuum permeability and ω_S and ω_H are the Larmor frequencies of the electron and proton. Factor S is defined as spin quantum number. The factor $\frac{A}{\hbar}$ represents the hyperfine or scalar coupling constant between the electron of the paramagnetic center and the proton of the coordinated water.

$$\begin{aligned}\frac{1}{T_{1m}} = &\underbrace{\frac{2}{15}\left(\frac{\mu_0}{4\pi}\right)^2 \frac{\gamma_I^2 g_e^2 \mu_B^2 S(S+1)}{r_{MH}^6}\left[\frac{7\tau_{C2}}{1+\omega_S^2\tau_{C2}^2}+\frac{3\tau_{C1}}{1+\omega_H^2\tau_{C1}^2}\right]}_{\text{Dipolar coupling}}+\\ &+\underbrace{\frac{2S(S+1)}{3}\left(\frac{A}{\hbar}\right)^2 \frac{\tau_{e2}}{1+\omega_S^2\tau_{e2}^2}}_{\text{Scalar coupling}}\end{aligned} \tag{40}$$

$$\begin{aligned}\frac{1}{T_{2m}} = &\underbrace{\frac{1}{15}\left(\frac{\mu_0}{4\pi}\right)^2 \frac{\gamma_I^2 g_e^2 \mu_B^2 S(S+1)}{r_{MH}^6}\left[4\tau_{C1}+\frac{13\tau_{C2}}{1+\omega_S^2\tau_{C2}^2}+\frac{3\tau_{C1}}{1+\omega_H^2\tau_{C1}^2}\right]}_{\text{Dipolar coupling}}+\\ &+\underbrace{\frac{S(S+1)}{3}\left(\frac{A}{\hbar}\right)^2 \left(\frac{\tau_{e2}}{1+\omega_S^2\tau_{e2}^2}+\tau_{e1}\right)}_{\text{Scalar coupling}}\end{aligned} \tag{41}$$

In these equations, the correlation times, which are characteristic of the relaxation processes are defined as:

$$\frac{1}{\tau_{Ci}} = \frac{1}{\tau_R}+\frac{1}{\tau_m}+\frac{1}{T_{ie}};\quad i=\{1,2\} \tag{42}$$

$$\frac{1}{\tau_{ei}} = \frac{1}{T_{ie}}+\frac{1}{\tau_m};\quad i=\{1,2\} \tag{43}$$

where τ_R is the rotational correlation time, τ_m is the water residency time and T_{ie} is the electronic relaxation time [9]. For protons, the two relaxation mechanisms at work are the dipole-dipole mechanism and the scalar mechanism.

The electronic relaxation rates depend on the strength of the applied magnetic field. For

widely used Gd(III) and Mn(II) complexes, the electronic relaxation times are explained in relation to zero-field splitting interactions (ZFS) [47]. They can be described with the low field limiting value of the electronic relaxation rate by these equations below:

$$\left(\frac{1}{T_{1e}}\right) = \frac{12}{5}\Delta^2\tau_v\left(\frac{1}{1+\omega_S^2\tau_v^2} + \frac{1}{1+4\omega_S^2\tau_v^2}\right) \tag{44}$$

$$\left(\frac{1}{T_{2e}}\right) = \frac{12}{10}\Delta^2\tau_v\left(3 + \frac{5}{1+\omega_S^2\tau_v^2} + \frac{2}{1+4\omega_S^2\tau_v^2}\right) \tag{45}$$

where τ_v is the correlation time for the modulation of the zero-field splitting interaction, Δ^2 is the mean square zero-field splitting energy. Therefore, the electronic relaxation rates decrease with the square of the applied field, and eventually, $\frac{1}{T_{1e}}$ becomes much smaller than $\frac{1}{\tau_R}$, leading to the dominance of the rotation contribution in the overall correlation time [9] [40]. Now, it may be useful to calculate proton relaxation rates as a function of applied magnetic field to show interplay between the various parameters. According to equation 40, two terms inside the square bracket (described as 3 term and 7 term) have magnetic field dependence. The 3 term is a function of the precession frequency, but the 7 term is a function of the electron precession frequency. The difference in gyromagnetic ratios between electrons and protons ($\gamma_S/\gamma_H = 658$) means that $\omega_s^2\tau_{c2}^2$ becomes much greater than 1 at a lower magnetic field than $\omega_H^2\tau_{c2}^2$. At the field where $\omega_S^2\tau_{c2}^2$ becomes greater than 1, the 7 term disperses away to approach zero. The Figure 23 below shows simulated inner-sphere relaxivities as function of applied magnetic field.

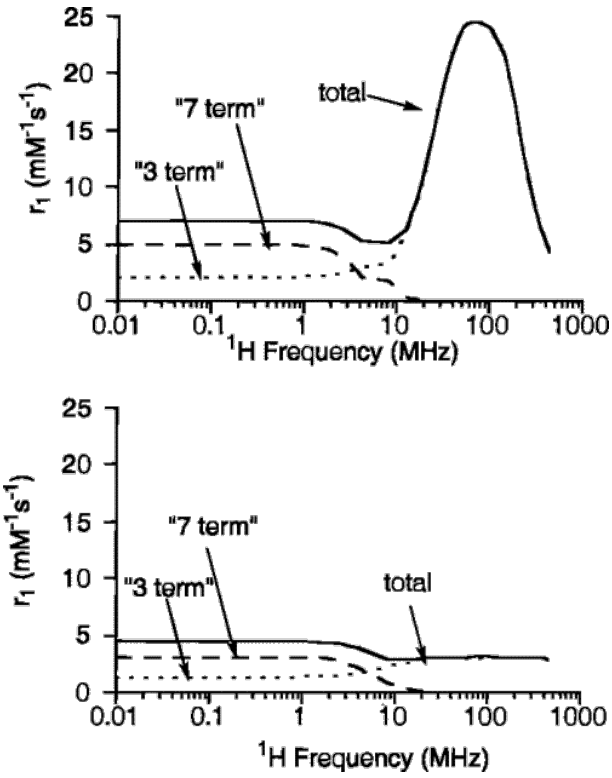

Figure 23: Simulated inner-sphere r_1 relaxivities. In top image $\tau_R = 1$ns, and in bottom image $\tau_R = 0.1$ ns. Reprinted (adapted) with permission from [40]. Copyright 1999 American Chemical Society.

It is interesting to note how increasing the overall correlation times τ_{ci} increases the bound relaxation rate $1/T_{1m}$. The relaxation enhancement will approach a maximum as the inverse of the correlation time $1/\tau_{ci}$ approaches the Larmor precession frequency. [40].

4.1.2 Outer-Sphere Relaxation

Outer-sphere relaxation arises from the translational diffusion of water molecules near the paramagnetic complex e.g. gadolinium complex. The outer-sphere relaxation rates are described as:

$$\frac{1}{T_1^{OS}} = C\left[3j(\omega_I) + 7j(\omega_S)\right] \tag{46}$$

$$\frac{1}{T_2^{OS}} = C\left[2 + 1.5j(\omega_I) + 6.5j(\omega_S)\right] \tag{47}$$

$$C = \left(\frac{32\pi}{405}\right)\gamma_I^2\gamma_S^2\hbar^2 S(S+1)\frac{N_A M}{1000aD} \tag{48}$$

$$j(\omega) = \Re\left\{\frac{1 + \frac{1}{4}\left[i\omega\tau_D + \left(\frac{\tau_D}{T_{1e}}\right)\right]^{1/2}}{1 + \left[i\omega\tau_D + \left(\frac{\tau_D}{T_{1e}}\right)\right]^{1/2} + \frac{4}{9}\left[i\omega\tau_D + \left(\frac{\tau_D}{T_{1e}}\right)\right] + \frac{1}{9}\left[i\omega\tau_D + \left(\frac{\tau_D}{T_{1e}}\right)\right]^{3/2}}\right\} \tag{49}$$

where N_A is Avogadro's number, M is the concentration of the complex, a is the distance of closest approach of the water molecule and the complex, D is the sum of the diffusion constants of water and the complex and τ_D is a diffusional correlation time given by $\tau_D = a^2/D$.

The T_1 relaxation enhancement caused by a paramagnetic complex depends on the quantum spin number as an $S(S+1)$ and inversely on the distance between the metal ion and the water proton. Gadolinium (III) with $S = \frac{7}{2}$ and manganese (II) or iron (III) with $S = \frac{5}{2}$ have been widely studied as contrast agents [42]. However, their ionic forms cannot be used, because they have high toxicity and undesirable biodistribution with accumulation in the spleen, liver and bones. This led to the development of clinically available chelates with high thermodynamic and kinetic stability. Contrast agents based on Gd(II) or Mn(II) chelates typically exhibit similar transverse and longitudinal relaxivities and they are mainly used as a T_1 contrast agents [27] [9]. The Table 3 below shows commercially available contrast agents and their molar relaxivities values obtained in plasma.

Table 3: Molar relaxivities for commercially available gadolinium-based contrast agents obtained in plasma at 37^oC in 1.5 T. Adapted from Ref. [45].

Trade Name	**Chemical Name**	**Mean r_1 $[mM^{-1}s^{-1}]$**	**Mean r_2 $[mM^{-1}s^{-1}]$**
$Magnevist^{TM}$	Gd-DTPA	3.9 - 4.3	3.8 - 5.4
$Gadovist^{TM}$	Gd-DO3A-butrol	4.9 - 5.5	5.2 - 7.0
$ProHance^{TM}$	Gd-HP-DO3A	3.9 - 4.3	4.2 - 5.8
$MultiHance^{TM}$	Gd-BOPTA	6.0 - 6.6	7.8 - 9.6
$Dotarem^{TM}$	Gd-DOTA	3.4 - 3.8	3.4 - 5.2
$Omniscan^{TM}$	Gd-DTPA-BMA	4.0 - 4.6	4.2 - 6.2
$Primovist^{TM}$	Gd-EOB-DTPA	5.4 – 6.2	-

4.2 Superparamagnetic Contrast Agents

While all of the clinically approved contrast agents are based on gadolinium chelates, there is another type of CAs based od superparamagnetic properties. This type of contrast agents mainly affects to T_2 relaxation. It is determined by the translational diffusion of water molecules in the nearest area of unpaired electrons. The relaxation enhacement caused by the presence of superparamagnetic contrast agents are subjected to the outer-sphere SBM theory combined

with the Curie relaxation theory. In this case, the relaxation rate can be described as:

$$\frac{1}{T_2} = \frac{256\pi^2\gamma^3}{405}\frac{V^* M_s^2 a^2}{D(1+\frac{L}{a})} \tag{50}$$

where γ is the gyromagnetic ratio, V^* is a volume fraction, M_s is a saturation magnetization, a is a radius of superparamagnetic core, L is the thickness of a surface coating and D is the diffusion contrast of water molecules.

In absence of the external magnetic field $\overrightarrow{B_0}$, the net magnetization is zero, but in applied external magnetic field, superparamagnetics behave like paramagnets, but with higher susceptibility and therefore higher saturation magnetization. This is the reason, why superparamagnetics are efficient T_2 contrast agents [59] [60]. The Table 4 shows some superparamagnetic contrast agents based on iron oxide.

Table 4: Molar relaxivities of superparamagnetic contrast agents obtaiend in 1.5 T. Adapted from Ref. [45] [49] [50].

Trade Name	**Generic Name**	**Mean r_1 $[mM^{-1}s^{-1}]$**	**Mean r_2 $[mM^{-1}s^{-1}]$**
$Feridex^{TM}$	Ferumoxide	4.2 - 4.8	31 - 35
$Resovist^{TM}$	Ferucarbotran	7.0 - 7.8	86 - 104
$Sinerem^{TM}$	Ferumoxtran	22.5 - 22.9 (at 0.47 T)	49.8 - 56.4 (at 0.47 T)
$Faraheme^{TM}$	Ferumoxytol	17.3 - 20.7	62.6 - 67.2

The superparamagnetic contrast agents described in the table above have been withdrawn from clinical use. They are often used in preclinical studies. Only $Faraheme^{TM}$ is in cinical usage [110].

Magnetic resonance contrast agents can be classified as positive or negative contrast agents. Positive contrast agents shorten the T_1 relaxation time, resulting of brighter signal-enhanced areas on T_1-weighted images. From the other hand, negative contrast agents shorten T_2 relaxation time, resulting darker areas on T_2-weighted images. Positive contrast agents include paramagnetic CAs, because they effectively shorten T_1. Superparamagnetic CAs are considered to be negative contrast agents.

4.3 Direct Detection Contrast Agents

Another group of contrast agents for MRI are contrast agents, which produce detectable signal from nuclei other than hydrogen. As mentioned earlier, every nuclei with a non-zero value

of spin produce MRI signal. However, due to some factors, like natural abundance, relative sensitivity and quadrupolar relaxation, only a few of them have practical meaning for MRI, e.g. ^{13}C, ^{23}Na, ^{31}P, ^{19}F, ^{3}He, ^{129}Xe, ^{15}N, and ^{6}Li [42].

Among the above-mentioned atomic nuclei, the most frequently used direct detection contrast agent is the fluorine ^{19}F. This nucleus has several properties that make it a good candidate for *in vivo* imaging. The gyromagnetic ratio of nucleus ^{19}F has a value close to the gyromagnetic ratio of nucleus ^{1}H (40.09 MHz/T for ^{19}F and 42.58 MHz/T for ^{1}H) [51] [52]. It means that it resonates at a frequency very close to the frequency of ^{1}H, so the standard ^{1}H hardware can be used with some modifications. The sensitivity of fluorine is 0.83, so it is much higher than the sensitivity of other active MR nuclei, such as ^{31}P (0.066), ^{13}C (0.016) and ^{23}Na (0.083) [53]. The nucleus of fluorine does not appear naturally in the human body. It is mainly found in higher concentrations in the bone matrix and teeth, where it is strongly immobilized. Due to this fact, it has a very short spin-spin relaxation time and cannot be detected by conventional MRI. Although using fluorine nuclei for imaging is beneficial, a drawback is the low signal-to-noise ratio (SNR) due to fewer available nuclei compared to standard hydrogen imaging. In hydrogen imaging, approximately 2/3 of the body's nuclei contribute to the final MR signal. To increase SNR, contrast agents containing a high content of fluorine molecules are necessary to ensure sufficient concentration in the tissue [54] [55].

The chemical group compounds, which are the most used in ^{19}F MRI are perfluorocarbons (PFC). Perfluorocarbons have a structure similar to biologically present compounds, like alkenes, with all hydrogen atoms substituted by fluorine [62].

Direct detection contrast agents are also called hot-spot agents. Very often, standard ^{1}H MR images as well as images of a different nucleus with a different resonance frequency are obtained during one imaging session. The image from the nucleus is then superimposed on the ^{1}H image, where the standard MR image is used as a reference for the spatial location of the signal coming from the nucleus with a different resonance frequency, for example fluorine ^{19}F [56]. The Figure 24 below presents implementation of merging ^{1}H and ^{19}F *in vivo* imaging.

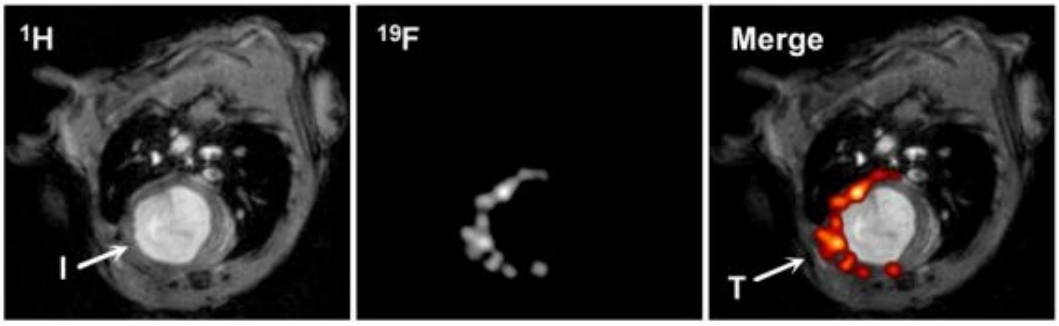

Figure 24: Infiltration of PFCs after myocardial infarction as detected by in vivo ^{19}F MRI as an example of merging imaging. Reprinted (adapted) with permission from [56]. Copyright 2008 Circulation.

4.4 CEST Contrast Agents

Chemical exchange saturation transfer (CEST) provides a new type of contrast for MRI, which is specific to structure of molecules. In this method, a slowly exchanging active NMR nucleus (typically a proton) with a chemical shift different from water is selectively saturated and then transferred to bulk water through chemical exchange [57].

The origins of this go back to the early 1990s, when Balaban and co-workers introduced chemical exchange saturation transfer (CEST) as a new class of contrast agents for MRI [63]. This method is becoming popular due to its appealing features. CEST allows the operator to control the image contrast by using an RF pre-saturation pulse. Since chemical exchange can be sensitive to the contrast agent's environment, the CEST effect can be used to image important physiological parameters, such as pH and metabolite levels [64] [65].

The CEST mechanism operates based on the presence of solute protons, which resonate at a different frequency than water and participate in a chemical exchange process. During this process, a proton moves back and forth between the solute and the solvent. Selective radiofrequency (RF) pulses are used to saturate the exchangeable proton pool at the solute's resonant frequency. This saturation is then transferred to the bulk water through chemical exchange, leading to a reduction in the water signal. The operating diagram of the CEST mechanism is shown in the Figure 25 below.

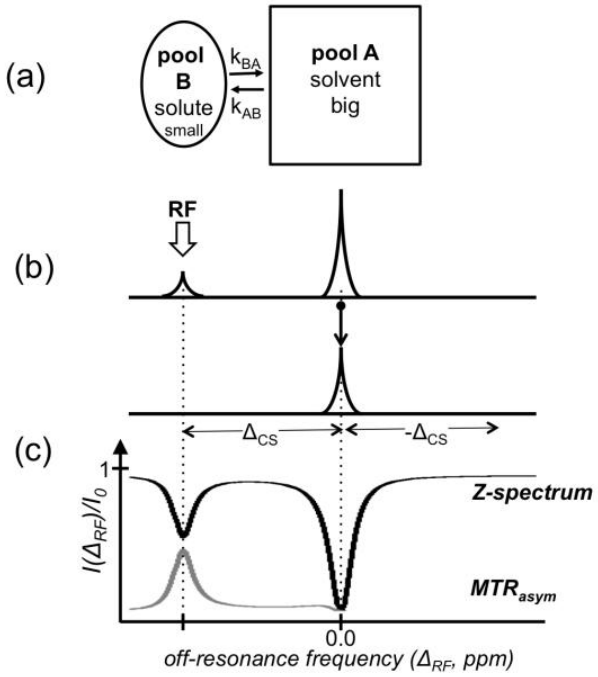

Figure 25: Schematic CEST experiment. Reprinted from [57] Copyright (2012), with permission from Elsevier.

In the figure above, part (a) shows the process of solvent (pool A) exchanging with the solute (pool B), while part (b) presents the chemical shifts with a difference of Δ_{CS}. In this scenario, RF is applied on-resonance with pool B, leading to saturation transfer and a signal decrease of pool A. Part (c) shows the plot of the normalized water intensity (I/I_0) against the off-resonance frequency of the saturating RF (Δ_{RF}). The water resonance is given a 0 ppm value. The MTR_{asym} represents the Z-spectrum asymmetry plotted against the RF off-resonance value [57]. This metric will be described later.

The solute typically has a low concentration and is undetectable in the standard MR signal. However, continuous saturation transfer allows for amplification, enabling the indirect observation of solutes at low concentrations [58].

When conducting CEST analysis, the metric that is frequently utilized is the magnetization transfer asymmetry MTR_{asym}. This metric is defined as:

$$MTR_{asym}(\Delta_{CS}) = \frac{I(-\Delta_{CS}) - I(\Delta_{CS})}{I_0} \tag{51}$$

where $I(\Delta_{CS})$ and $I(-\Delta_{CS})$ are signal intensities are acquired with RF irradiation applied on-resonance with the exchanging pool and at the frequency symmetric around water. On the other hand, I_0 represents the reference signal intensity acquired without RF pre-saturation [57].

The most common classificiation of CEST contrast agents includes below groups: DiaCEST,

ParaCEST, exogenous CEST agents using liposomes lipoCEST and CEST agents using hyperpolarized gases hyperCEST [57]. For DiaCEST, the difference in chemical shift is in range of 0 - 5 ppm [66]. The relatively small difference in chemical shift of DiaCEST agents is their main drawback, causing partial saturation of the signal from a bulk water pool. Additionally, it indicates the need for very slow exchange rates. This issue can be resolved by enhancing the chemical shift separation between the two exchanging pools through the use of ParaCEST agents. In ParaCEST agents, the difference is in range of +500 to -720 ppm with respect to the resonance frequency of water [67].

5 Diffusion Theory

This chapter provides fundamental information concerning diffusion measurements using MRI methodology.

Diffusion is the random movement of water molecules caused by thermal energy. German physicist Adolf Fick modeled diffusion as the movement of particles from an area of high concentration to an area of low concentration. Fick demonstrated that the flux of particles during diffusion is directly proportional to the concentration gradient, with a factor D representing the diffusion coefficient. The unit of diffusion coefficient is mm^2/s. Additionally, Albert Einstein developed a comprehensive mathematical theory to explain Brownian motion and incorporate Fick's laws of diffusion. His approach involved modeling the process as a statistical random walk with a Gaussian distribution. Einstein also integrated George Stokes' principle of fluidic friction into his theory, resulting in the Stokes-Einstein equation. This equation illustrates that the diffusion coefficient D is directly proportional to the absolute temperature T and Boltzmann constant k_B, while being inversely proportional to the particle's radius r and the medium's viscosity η.

$$D = \frac{k_B T}{6\pi r \eta} \tag{52}$$

In a fluid, diffusion occurs equally in all directions and can be represented by a single diffusion coefficient D. These materials are referred to as isotropic. However, biological tissues are anisotropic, because they have varying diffusion coefficients along different directions. In such materials, diffusion is described using a diffusion tensor, where the diagonal elements depict diffusion along each principal direction and the off-diagonal terms reflect the correlation between random motions corresponding to each pair of directions.

In diffusion measurements, individual elements of the diffusion tensor are calculated by measuring phase dispersion and signal loss due to diffusion-sensitizing gradients, which are applied in various directions. However, this method detects signals from several processes too. As a result, the measured diffusion depends on the nature of the media studied and the experimental conditions. To distinguish different processes from diffusion, the apparent diffusion coefficient ADC was introduced. It represents the mean diffusion in a voxel and is calculated by summing or averaging the diagonal elements of the diffusion tensor.

Diffusion sequences allow the acquisition of diffusion weighted images using the Pulsed Gradient Spin Echo PGSE technique developed by Edward Stejskal and John Tanner. The sequence scheme is shown in Figure 26 below.

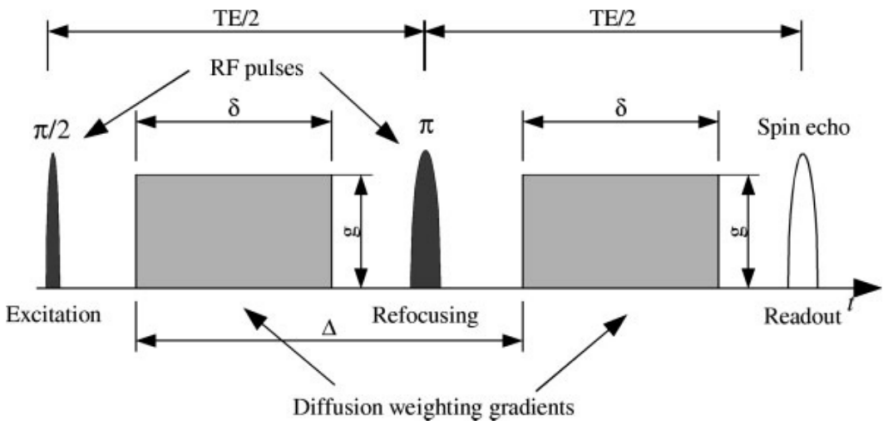

Figure 26: The PGSE sequence. For the idealised case of rectangular gradient pulses, g represents gradient intensity, δ represents gradient duration and Δ represents gradient spacing. Reprinted from [83] under the terms of the Creative Commons Attribution License.

When applied strong, symmetric diffusion-sensitizing gradients on either side of the π pulse, stationary spins are not affected because the phase accumulation from the first gradient is reversed by the second. However, diffusing spins move to different locations between diiferent magnetic field due to the gradients, causing them to fall out of phase and lose signal. After the second gradient, the image acquisition module is typically a fast echo-planar sequence. To prevent chemical shift artifacts, all diffusion-weighted imaging DWI sequences use some form of fat suppression method, such as a chemically-selective fat saturation pulse or a nonselective STIR-like inverting pulse applied immediately before the $\pi/2$ pulse. Alternatively, the $\pi/2$ pulse itself may be selectively tuned to excite water protons only.

To generate DW images and their maps, the following steps are performed. Firstly, the DW pulse sequence is run with the diffusion gradients turned off or set to a very low value. This generates a set of $b0$ images, which are T_2-weighted and serve as a baseline for later calculated maps. Secondly, the DW sequence is then run with the diffusion gradients turned on individually or in combination and at various strengths, producing DW source images sensitized to diffusion in multiple different directions. Thirdly, the DW source images are combined to produce a set of Trace DW images, which are the first-line images used for clinical diagnosis. Fourthly, an Apparent Diffusion Coefficient (ADC) map is then calculated using the data from the b0 and source DW images. The ADC map is used to clarify abnormalities seen on the trace images. Finally, further advanced processing can be optionally performed, creating additional calculated image sets for analysis. These may include exponential ADC maps, fractional anisotropy images, principal diffusion direction maps and fiber tracking maps [84].

The mathematical description of the effect of diffusion phenomenon on NMR signal uses the traditional Bloch equations, with some modification introduced by Torey. Hence the name of this equation is the Bloch-Torrey equation:

$$\frac{\partial \overrightarrow{M}}{\partial t} = \gamma \overrightarrow{M} \times \overrightarrow{B} + \begin{pmatrix} -\frac{1}{T_2} & 0 & 0 \\ 0 & -\frac{1}{T_2} & 0 \\ 0 & 0 & -\frac{1}{T_1} \end{pmatrix} \overrightarrow{M} + \begin{pmatrix} 0 \\ 0 \\ \frac{M_0}{T_1} \end{pmatrix} - \nabla \cdot \overrightarrow{v} \overrightarrow{M} + \nabla \cdot \overrightarrow{D} \nabla \overrightarrow{M} \tag{53}$$

where $\overrightarrow{M}$ represents the magnetization vector, $\overrightarrow{B}$ is an external magnetic field, T_1 is the longitudinal relaxation time, T_2 is transverse relaxation time, M_0 is the thermal equilibrium magnetization, $\overrightarrow{v}$ is the flow velocity and finally $\overrightarrow{D}$ is the rank-2 diffusion tensor. The effect of the diffusion term is to introduce signal attenuation. Exist the linear relationship between precesion rate and the magnetic field. The first diffusion pulse introduce dephasing:

$$\Phi_1 = \gamma \int_0^{\delta} gxdt = \gamma g \delta x \tag{54}$$

while the second pulse introduce rephasing:

$$\Phi_2 = \gamma \int_{\Delta}^{\Delta+\delta} gx'dt = \gamma g \delta x' \tag{55}$$

where γ is gyromagnetic ratio [83].

In a PGSE sequence a time-dependent diffusion-weighting gradient $\overrightarrow{g}(t)$ is applied, spins are subject to a magnetic field:

$$\overrightarrow{B}(\overrightarrow{r}t) = (0, 0, \overrightarrow{g}(t) \cdot \overrightarrow{r}) \tag{56}$$

where $\overrightarrow{r}$ is the spin displacement vector.

To describe the diffusion weighting strength, a quantity called b-value is used. The b-value reflects the strength and timing of diffusion gradients. A higher b-value indicates stronger diffusion effects. The signal after applying diffusion gradients is given by:

$$S = S_0 exp[-b \overrightarrow{u}^T \overrightarrow{D} \overrightarrow{u}] \tag{57}$$

where $\overrightarrow{u}$ is the unit vector corresponding to the direction of the diffusion-sensitizing gradient, S is a signal after applying diffusion gradients, and S_0 is signal befor applyint these gradients. Two strong, rectangular gradient pulses of magnitude g and duration δ, separated by time interval Δ, allow to describe b-value as [83]:

$$b = \gamma^2 \delta^2 g^2 (\Delta - \frac{\delta}{3}) \tag{58}$$

The optimal choice of b-value is not clearly defined; it depends on magnetic field strength, signal averages, anatomical features and pathology. Figure 27 below shows human brain DW images with different b-values.

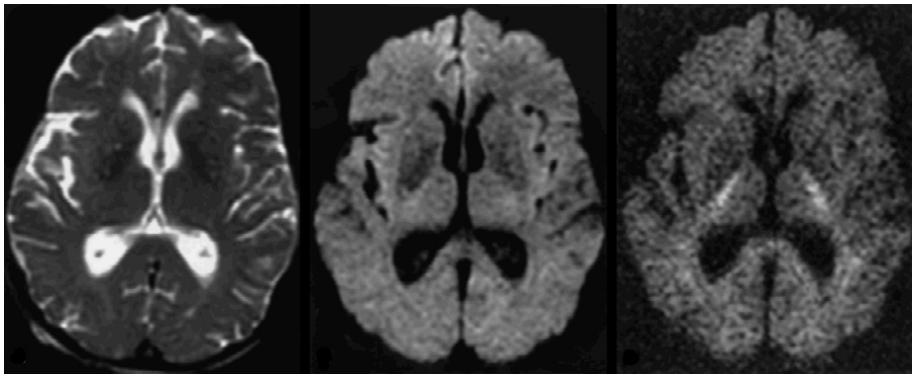

Figure 27: Brain diffusion weighted images using different b-values. First image b-value is 0 s/mm^2, second 1000 s/mm^2, and third 3000 s/mm^2. Courtesy of Allen D. Elster, MRIquestions.com.

Consecutive images present more diffusion weighting and also more noise. As a practical matter, most routine clinical DWI currently use b-value between 0 and 1000 s/mm^2 [84].

6 Perfusion Theory

In the *in vivo* studies performed as part of the doctoral dissertation, perfusion measurements were also carried out.

Perfusion refers to the rate of blood flow through the capillary circulation of an organ or tissue. To account for differences in organ size, perfusion is often expressed as the bulk blood flow rate (in mL/min) divided by the mass of the organ (in grams) and reported in units of $mL/min/100g$. Perfusion varies among organs and can change in response to pathology or metabolic needs. Measurement of perfusion involves the use of tracers, which are molecules, molecular aggregates or small particles, which distribute in tissues according to blood flow and can be detected.

In perfusion measurements, it is possible to use three MRI methods:

- Dynamic Susceptibility Contrast (DSC)
- Dynamic Contrast Enhanced (DCE)
- Arterial Spin Labeling (ASL).

The DSC and DCE methods require intravenous bolus administration of gadolinium-based contrast agent. On the other hand, the ASL method is performed without exogenous contrast.

Perfusion imaging using DSC involves injecting gadolinium chelate into a vein, followed by quickly capturing gradient or spin echo images of the organ under study. Initially, the gadolinium stays within the blood vessels as it moves through the local circulation. Due to its paramagnetic properties, gadolinium distorts the local magnetic field around the vessels, causing T_2 (T_2^*) dephasing and a loss of signal as it passes through. By measuring the signal intensity over time and using a mathematical model, various perfusion parameters such as blood volume, blood flow and mean transit time can be calculated.

In DCE imaging, a gadolinium-based contrast agent is injected into the bloodstream. DCE uses the T_1 shortening effects of gadolinium by capturing repeated T_1-weighted images. This allows the contrast agent to accumulate in the extracellular space of tissues, with the accumulation rate depending on perfusion, capillary permeability and surface area. The resulting image data can be analyzed visually or semiquantitatively. Full quantification involves using a compartmental model to calculate various physiological parameters such as the transfer constant (K^{trans}), fractional plasma volume (v_p) and fractional volume of the tissue extracellular space (v_e).

ASL imaging does not require the use of gadolinium contrast. Instead of using external contrast, the patient's own water molecules are used as a natural tracer. This is achieved by labeling water molecules in nearby blood vessels using radiofrequency pulses. As these labeled molecules flow into the organ being studied, they decrease the signal intensity in the tissue in proportion to the blood flow. In a typical ASL imaging process, images are taken with and without the labeling pulses and then the two sets of images are subtracted. Using a mathematical model, various perfusion parameters, mainly blood flow, can be calculated. ASL imaging works significantly better at 9.4 T than at 3.0 T or 1.5 T due to its signal-to-noise limitations.

Gadolinium-based contrast agents usually cannot pass through the extracellular spaces of the brain and spinal cord because they are blocked by the blood-brain barrier (BBB). The BBB is composed of tight junctions between endothelial cells, which only permit the passage of ions and small molecules (such as O_2) through the vessel wall. However, if the BBB is compromised due to conditions like malignant tumors or stroke, the contrast agents may go into the brain tissue, leading to T_1 shortening and signal enhancement.

A variety of semi-quantitative perfusion parameters can be calculated by analyzing DSC signal intensity curves for each voxel as the contrast bolus passes through. These parameters are widely used because they are simple to calculate. The most common parameters are illustrated and defined below on the Figure 28.

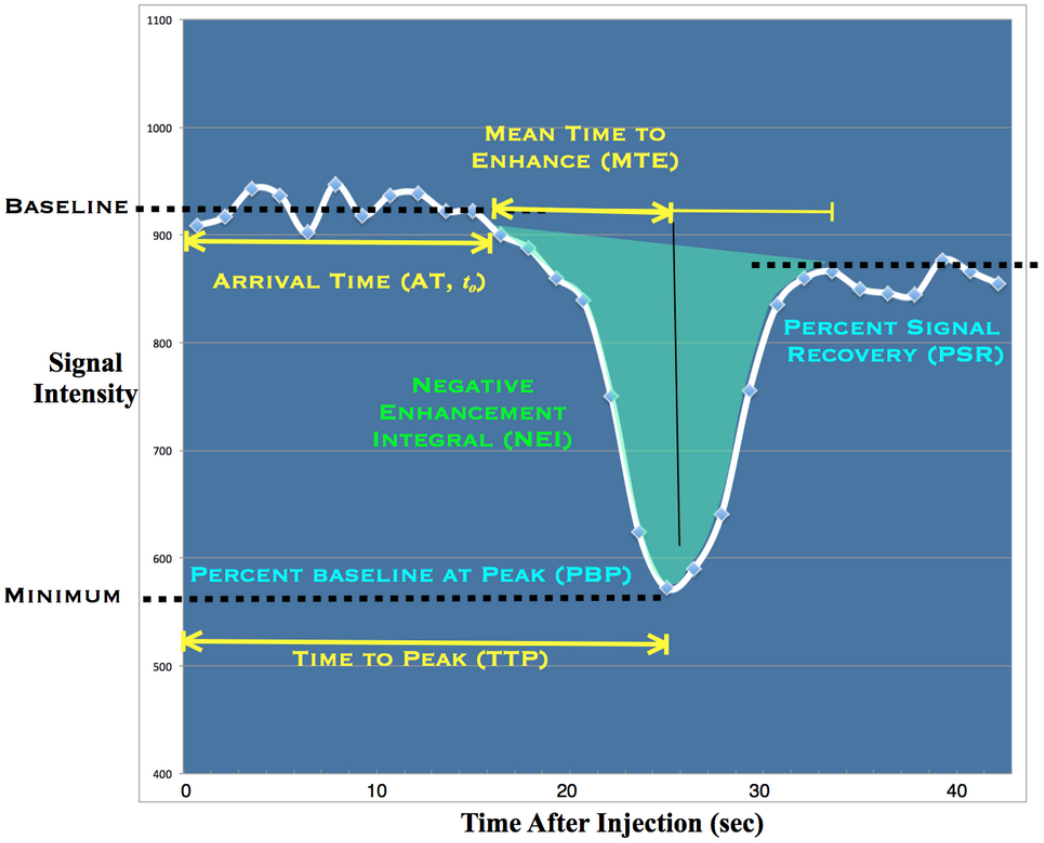

Figure 28: Simplified semiquantitative analysis of DSC signal intensity curves. Courtesy of Allen D. Elster, MRIquestions.com.

The definition of the individual parameters is as follows:

- Arrival Time AT - it is the interval time between intravenous contrast injection and its first detection in tissue. It reflects the sum of all processes leading to tissue delivery of contrast
- Time to Peak TTP - it is time from initial contrast injection to maximal signal loss within the organ of interest
- Negative Enhacement Integral NEI - it is a total area under the signal intensity curve during first pass of contrast agent. In other words, it is a Area Under Curve AUC. This parameter reflects the total amount pf contrast transiting through the regional vascular system and is proportional to blood volume
- Mean Time to Enhance MTE - it is average time for the entire bolus of contrast to pass through a region of tissue. Absolute values are higly dependent on the shape of arribing contrast bolus and to a lesser degree on tissue perfusion

- Percent Baseline at Peak PBP and Percent Signal Recovery PSR - they are defines respectively as the ratio of signal intensity at minimum or during the recirculation phase divided by their initial baseline values.

Gadolinium concentration is proportional to the observed change in T_2^*-relaxation rate ($\Delta R_2^* = 1/\Delta T_2^*$), which is proportional to the negative logarithm of relative signal:

$$[Gd] \propto \Delta R_2^* = -\frac{1}{T_E} ln(\frac{S_t}{S_0}) \tag{59}$$

where S_0 is baseline signal intensity, while S_t is signal at time t during passage of contrast bolus [85] [86] [87].

The DCE imaging can be evaluated using a few methods: simple visual assessment, semi-quantitative descriptive indices or model-based quantification. Different parts of a dynamic contrast enhancement curve reflect various anatomic and physiological features. The step initial upslope of the curve corresponds to tissue blood flow and its peak height reflects total blood flow and volume. The following part of the curve is a result of contrast leaking into the tissue interstitium, which is influenced by capillary area and permeability. The later parts of the curve indicate the total tissue extracellular space and plasma interstitial volume. On the Figure 29 below the contribution to total contrast enhancement was presented.

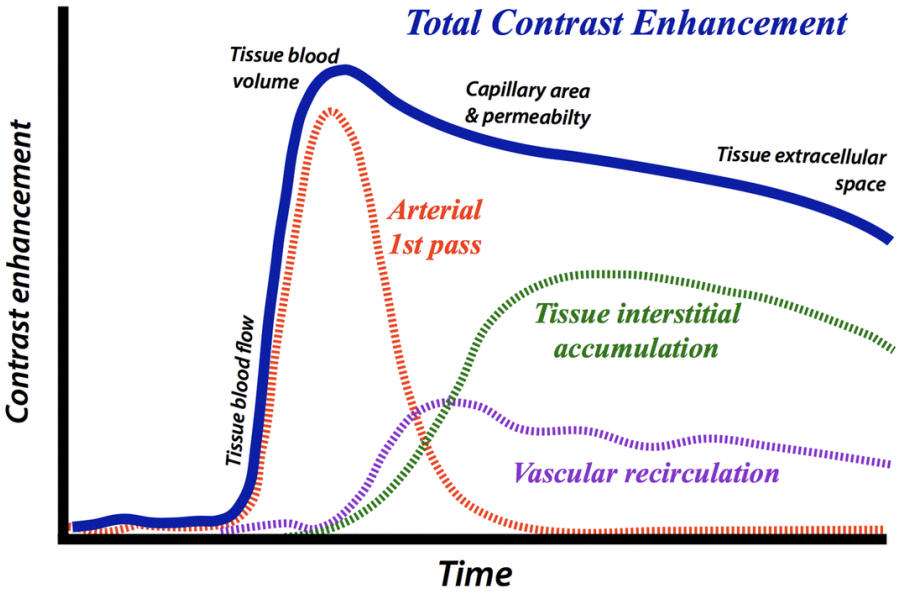

Figure 29: Contributions to total contrast enhancement as a function of time. Courtesy of Allen D. Elster, MRIquestions.com.

Semi-quantitative descriptive indices from the raw signal intensity data can also be applied to

this data, similar to those used for DSC imaging. On the other hand, a full quantitative analysis of DCE requires three steps:

1. Conversion of signal intensity to gadolinium concentration
2. Selection of an appropriate tissue model
3. Estimation of model parameters from fitted data.

After converting the raw DCE signal data to gadolinium concentration, the next step is to determine the tissue model to which the data will be fitted. Most widely used model is Tofts-Kermode Model. This model was presented in Figure 30 below.

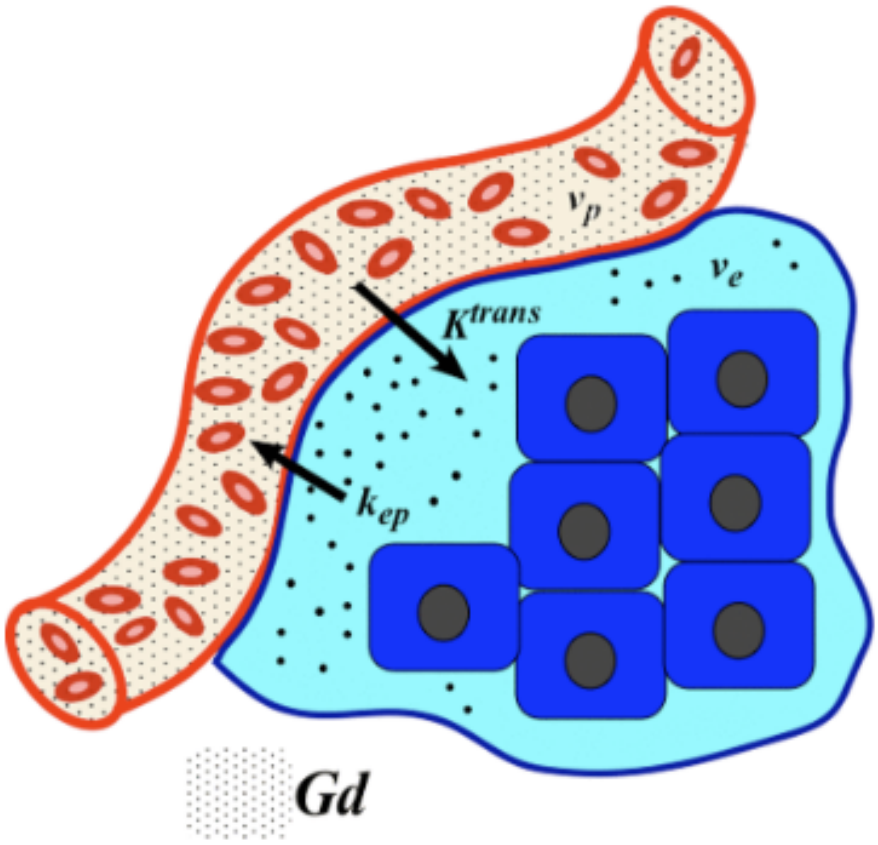

Figure 30: Graphicall representation of Tofts Model. Courtesy of Allen D. Elster, MRIquestions.com.

In this model, each voxel contains three components: tissue parenchymal cells (dark blue), blood vessels (containing erythrocytes and plasma) and tissue extracellular extravascular space (EES). When gadolinium contrast is injected, it moves from the plasma to the EES through the vascular endothelium due to a concentration gradient. The rate at which gadolinium moves (K^{trans}) depends on blood flow, vascular surface area and vascular permeability. The corresponding rate

at which gadolinium moves back from the EES to the plasma is denoted as k_{ep}. Since gadolinium does not enter cells, its concentration depends on the fractional volumes of plasma (v_p) and the EES (v_e). The original model equation is formulated as:

$$\frac{dC_t}{dt} = K^{trans}(C_p - C_e) = K^{trans}(C_p - \frac{C_t}{v_e}) \tag{60}$$

This model assumes that the equilibrium concentration of gadolinium in tissue C_t, is driven by simple passive diffusion based on the concentration gradient between plasma C_p, and tissue extravascular extracellular space C_e. Gadolinium contrast does not enter cells because C_e is higher than C_t due to the dimension less volume fraction of the tissue extravascular extracellular space v_e. In this equation, K^{trans} is the mass transfer influx constant. The original model assumed that the intravascular contribution to total tissue gadolinium concentration was negligible. In other words, the fractional volume parameter v_p is very small and disregarded in the analysis. The simple model thus has only a single compartment with two free parameters and its differential equation can be solved by integration:

$$C_t(t) = K^{trans} \int_0^t C_p(\tau) e^{-(K^{trans}/v_e)(1-\tau)} d\tau \tag{61}$$

Using nonlinear least squares estimation on a voxel-by-voxel basis, K^{trans} and v_e can then be computed [88] [89] [90].

Arterial Spin Labeling (ASL) is an MRI method used to measure perfusion by using water molecules as a tracer. Unlike other methods, ASL doesn't require the injection of contrast agents. The process involves acquiring control images through the area of interest and then applying tagging pulses to a slab of tissue near the imaging volume, which inverts the magnetization of water molecules in that slab. After a few seconds, the magnetically labeled molecules within vessels flow to the imaging volume. These labeled water molecules then exchange their magnetization with those in the static tissue, causing a slight reduction in the latter's equilibrium magnetization. Subsequently, the area of interest is imaged again and data from the tagged images are subtracted from the control images pixel-by-pixel. The resulting subtracted image is a perfusion-weighted image. [91] [92].

7 Materials and Methods

This chapter provides a description of the materials and experimental apparatus used in the studies presented in this thesis. First, a description of investigated nanoparticles was provided. Next, a description of used ischemic stroke model in rats was described. In next step the experimental apparatus was briefly presented.

7.1 Nanomaterials

7.1.1 AOT Nanocapsules

The Dioctyl Sodium Sulfosuccinate (AOT) is an anionic surfactant, which can form stable microemulsions and nanoparticles, making it valuable for various drug delivery nanosystems and contrast agents in imaging. The chemical structure of AOT is presented in Figure 31 below.

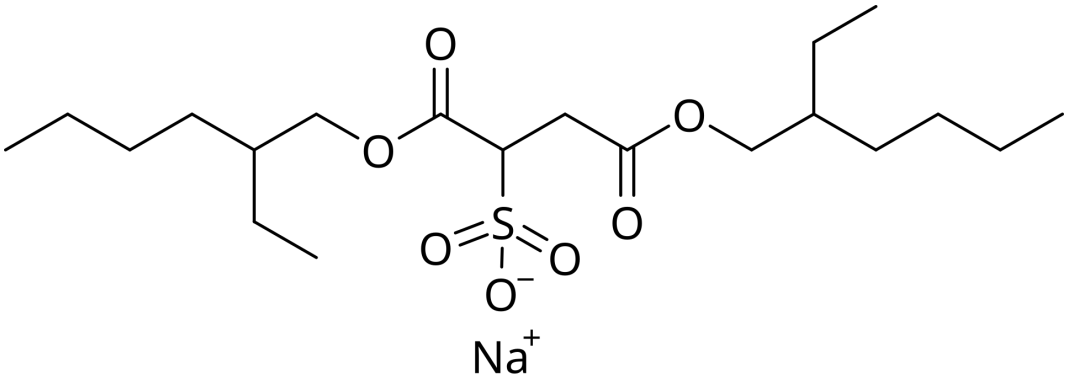

Figure 31: Chemical structure of AOT.

The AOT chemical structure comprises a hydrophilic head and two hydrophobic alkyl chains, allowing the formation of micelles and microemulsions in aqueous and organic environments.

Nanocapsules based on AOT can be used for imaging and therapy, making it promising candidates in theranostic applications. These nanocapsules can simultaneously transport therapeutic and diagnostic agents, encapsulate drugs to enable targeted delivery to disease areas, like stroke and allow monitoring of treatment progress through MR imaging.

The creation of AOT nanocapsules involves using the layer-by-layer method, where layers with opposite charges are added one after the other. The nanocapsules tested in the study had single and double layers containing gadolinium. The elements involved in the synthesis of nanocapsules are as follows:

- PLL - Poly-L-lysine hydrobromide

- PGA - Poly-L-glutamic acid sodium salt
- PEG - Polyethylene glycol

It is important to note the various benefits of AOT nanocapsules. Firstly, they are biocompatible, meaning they have relatively low toxicity. Secondly, they are multifunctional, as they can be used for both therapeutic and diagnostic purposes. Lastly, they are easy to modify. For instance, they can be functionalized by attaching ligands to target specific receptors, making them more effective in targeted therapies. In this disertetion, the following AOT samples were investigated.

Table 5: Description of investigated AOT nanocapsules.

Symbol	**Layers description**	**Gd concentration**
AOT 1x REF	AOT/PLL NCs with shell layers: PLL/PGA/PLL/PGA-g-PEG	0
AOT 1x Gd	AOT/PLL NCs with shell layers: PLL/PGA/PLL-Gd/PGA-g-PEG	$55\mu M$
AOT 2x REF	AOT/PLL NCs with shell layers: PLL/PGA/PLL/PGA/PLL/PGA-g-PEG	0
AOT 2x Gd	AOT/PLL NCs with shell layers: PLL/PGA/PLL-Gd/PGA/PLL-Gd/PGA-g-PEG	$120\mu M$

The purpose of the AOT/PLL nanocapsule study was to examine the contrast properties of nanocapsules with one and two layers containing gadolinium in shells. According to the table, the initial gadolinium concentration for one gadolinium layer was 55 μM, while for two gadolinium layers it was 120 μM. These samples were diluted successively to determine the molar relaxivities.

7.1.2 PCL Nanocapsules

Nanocapsules made of poly(ε-caprolactone) (PCL) are an important platform for delivering drugs and other bioactive substances. Polycaprolactone is a biocompatible and biodegradable polyester with low toxicity, si it is an attractive material for drug delivery. Its slow degradation time makes it ideal for creating carriers with extended release profiles, which is particularly important in the treatment therapy.

The polymer PCL is a semi-crystalline material. It does not dissolve in alcohol or water, but it can dissolve in non-polar solvents like benzene, chloroform and carbon tetrachloride. It is also slightly soluble in acetone, DMF, ethyl acetate and acetonitrile. PCL's insolubility in polar solvents presents a significant challenge for its applications and in the synthesis of PCL-based nanocarriers. PCL has a melting temperature between 59 and 64°C and a glass transition temperature of -60°C. It remains semi-crystalline in physiological conditions due to its melting point being significantly above body temperature. The chemical structure of PCL is presented in Figure 32 below.

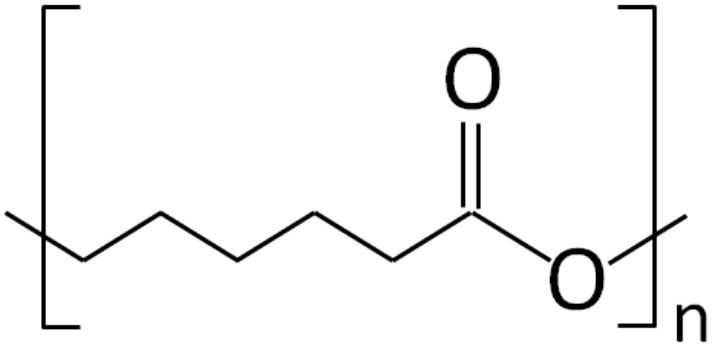

Figure 32: Chemical structure of PCL.

PCL nanocapsules consisting of a core and a polymer shell can be customized to transport different therapeutic compounds, including hydrophobic drugs, which have low solubility in water. These nanocapsules can be tailored to target specific tissues or cells with minimal side effects, due to their ability to undergo surface modification and control physicochemical properties such as size and surface potential.

The use of PCL nanocapsules extends beyond drug delivery. They can be used as carriers for diagnostics in modern theranostics. PCL's capacity to encapsulate different molecules and release them in a controlled manner makes it an extremely versatile material with the potential to revolutionize the approach to treating and diagnosing various diseases. The following PCL samples were investigated during this dissertation.

Table 6: Description of investigated PCL nanocapsules.

Symbol	Layers description	Gd concentration
PCL-PEG REF	PCL NCs (empty) in 0.015 M NaCl with following layers: PLL/PGA/PLL/PGA-g-PEG	0
PCL-Gd-PEG	PCL NCs (empty) in 0.015 M NaCl with following layers: PLL/PGA/PLL-Gd/PGA-g-PEG	$55\mu M$
PCL REF	PCL NCs with following layers: PLL/PGA/PLL/PGA/PLL/PGA-g-PEG	0
PCL	PCL NCs (empty) with following layers: PLL/PGA/PLL-Gd/PGA/PLL-Gd/PGA-g-PEG	$120\mu M$

The purpose of this study was to examine the contrast properties of PCL nanocapsules with one and two layers of gadolinium in the coating. The initial gadolinium concentration with one layer was 55 μM, while with two layers it was 120 μM. The samples were then diluted to determine the molar relaxivities. The schematic composition of NCs with 2 layers of contrast agent was presented on Figure 33 below.

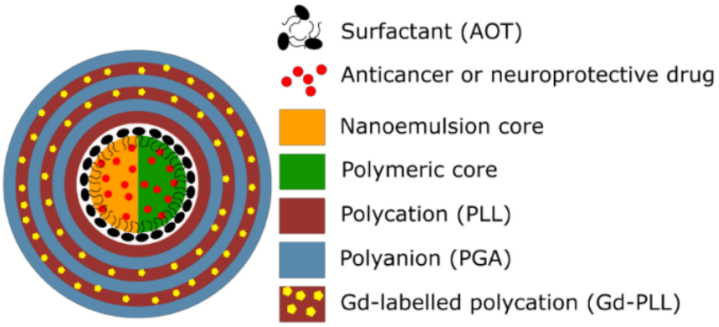

Figure 33: Schematic composition of NCs with 2 layers of contrast agents (PLL-Gd).

7.1.3 CQD Nanoparticles

Quantum dots (CQD) are becoming important materials in the field of theranostics, especially in the field of MRI. They are highly advanced fluorescent nanoparticles discovered in the semiconductor industry. Quantum dots are nanoparticles with a crystal size of approximately 20 nm in diameter or less. At this size, electrons are confined three-dimensionally to a limited area and exhibit the quantum size effect. Due to this effect, quantum dots display fluorescent properties, which are completely different from those of traditional fluorescent probes, such as

organic fluorescent dyes and naturally occurring fluorescent proteins.

Additional ligands can be attached to CQDs, thereby obtaining additional properties. For MRI applications, gadolinium was added to the CQD structure, creating a CQD-Gd compound with an initial gadolinium concentration of 41 mM. Samples were filtered through a 1 μm filter and sent for MRI contrast testing.

7.1.4 POSS-based Nanoparticles

A Polyhedral Oligomeric Silsesquioxane (POSS) is a type of hybrid material with a unique 3D configuration, a definite framework and customizable physicochemical properties. It can be considered the smallest form of hybrid silica-based material with a size ranging from 1 nm to 3 nm [93] [94]. The basic chemical structure of POSS has the composition of $(RSiO_{1.5})_n (n = 6, 8, 10, 12, ...)$, where R represents either a hydrogen atom or organic groups. The most common form of POSS is $n = 8$, also known as a POSS cage. POSS molecules consist of a core cubic cage of eight silicon corner atoms and twelve oxygen edge atoms Si—O—Si, with each silicon atom potentially carrying an organic group around the periphery of the cage. These groups can be further modified to create hundreds of possible compounds. POSS combines many of the benefits of silica, such as thermal, chemical and radiation stability and optical transparency with those of siloxane polymers, such as solubility and low toxicity. Additionally, their structure can be further modified by functionalizing R to achieve desired properties [95]. The schematic representation of investigated POSS nanoparticles (NPs) was presented on Figure 34 below.

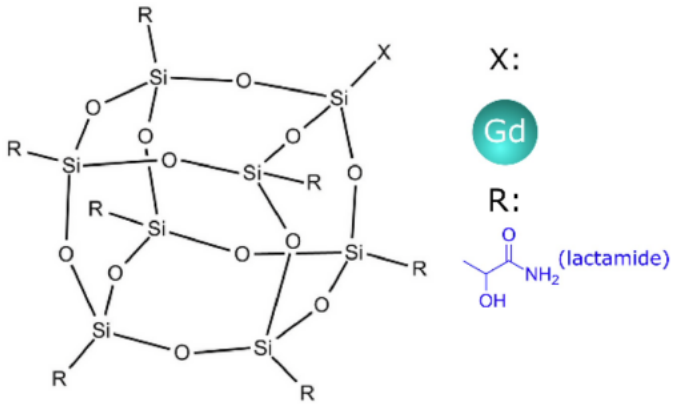

Figure 34: Schematic representation of investigated POSS NPs.

The aim of this step in dissertation was to evaluate MRI contrasting properties of series of modification POSS-based nanoparticles: POSS-Gd in PBS, POSS-Gd in water solution, Lactamide POSS-Gd and POSS without gadolinum. POSS-based nanoparticles were prepared by

a two step synthesis: controlled sol-gel synthesis of POSS followed by chemical conjugation of gadolinium Gd to chemical structure.

The samples for MRI investigations were prepared by successive dilution of the nanoparticles solution. The initial concentration of the gadolinium/nanoparticles were: 23.85 mM for POSS-Gd in PBS, 2.98 mM for POSS-Gd in water and Lactamide POSS-Gd, and 23.85 for POSS. Obtained sets of samples are described in the Table below.

Table 7: Description of investigated POSS-based nanoparticles.

Nanoparticle	**Initial Gd/NPs concentration [mM]**	**Concentration of Gd/NPs in samples for MRI [mM]**
POSS-Gd in PBS	23.85	0.09, 0.19, 0.37, 0.75, 1.49, 2.98
POSS-Gd in water	2.98	0.09, 0.19, 0.37, 0.75, 1.49, 2.98
Lactamide POSS-Gd	2.98	0.09, 0.19, 0.37, 0.75, 1.49, 2.98
POSS	23.85	2.98, 5.96, 11.93, 23.85

7.1.5 Cerium Oxide-based Nanoparticles

Cerium oxide nanoparticles (CeO2 NPs) have a wide range of applications in the materials industry, including glass polishing, fuel additives to enhance combustion, electrolytes for solid oxide fuel cells, ultraviolet absorbents and oxygen sensors. They are highly valued for their regenerative antioxidant properties and their ability to facilitate ion transfer through the nanoparticle matrix. In addition to their materials-related uses, CeO2 NPs also hold promise for treating diseases associated with oxidative stress, particularly those related to neurodegeneration.

Cerium is a rare earth element belonging to the lanthanide series. It has two partially filled subshells of electrons, $4f$ and $5d$, with several hypothesized excited substates. The cerium atom can exist in two valence states: either +4 (fully oxidized) or +3 (fully reduced) and it alternates between the two in redox reactions. In nanoparticle form, cerium is bound to oxygen in a crystalline fluorite lattice structure, which exhibits oxygen electron holes in the lattice structure. These arise from the absence of oxygen and/or its electrons. Additionally, besides the cerium atom being capable of shifting between +3 and +4, the stoichiometry of the nanoparticle can change from CeO2 to CeO2-x. Due to changes in redox state and oxygen vacancies, CeO nanoparticles interact with numerous free radicals, detoxifying their harmful activity. Furthermore, because of the lattice structure and ease of electronic conversions with other ionic species at the quantum level, CeO2 nanoparticles can regenerate their redox-active matrix, allowing repetitive interactions with free radicals. [96] [97].

In this work, the MRI contrast properties of the following CeO2 nanoparticles with modifications with following initial concentration were analyzed: CeO2-Gd with concentration 4.34 mM, CeO2 with nanoparticle concentration 3.78 mM and CeO2-Gd-PAA with concentration 2.04 mM. Nanoparticles with gadolinium were filtred using 450 nm filter. The Table below presents CeO2-based nanoparticles.

Table 8: Description of investigated CeO2-based nanoparticles.

Nanoparticle	**Initial Gd/NPs concentration [mM]**
CeO2-Gd	4.34
CeO2	3.78
CeO2-Gd-PAA	2.04

7.2 MCAO Model

The purpose of the previously described nanoparticles and nanocapsules is to deliver neuroprotective drugs to the brain in the case of ischemic changes. To achieve this goal, the use an appropriate model of ischemic stroke is necessary. Among the developed models, the middle cerebral artery occlusion (MCAO) model in rats is commonly used and closely mimics human ischemic stroke [77] [78]. The reason is fact that in humans, the middle cerebral artery MCA and its branches are most frequently affected by ischemic stroke, up to 70% of all cerebral strokes [79]. Moreover, the major cerebral arteries of rats are very similar to human arteries in terms of their structure and morphological functions [81]. Having an animal model of ischemic stroke is crucial for understanding the complex cellular and molecular mechanisms and for designing new approaches for neuroprotective therapy with theranostics.

The MCAO model induction procedure was performed at the Faculty of Pharmacy, Medical College of the Jagiellonian University. All experiments were permformed on male Sprague-Dawley rats. Dexpanthenol gel was applied to both eyes to prevent drying. The surgical procedure was performed under a stereomicroscope (Leica, A60F; Germany) and the body temperature was maintained at physiological levels with a heating blanket (Homeothermic Blanket System; Harvard Apparatus). Rats were anesthetized with 5% isoflurane for induction and 2.5% isoflurane for maintenance of optimal anesthesia. After exposure of the left external carotid artery (ECA), internal carotid artery (ICA) and common carotid artery (CCA), all ECA branches were coagulated. The ECA, ICA and CCA arteries were temporarily secured

with microvascular clips. During the most important part of the procedure, a silicon-coated filament (Doccol, USA) was introduced into the ECA lumen and advanced until blook flow decreased. The clips were removed from the CCA and the wound was secured with silk sutures. Arterial occlusion was confirmed using a laser contrast analysis system (PeriCam HR PSI, Perimed, Sweden) and a 70% reduction in blood flow in the middle cerebral artery territory was considered evidence of surgical success. This occlusion was maintained for 90 minutes. The wound was then reopened to remove the filament and restore blood flow. The wound was then closed again [100]. The Figure 35 below presents major rat head and neck arteries and filament position during MCAO procedure.

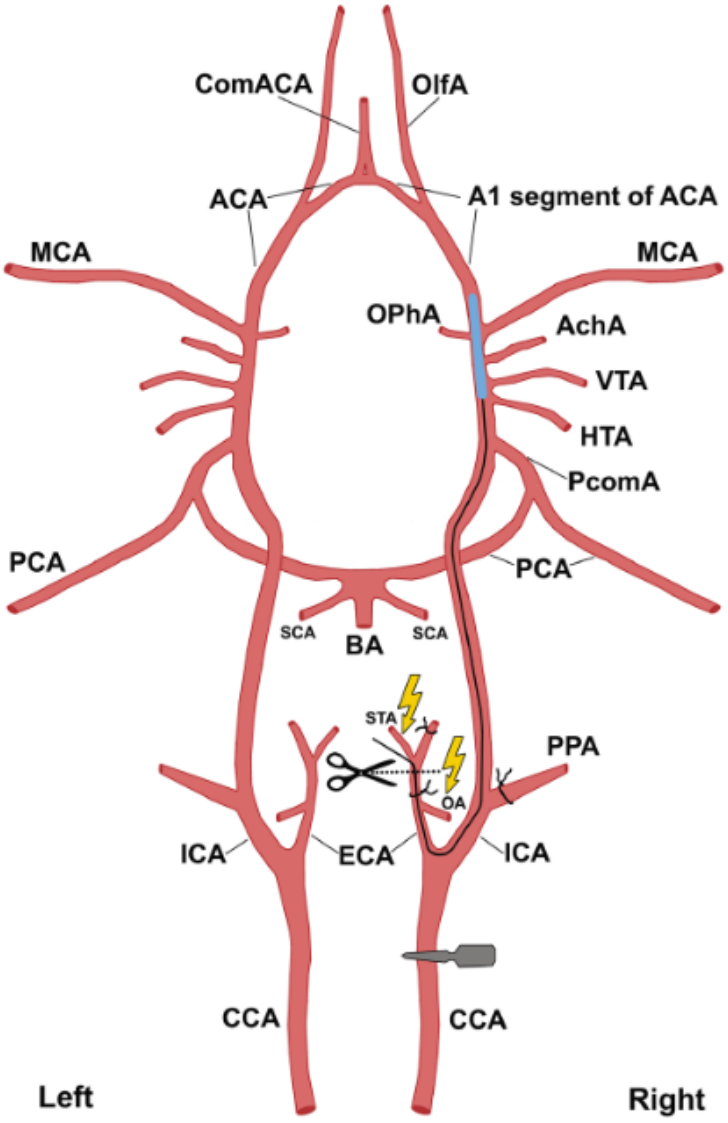

Figure 35: Schematic representation of the major rat head and neck arteries (view from the top) and the appropriate filament position during MCAO. Reprinted from [98] under the Creative Commons Attribution 4.0 International License.

The Table 9 below lists the rats used for in vivo studies using the MCAO model. The table also provides information on the time of MRI imaging.

Table 9: Description of investigated rats in the case of MRI.

Rat Name	**MRI Contrast Type**	**MRI Time Interval After Occlusion [h]**
MCAO 0	Magnevist^{TM}	CONTROL
MCAO 1	Magnevist^{TM}	24
MCAO 2	Magnevist^{TM}	24
MCAO 3	AOT/PLL 1xGd	24, 48
MCAO 4	PCL 1xGd	24, 48
MCAO 5	PLL-Gd	24, 96, 120
MCAO 6	NaCl	24, 48, 96
MCAO 7	NaCl	24, 48, 96, 240
MCAO 8	NaCl	24, 48, 96, 240

In the rat nomenclature which was used, the MCAO 0 rat was the control, healthy rat. In all above rats, T_2 maps, ADC diffusion as well as ASL perfsuion and the resulting T_1 map were imaged at different time intervals. DCE imaging of the biodistribution of different contrast agents in the rat brain was also performed. In this case, fast FLASH imaging sequence was used, during which the appropriate contrast agent was injected into the rat tail.

7.3 Experimental Equipment and Software

All magnetic resonance relaxation and imaging measurements were obtained using the *9.4 T Bruker BioSpec Avance III MRI* (Bruker; Germany) system at the Institute of Nuclear Physics PAS in the Department of Magnetic Resonance Imaging. The scanner has a 210 mm bore diameter and two systems of high-performance actively shielded gradient system with integrated shims, with an interior diameter of 120 mm and 60 mm. This system was installed in 2011 and was the first of its kind in Poland. It is a fully complete and advanced imaging system, allowing for interdisciplinary in vitro and in vivo biomedical research using non-invasive methods and MR spectroscopy with various animal models. The equipment includes a number of specialized measuring coils for conducting research using ^{1}H, ^{31}P, ^{19}F, and ^{13}C nuclei. Among other things, the system is equipped with a cryocoil, which allows to obtain high-quality images in a short time. The PC-SAM (SA Instruments; USA) deviced for monitoring and maintaining

vital functions during measurements allows for full control of the animal condition and their control. The Figure below shows MRI system installed at the Institute of Nuclear Physics PAS.

Figure 36: Bruker BioSpec Avance III MRI 9.4 T.

In the software case, ParaVision 7.0 (Bruker, Germany) was used to accomplish MR imaging and spectroscopy. For processing and analysis of obtained data and images, the ParaVision, ImageJ, MATLAB (MathWorks), Python 3.11 via VS Code IDE and DSI Studio were mainly used. All advanced image data analysis scripts were hand written using the above tools.

7.4 MRI Pulse Sequences

7.4.1 MSME and RARE VTR

The sequence Multi Slice Multi Echo (MSME) creates multiple spin echoes using the Carr-Purcell-Meiboom-Gill (CPMG) sequence with slice selective RF pulses, where each echo is used to obtain an image with different echo time T_E. As a result, a series of echo images allows to calculate T_2 relaxation time. In this case, MSME images were used to obtain the mean signal intensities in ROIs for each T_E. This signal intensity and echo time T_E can be described with this function:

$$I(t) = I_0 * exp[-\frac{T_E}{T_2}] \tag{62}$$

This function was used to find T_2 values. The Figure 37 below represents a time diagram of MSME sequence.

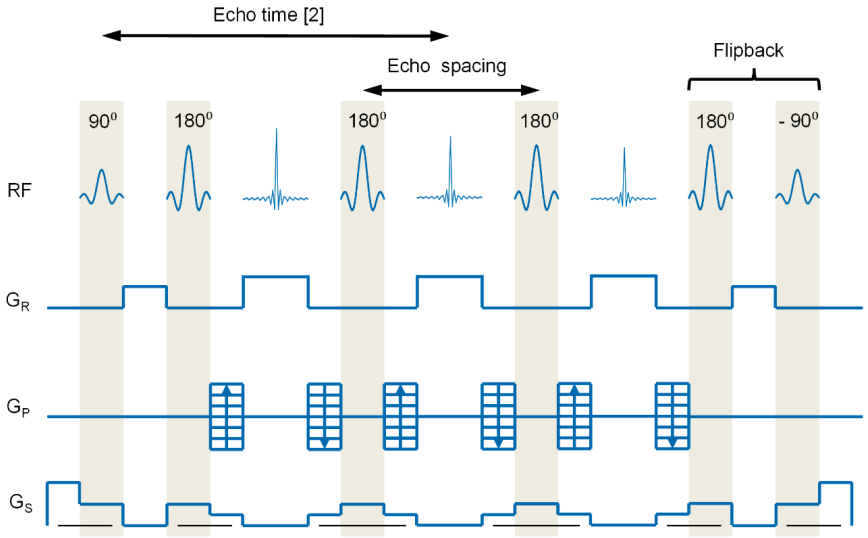

Figure 37: Pulse diagram of MSME sequence. Reprinted from ParaVision 7.0 - User Manual.

Application of MSME sequence include T_2-weighted imaging and T_2-value mapping with $TE \approx T2$ and $TR > T1$ or double MRI contrast, where first echo signal group is for T_1 contrast, but second is for T_2 contrast.

At this point, it is worth to analyze some parameters of MSME sequence, such as:

- Echo Spacing - time between the centers of consecutive echoes. Low value allows decrease effective echo time
- Echo Images - number of images with different effective echo times

- Echo Time - delay between the excitation RF pulse and the central phase-encoding step. This parameter determines the T_2 contrast and depends on the echo spacing and RARE factor
- Echo Averages - number of consecutive echoes, which will be averaged to give the echo image
- Excitation Angle - flip angle of the excitation pulse

The principle of sequence Rapid Acquisition with Relaxation Enhancement with variable Repetition Time (RARE VTR) is the same as MSME, but there's a possibility of multiple acquisitions with the repetition time T_R varied for a saturation recovery series. In this case, there is an important parameter named RARE Factor. It corresponds a number of different phase encoded echoes. Increasing this parameter reduces scan time, but typically increases the effective T_E and the blurring caused by T_2 relaxation [24].

RARE VTR images were used for T_1 measurements. In each ROIs, the mean of the signal accross the all repetition times was taken. The signal intensity can be described with this equation:

$$I = I_{max}(1 - exp[-\frac{T_R}{T_1}]) \tag{63}$$

This equation was used to calculate T_1 values.

The parameters used in MSME sequence were as follows: echo spacing was 7 ms, T_R was 2200 ms, averages and repetitions were equal 1, 20 echo images were obtained with T_E values in range 7 - 140 ms. Dummy scans were equal 2 and FA was 90^o. This sequence allow to obtain 9 slices with slice thickness 0.8 mm. Image size was equal 128 x 128 with field of view FOV 30 x 30 mm.

In case of RARE VTR sequence T_E was 7 ms, RARE factor was equal 2 with 9 T_1 experiments with following T_R values in range 200 - 15000 ms. Slice thickness was equal 1 mm and image size was 96 x 96 and FOV 30 x 30 mm. Finally, FA was equal 90^o. This sequence was used for *in-vitro* imaging experiments of different nanoparticles.

7.4.2 FLASH

The Fast Low Angle Shot (FLASH) is a general purpose MRI method based on a gradient echo generated with a single slice-selective RF pulse. Compensated phase encoding and contrast spoiling gradients allow to run the sequence with short repetition time. The final signal depends

on three parameters: T_R, T_E and FA plus three intrinsic tissue parameters like: T_1, T_2^* and proton density $[H]$. The signal can be described with this function:

$$S_{FLASH} = k[H] * \frac{(1 - exp[-\frac{T_R}{T_1}])}{1 - cos(FA)exp[-\frac{T_R}{T_1}]} * sin(FA) * exp[-\frac{T_E}{T_2^*}] \tag{64}$$

where k is scaling factor.

The contrast is relatively independent of T_1 and T_2 with short T_E and T_R, because of steady-state character of signal described in previous equation. The T_1 contrast can be obtained with the RF spoiling, which removes the echo contributions to the signal. With longer T_E, T_2^* contrast becomes dominant. The Figure 38 shows a time diagram of FLASH sequence.

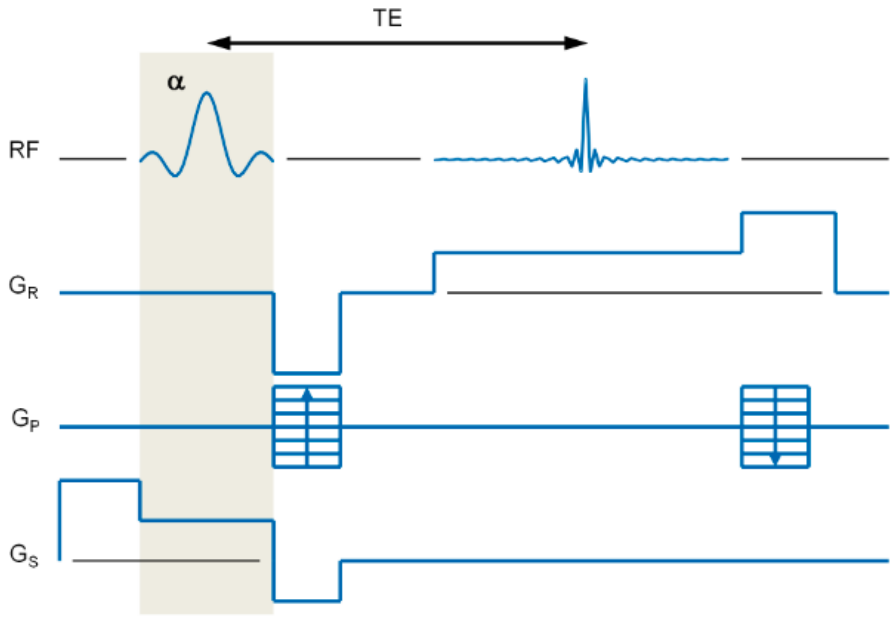

Figure 38: Pulse diagram of FLASH sequence. Reprinted from ParaVision 7.0 - User Manual.

The typicall aplications of FLASH sequence are: rapid pilot images, high resolution BOLD contrast imaging in fMRI with $T_E \approx T_2^*$, T_1-weighting imaging with short T_E and $T_1 > T_R > T_2$ or with short T_R and RF spoiling, susceptibility-weighted imaging and cardiac cine imaging.

The most important FLASH parameters are:

- Echo Time T_E - time between the center of excitation RF pulse and the center of the gradient echo. Determines the T_2^* contrast on the image
- Repetition Time T_R - time between consecutive excitation pulses of the same slice
- Flip Angle FA - flip angle of excitation pulse. Determines both T_1 and T_2 contrast of

the image. With short T_R and RF spoiling, increasing the flip angle FA enhances the T_1 contrast of the image.

For experiments included in dissertation, the FLASH parameters used in the biodistribution studies were as follows: T_E was 2 ms, T_R was 13 ms, FA was equal 12^o. Slice thickness of 1 slice was equal 1 mm and image size was 128 x 128 with FOV 30 x 30 mm. Dummy scans were equal 12. For biodistribution studies, the evolution function was used.

7.4.3 EPI

The Echo Planar Imaging (EPI) sequence is one of the fastest MRI pulse sequences, minimizing the effects of patient motion. This technique is capable of producing tomographic images at video rates. The EPI sequence depends on specialized equipment, including strong gradient fields, which are capable of rapid switching. However, sequence suffers from an increased sensitivity to signal loss from sources of susceptibility differences in sample [82].

The EPI method produces a series of differently phase-encoded gradient echoes following an FID or spin echo excitation by using periodic reversals of the readout gradient along with short phase encoding gradient blips. The K-Space matrix can be covered in one scan (Single Shot EPI) or in several interleaved segments (Multi-Shot EPI). Depending on excitation mode, the sequence has gradient echo or spin echo contrast properties. The EPI sequence is inherently strongly T_2/T_2^* weighted with a moderate T_1 weighting depending on the repetition time and flip angle [101]. The Figures below present pulse diagram of early EPI sequence and the K-space coverage.

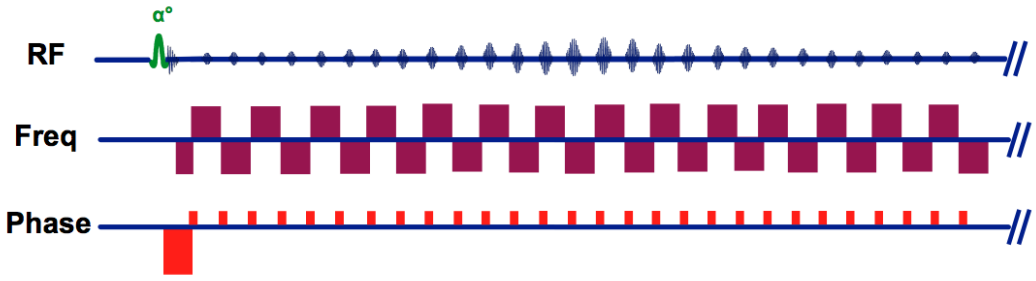

Figure 39: Modulus-blipped echo-planar single-pulse technique (MBEST), one of the early EPI sequences. Courtesy of Allen D. Elster, MRIquestions.com.

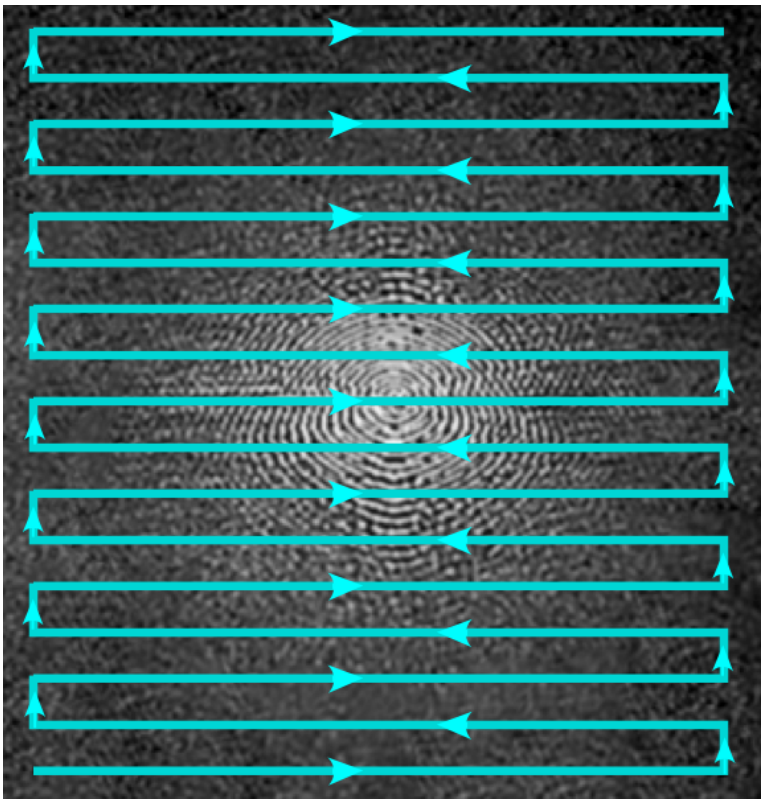

Figure 40: K-space coverage from MBEST. Frequency-encoding is along horizontal axis and phase-encoding is along the vertical. Courtesy of Allen D. Elster, MRIquestions.com.

The typicall EPI parameters in standard routine are as follows:

- Echo Time T_E - delay between the effective center of the excitation pulse and the acquisition of the K-Space center. Determines the T2* contrast of the sequence
- Repetition Time T_R - delay between corresponding slices in consecutive volume. It is also a time between first and second RF pulse
- Segments - the regions of k-space divided up by each shot of a multi-shot sequence. Allows running sequence in a number of interleaved shots to reduce image distortions caused by magnetic field inhomogeneity
- Signal Type - allows to select the type of final signal
- Bandwidth - effective bandwidth of the image in the frequency encoding dimension. A higher bandwidth reduces chemical shift artifacts and allow reach shorter echo times at the price of a lower SNR of ratio. The SNR is inverse-proportional to the square root of the effective bandwidth [24].

In diffusion measurements, the DTI_EPI protocol was used, which combine Diffusion Module and EPI Module. This combination allows to fast acquisition of diffusion weighted images and quantitative diffusion data. The main advantage of this method is he possibility of taking entire images with a single shot. It reduces scan time and eliminates the sensitivity of the experiment to microscopic motion. The typical applications of DTI_EPI protocol are: ultrafast diffusion weighted imaging, ultrafast measuring of ADC maps and ultrafast measurement of diffusion tensor images.

The following EPI parameters were used: T_E was 21.5 ms, T_R was 3000 ms, averages were equal 9 and repetitions 1, FA was equal 90^o. Dummy scan was 1. In this case, 9 slices were obtained with slice thickness 0.8 mm, image size was 108 x 96 with FOV 25 x 25 mm. Diffusion was measured one direction with following b-values: 15, 30, 50, ..., 1400, 1800 s/mm^2. In this case fat saturation was used.

7.4.4 FAIR-EPI

The Flow-sensitive Alternating Inversion Recovery with EPI (FAIR-EPI) method allows for measuring perfusion or conducting perfusion-weighted imaging based on the FAIR sequence. It involves acquiring a package of slices using an EPI sequence after applying either a selective or non-selective adiabatic inversion. The selective inversion is targeted at a slab covering the slice package. By subtracting selectively-prepared and non-selectively prepared images, blood flow in the imaging package can be visualized. Additionally, quantitative perfusion measurement is possible by acquiring images with different inversion recovery times.

Typicall aplications of FAIR-EPI sequence are measuring perfusion in brain on single slice, making dynamic perfusion-weighted imaging, and finally making T_1-mapping [24]. FAIR-EPI is a variant of EPI sequence, so the most parameters have the same. These parameters were described in previous subsection [24].

In FAIR-EPI sequence, the following parameters were used: T_E was 17.5 ms, averages and repetitions were equal 1, recovery time was 10000 ms, 17 values of T_R 10046, 10116, ..., 14016 ms and FA was equal 90^o. Slice thickness of 1 slice was equal 2 mm, image size was 64 x 64 with FOV 30 x 30 mm. Fat saturation was used in perfusion measurements.

8 Results

This chapter presents the most important research results of this work. These results are divided into two categories. The first one is the *in vitro* results of contrasting properties of different nanoparticles. This part presents the relaxation results and obtained molar relaxivities. The second part focuses on the *in vivo* results using the MCAO rat ischemic stroke model.

8.1 In Vitro MRI Contrasting Properties of Novel Theranostic Nanoparticles

8.1.1 AOT/PLL and PCL Nanocapsules

The first step of the relaxation studies was comparison of the contrast properties of AOT/PLL and PCL nanocapsules with one and two gadolinium layers on their shells [25]. The initial concentration of gadolinium in both types with one gadolinium layer was 55 μM, while for two gadolinium layers the concentration was 120 μM. The samples were successively diluted with distilled water and subjected to T_1-weighted and T_2-weighted imaging. The T_1-weighted images of investigated nanocapsules with one and two gadolinium layers are presented on Figures 41 and 42 below. As a reference, the samples of nanocapsules without gadolinium were presented.

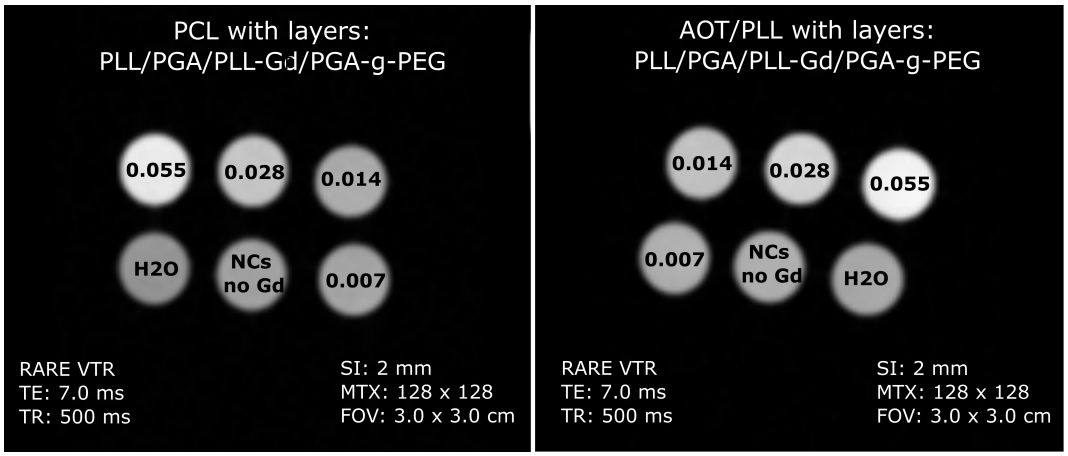

Figure 41: Obtained T_1-weighted images of PCL (on the left) and AOT/PLL (on the right) nanocapsules with one gadolinium layer for different Gd concentrations using RARE VTR sequence with TE = 7 ms and TR = 500 ms.

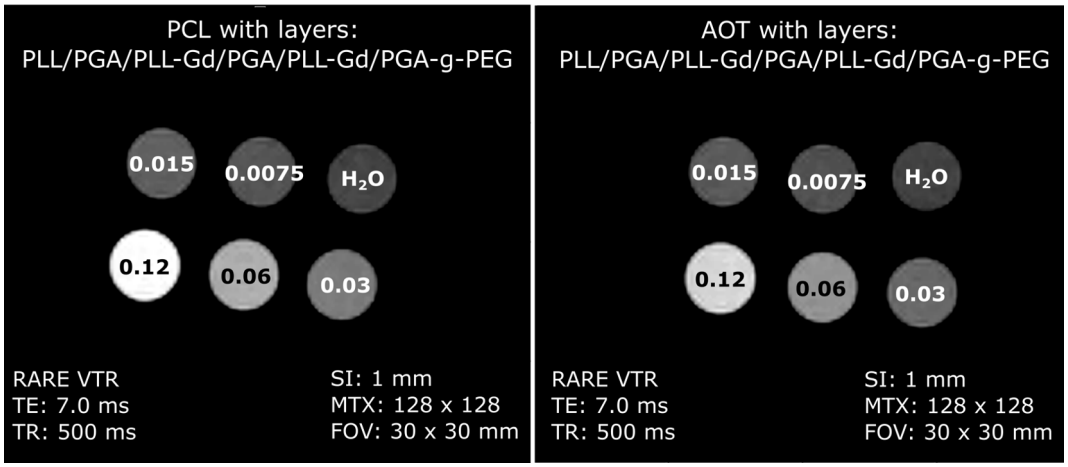

Figure 42: Obtained T_1-weighted images of PCL (on the left) and AOT/PLL (on the right) nanocapsules with two gadolinium layers for different Gd concentrations using RARE VTR sequence with TE = 7 ms and TR = 500 ms.

The obtained relaxation times T_1 and T_2 and obtained relaxation rates R_1 and R_2 for tested nanocapsules are presented in the Tables 10 and 11 below.

Table 10: Relaxation times T_1 and relaxation rates R_1 for AOT/PLL and PCL with one gadolinium layer.

Gadolinium concentration [mM]	**AOT/PLL 1xGd**		**PCL 1xGd**	
	T1 [ms]	**R1 [s^{-1}]**	**T1 [ms]**	**R1 [s^{-1}]**
0.055	1778 ± 10	0.56 ± 0.01	1712 ± 11	0.58 ± 0.01
0.028	2190 ± 11	0.46 ± 0.01	2091 ± 13	0.48 ± 0.01
0.014	2462 ± 10	0.41 ± 0.01	2294 ± 12	0.44 ± 0.01
0.007	2604 ± 12	0.38 ± 0.01	2397 ± 12	0.42 ± 0.01
H_2O	2793 ± 11	0.36 ± 0.01	2669 ± 11	0.37 ± 0.01

Table 11: Relaxation times T_1 and relaxation rates R_1 for AOT/PLL and PCL with two gadolinium layers.

Gadolinium concentration [mM]	**AOT/PLL 2xGd**		**PCL 2xGd**	
	T1 [ms]	**R1 [s^{-1}]**	**T1 [ms]**	**R1 [s^{-1}]**
0.12	1503 ± 6	0.67 ± 0.01	1332 ± 6	0.75 ± 0.01
0.06	1951 ± 6	0.51 ± 0.01	1800 ± 6	0.56 ± 0.01
0.03	2319 ± 6	0.43 ± 0.01	2226 ± 7	0.45 ± 0.01
0.015	2493 ± 7	0.40 ± 0.01	2466 ± 7	0.41 ± 0.01
0.0075	2627 ± 7	0.38 ± 0.01	2610 ± 6	0.38 ± 0.01
H_2O	2774 ± 8	0.36 ± 0.01	2797 ± 7	0.36 ± 0.01

In the tables above, the standard deviation of the relaxation times $u(T_{1,2})$ was calculated from the square root corresponding diagonal element of the covariance matrix Σ, which is the result of fitting the exponential function to obtained MRI signal amplitudes:

$$u(T_{1,2}) = \sqrt{\Sigma[1,1]} \tag{65}$$

In turn, the relaxation rate errors were calculated from the propagation of uncertainty law:

$$u(R_{1,2}) = \left[\frac{dR_{1,2}}{dT_{1,2}} * u(T_{1,2})\right]^2 \tag{66}$$

Based on the obtained results of relaxation times and relaxation rates, it is possible to plot a graph of dependence of the relaxation rate R_1 and the gadolinium concentration in accordance to the SBM theory. Molar relaxivities r_1 and r_2 were caldulated using equation 35. The Figure 43 below shows this dependence in nanocapsules with different amount of gadolinium layers.

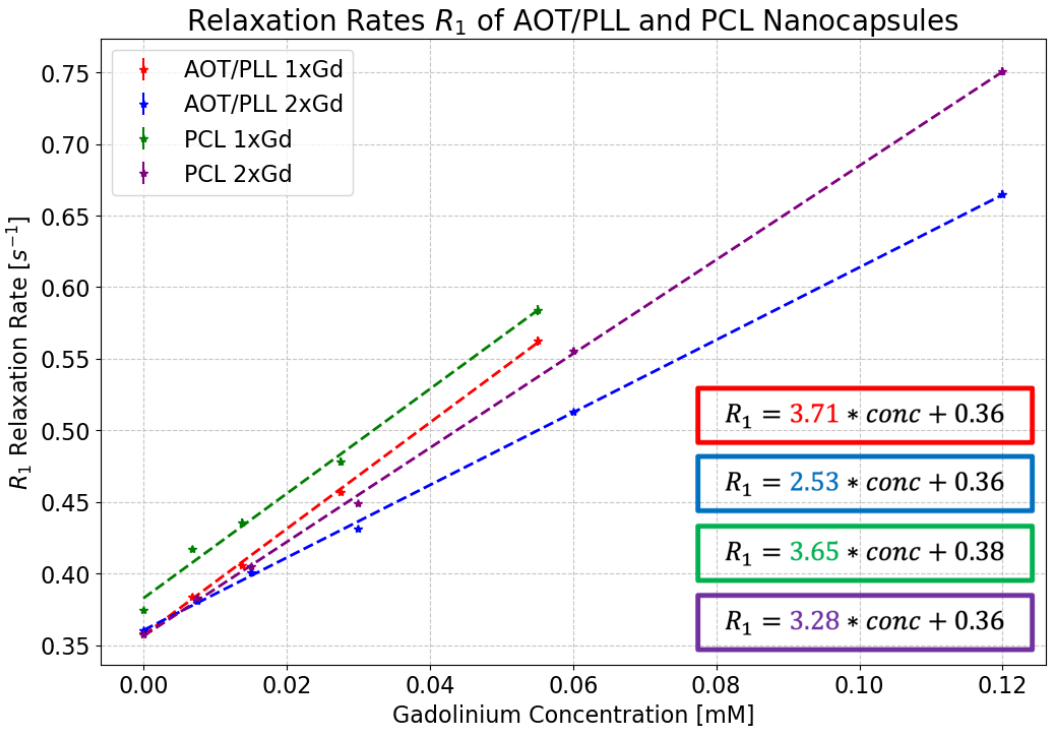

Figure 43: Dependence of the relaxation rate R_1 on gadolinium concentration for nanocapsules with one and two gadolinium layers.

From this figure, it can be seen that the molar relaxivities r_1 for nanocapsules are: 3.71 ± 0.05 $mM^{-1}s^{-1}$ for AOT/PLL 1xGd, 3.65 ± 0.18 $mM^{-1}s^{-1}$ for PCL 1xGd, 2.53 ± 0.03 $mM^{-1}s^{-1}$ for AOT/PLL 2xGd and 3.28 ± 0.03 $mM^{-1}s^{-1}$ for PCL 2xGd.

Using T_2 transverse relaxation measurements, it was possible to determine relaxation times T_2 and relaxation rates R_2. The Tables 12 and 13 below present obtained results for T_2 relaxation measurements.

Table 12: Relaxation times T_2 and relaxation rates R_2 for AOT/PLL and PCL with one gadolinium layer.

Gadolinium concentration [mM]	**AOT/PLL 1xGd**		**PCL 1xGd**	
	T2 [ms]	**R2 [s^{-1}]**	**T2 [ms]**	**R2 [s^{-1}]**
0.055	449 ± 3	2.23 ± 0.02	356 ± 2	2.81 ± 0.01
0.028	555 ± 4	1.80 ± 0.01	495 ± 3	2.02 ± 0.01
0.014	590 ± 4	1.69 ± 0.01	549 ± 4	1.82 ± 0.01
0.007	631 ± 6	1.59 ± 0.01	579 ± 4	1.73 ± 0.01
H_2O	625 ± 4	1.59 ± 0.01	662 ± 5	1.51 ± 0.01

Table 13: Relaxation times T_2 and relaxation rates R_2 for AOT/PLL and PCL with two gadolinium layers.

Gadolinium concentration [mM]	**AOT/PLL 2xGd**		**PCL 2xGd**	
	T2 [ms]	**R2 [s^{-1}]**	**T2 [ms]**	**R2 [s^{-1}]**
0.12	304 ± 1	3.29 ± 0.01	286 ± 1	3.49 ± 0.02
0.06	435 ± 2	2.29 ± 0.01	399 ± 1	2.50 ± 0.01
0.03	538 ± 3	1.86 ± 0.01	496 ± 3	2.02 ± 0.01
0.015	622 ± 4	1.61 ± 0.01	587 ± 3	1.71 ± 0.01
0.008	664 ± 5	1.51 ± 0.01	631 ± 4	1.59 ± 0.01
H_2O	677 ± 5	1.48 ± 0.01	664 ± 4	1.51 ± 0.01

The relaxation time errors were calculated based on the covariance matrix, while relaxation rate errors were calculated based on the propagation of uncertainty law. The Figure 44 below shows the dependence of relaxation rate R_2 and gadolinium concentration in nanocapsules.

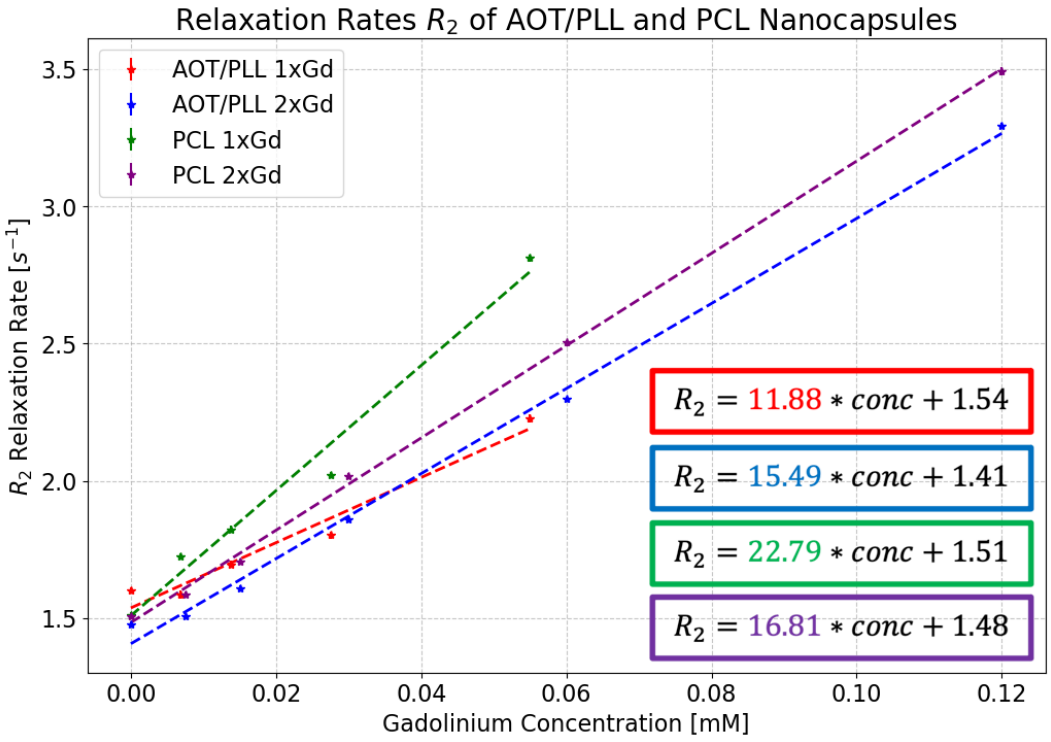

Figure 44: Dependence of relaxation rate R_2 on gadolinium concentration for nanocapsules with one and two gadolinium layers.

From the figure above, it can be seen that molar relaxivities r_2 are: 11.88 ± 1.33 $mM^{-1}s^{-1}$ for AOT/PLL 1xGd, 22.79 ± 1.84 $mM^{-1}s^{-1}$ for PCL 1xGd, 15.49 ± 0.47 $mM^{-1}s^{-1}$ for AOT/PLL

2xGd and 16.81 ± 0.28 $mM^{-1}s^{-1}$ for PCL 2xGd.

8.1.2 CQD Nanoparticles

The next nanoparticles considered for theranostic applications were quantum dots labelled with gadolinium atoms CQD-Gd. The initial gadolinium concentration was 41 mM and samples were successively diluted with distilled water. Using imaging protocol, it was possible to obtain T_1 and T_2 relaxation curves. The following Figures 45 and 46 show the obtained T_1 and T_2 relaxation curves for different gadolinium concentrations in CQDs nanoparticles.

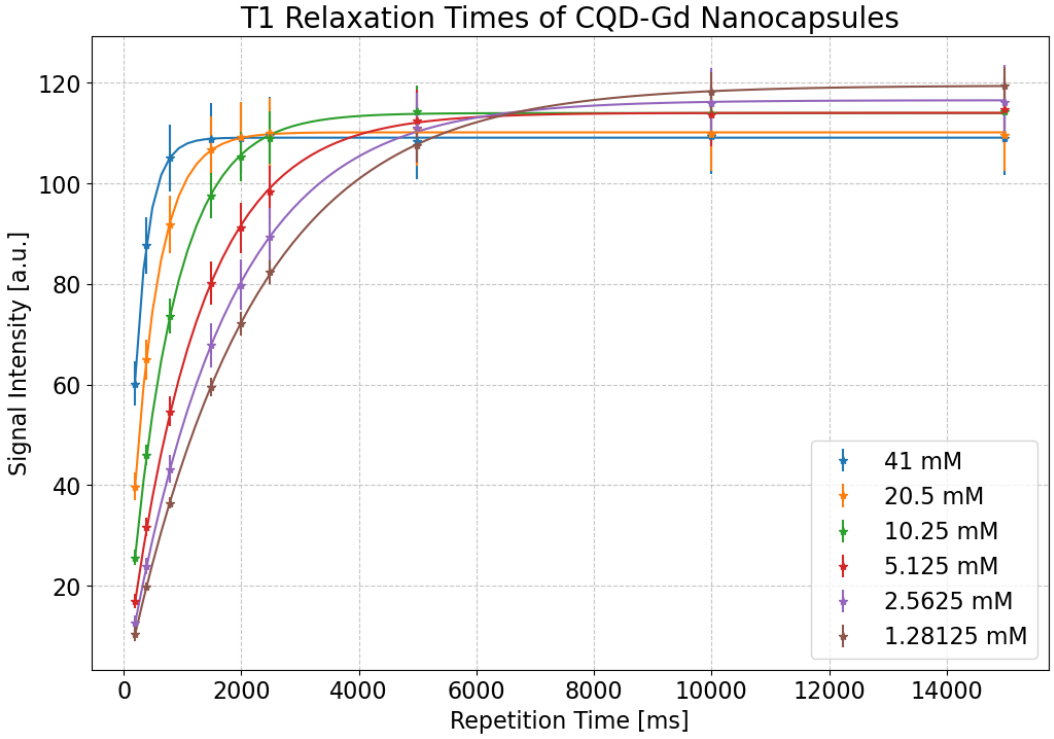

Figure 45: T_1 relaxation curves for different concentration of gadolinium in CQD nanoparticles.

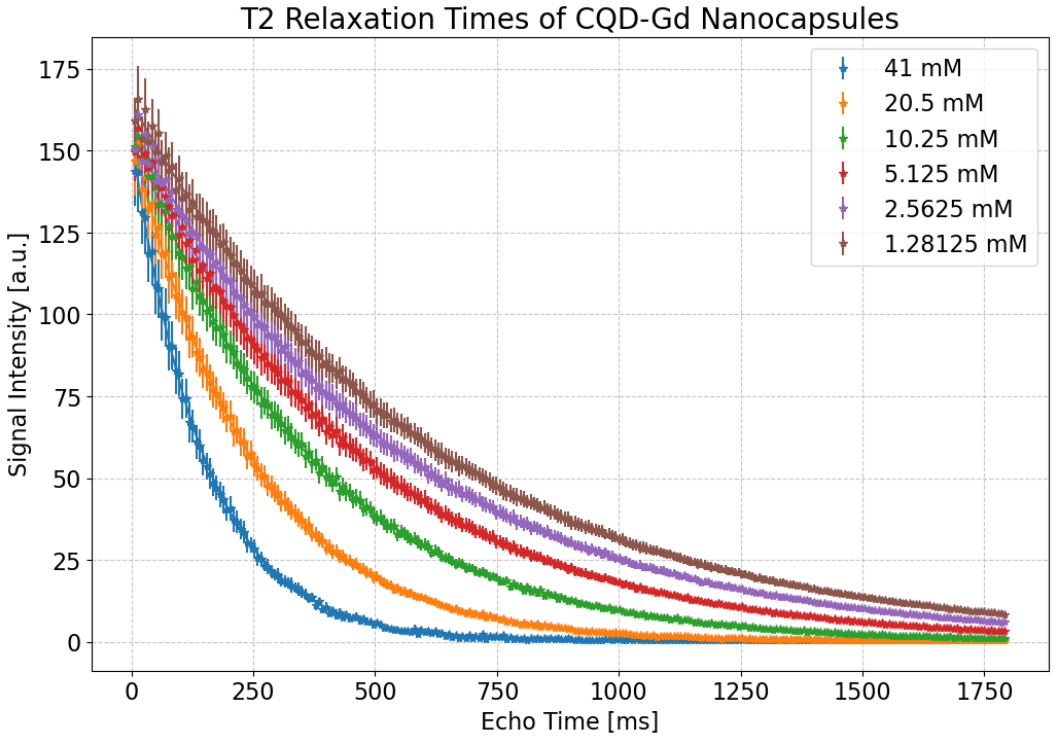

Figure 46: T_2 relaxation curves for different concentration of gadolinium in CQD nanoparticles.

Using the Bloch equations discussed in the theoretical part, it was possible to fit exponential equations to the obtained data in order to calculate the corresponding relaxation times T_1 and T_2. The Table 14 below presents obtained relaxation times and relaxation rates.

Table 14: Obtained relaxation times T_1 and T_2 and relaxation rates R_1 and R_2 for CQD-Gd nanoparticles.

Gadolinium concentration [mM]	**T1 [ms]**	**R1 [s^{-1}]**	**T2 [ms]**	**R2 [s^{-1}]**
41	237 ± 2	4.21 ± 0.03	149 ± 1	6.73 ± 0.02
20.5	434 ± 4	2.31 ± 0.02	242 ± 1	4.13 ± 0.01
10.25	761 ± 5	1.31 ± 0.01	356 ± 1	2.81 ± 0.01
5.125	1224 ± 12	0.82 ± 0.01	462 ± 1	2.16 ± 0.01
2.5625	1705 ± 11	0.59 ± 0.01	547 ± 1	1.83 ± 0.01
1.28125	2149 ± 9	0.47 ± 0.01	604 ± 1	1.65 ± 0.01

The errors of the relaxation times were calculated based on the covariance matrix. Relaxation rate errors were calculated based on the propagation of uncertainty law. The Figures 47 and 48 show dependence of relaxation rates R_1 and R_2 and the gadolinium concentration.

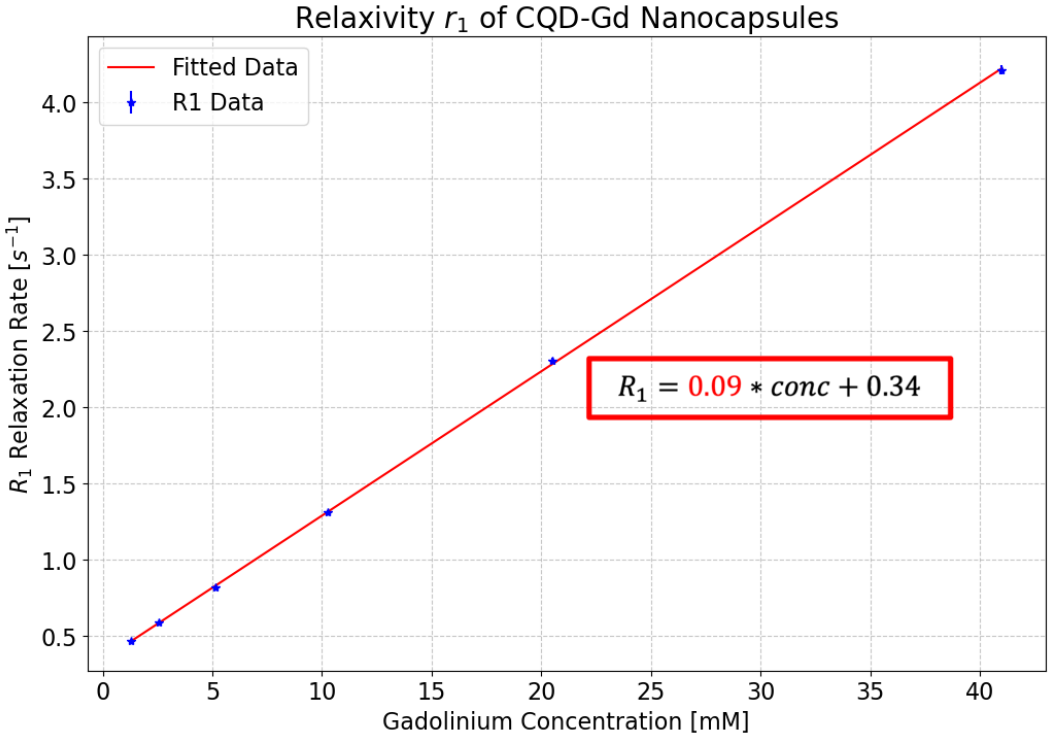

Figure 47: Dependence of relaxation rate R_1 on gadolinium concentration for CQD-Gd nanoparticles.

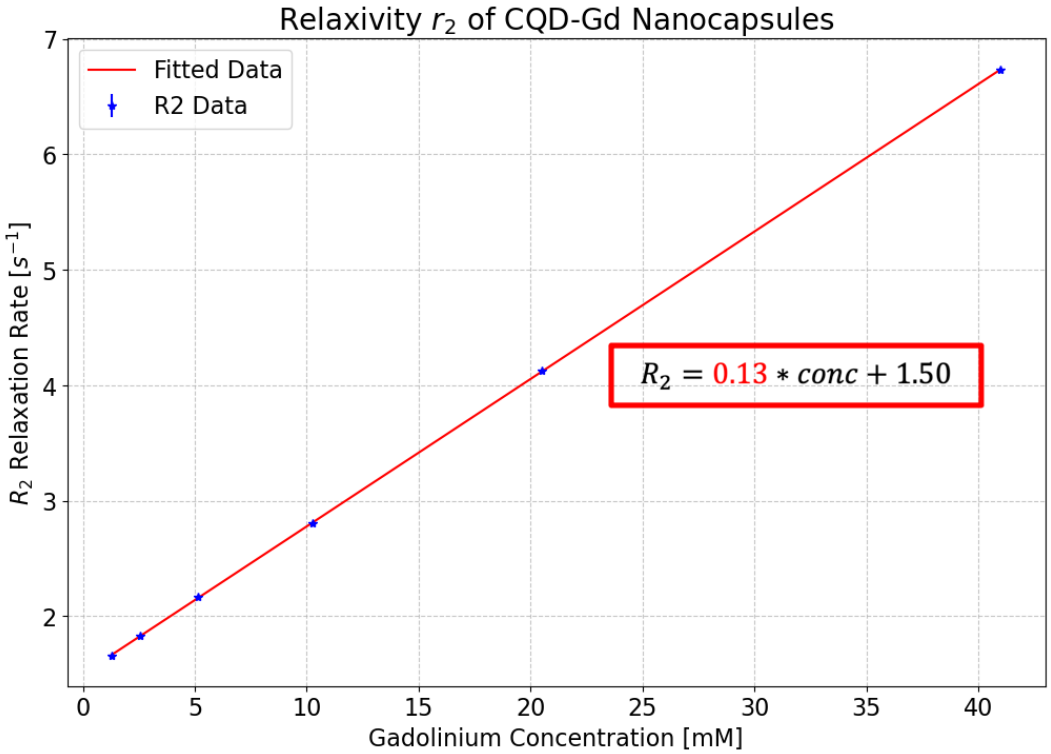

Figure 48: Dependence of relaxation rate R_1 on gadolinium concentration for CQD-Gd nanoparticles.

From the above figures, for CQD-Gd nanoparticles molar relaxivity r_1 is equal 0.09 ± 0.0004 $mM^{-1}s^{-1}$ and molar relaxivity r_2 is equal 0.13 ± 0.0003 $mM^{-1}s^{-1}$.

8.1.3 POSS-based Nanoparticles

The next analyzed nanoparticles were POSS-based nanoparticles, among it can be distinguished: Lactamide POSS-Gd, POSS-Gd in water solution, POSS-Gd in PBS solution and POSS without gadolinium labeling. The initial gadolinium concentration was 2.98 mM for Lactamide POSS-Gd, POSS-Gd in water and POSS-Gd in PBS. On the other hand, for POSS without gadolinium nanoparticle concentration was 23.85 mM. The example of obtained T_1- and T_2-weighted images of POSS-based nanoparticles were presented in Figures 49 and 50 below.

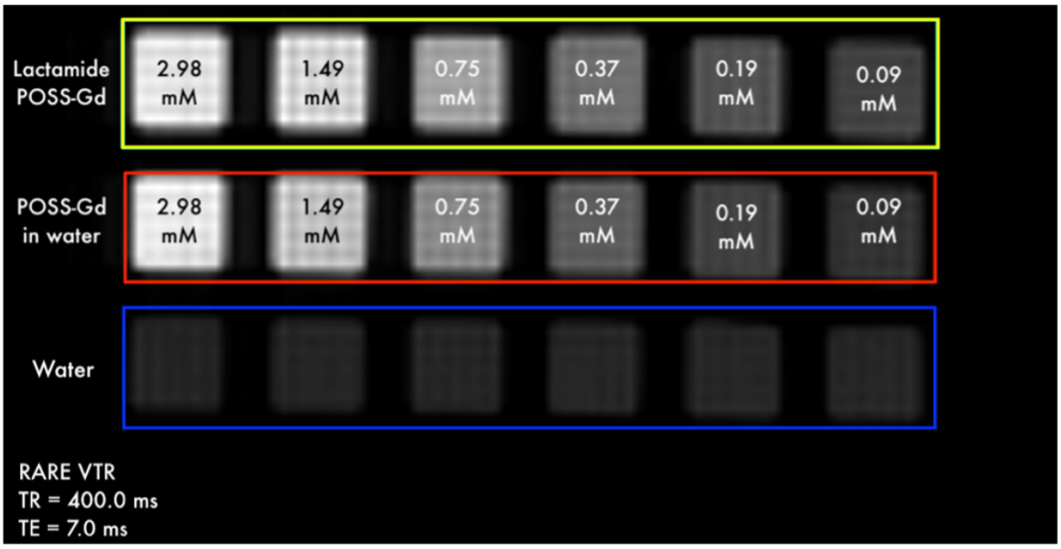

Figure 49: T_1-weighted image of Lactamide POSS-Gd and POSS-Gd in water solution using RARE VTR sequence with TR = 400 ms and TE = 7 ms.

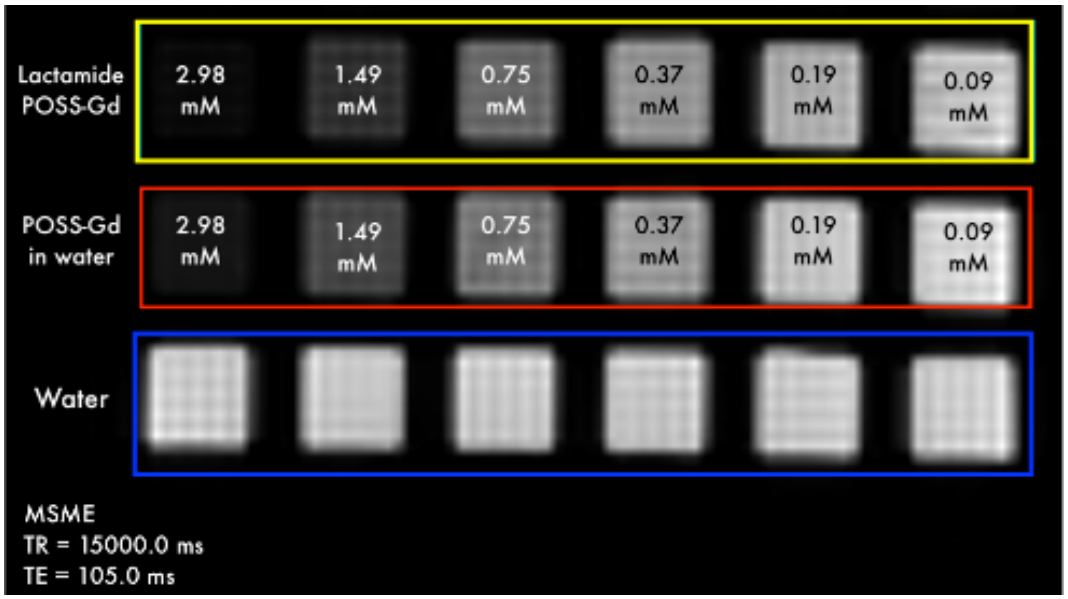

Figure 50: T_2-weighted image of Lactamide POSS-Gd and POSS-Gd in water solution using MSME sequence with TR = 15000 ms and TE = 105 ms.

The following Figures 51 and 52 show the obtained T_1 and T_2 relaxation curves for Lactamide POSS-Gd nanoparticles.

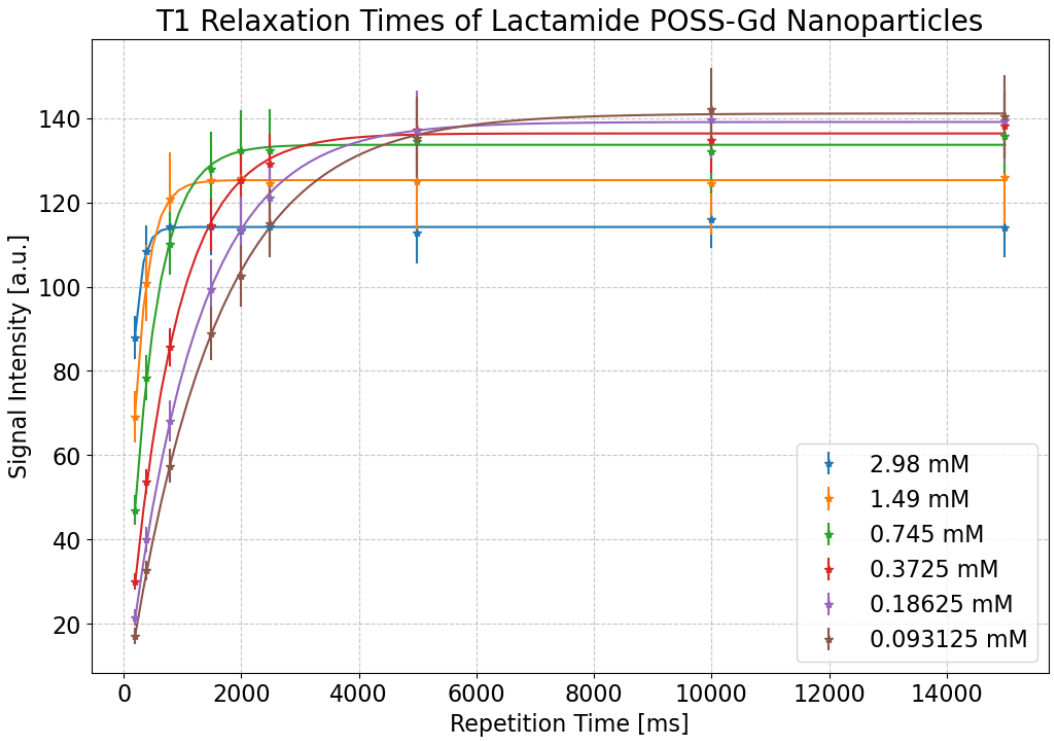

Figure 51: T_1 relaxation curves for Lactamide POSS-Gd nanoparticles.

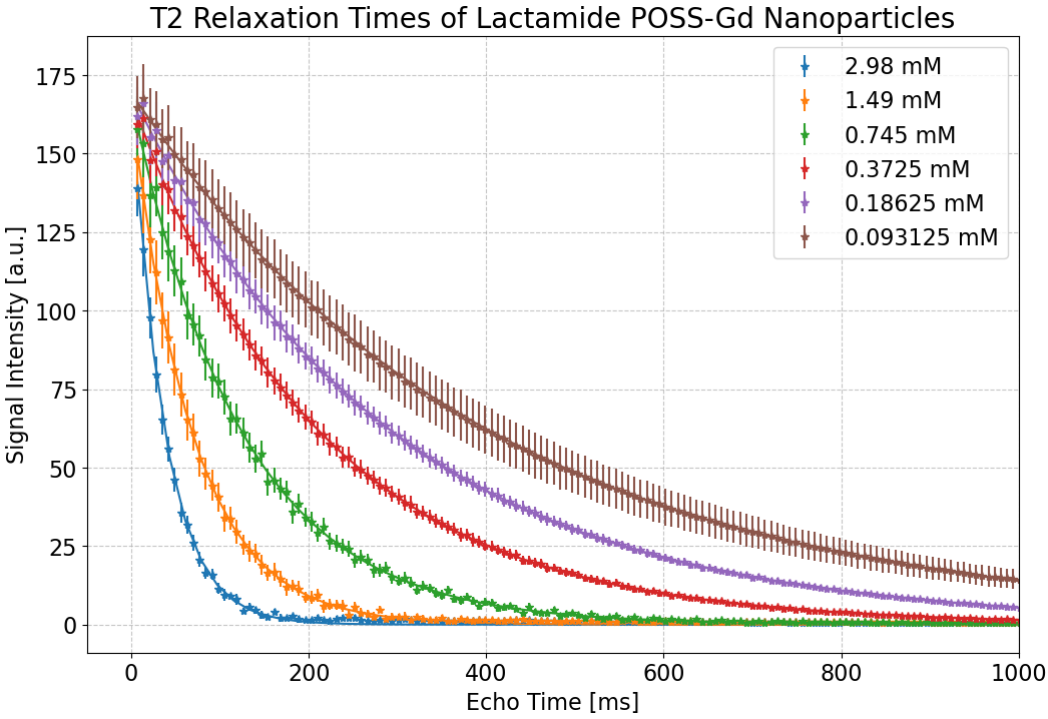

Figure 52: T_2 relaxation curves for Lactamide POSS-Gd nanoparticles.

The Tables 15, 16 and 17 below present obtained relaxation times and relaxation rates for POSS-based nanoparticles labeled with and without gadolinium.

Table 15: Relaxation times T_1 and relaxation rates R_1 for POSS-Gd-based nanoparticles.

Gadolinium concentration [mM]	**Lactamide POSS-Gd**		**POSS-Gd in water**		**POSS-Gd in PBS**	
	T1 [ms]	**R1 [s^{-1}]**	**T1 [ms]**	**R1 [s^{-1}]**	**T1 [ms]**	**R1 [s^{-1}]**
2.98	129 ± 3	7.75 ± 0.19	168 ± 4	5.94 ± 0.14	149 ± 9	6.71 ± 0.40
1.49	237 ± 2	4.22 ± 0.04	328 ± 4	3.05 ± 0.04	283 ± 5	3.53 ± 0.06
0.75	445 ± 8	2.25 ± 0.04	609 ± 12	1.64 ± 0.03	514 ± 3	1.95 ± 0.01
0.37	795 ± 15	1.26 ± 0.02	1021 ± 19	0.98 ± 0.02	874 ± 4	1.14 ± 0.01
0.19	1178 ± 11	0.85 ± 0.01	1588 ± 16	0.63 ± 0.01	1270 ± 8	0.79 ± 0.01
0.09	1503 ± 16	0.66 ± 0.01	2099 ± 23	0.48 ± 0.01	1595 ± 11	0.63 ± 0.01

Table 16: Relaxation times T_1 and relaxation rates R_1 for POSS nanoparticles without gadolinium compounds.

Nanoparticle concentration [mM]	**T1 [ms]**	**R1 [s^{-1}]**
23.85	2569 ± 1	0.3892 ± 0.0001
11.93	2684 ± 1	0.3725 ± 0.0001
5.96	2752 ± 1	0.3634 ± 0.0001
H_2O	2758 ± 1	0.3626 ± 0.0001

Table 17: Relaxation times T_2 and relaxation rates R_2 for POSS-Gd-based nanoparticles.

Gadolinium concentration [mM]	**Lactamide POSS-Gd**		**POSS-Gd in water**		**POSS-Gd in PBS**	
	T2 [ms]	**R2 [s^{-1}]**	**T2 [ms]**	**R2 [s^{-1}]**	**T2 [ms]**	**R2 [s^{-1}]**
2.98	37 ± 1	26.81 ± 0.18	46 ± 1	22.01 ± 0.12	3.7 ± 0.9	271.74 ± 62.77
1.49	69 ± 1	14.54 ± 0.07	89 ± 1	11.20 ± 0.04	6.3 ± 0.4	159.49 ± 9.67
0.75	124 ± 1	8.07 ± 0.03	136 ± 1	7.33 ± 0.03	12.9 ± 0.3	77.16 ± 1.85
0.37	212 ± 1	4.72 ± 0.01	221 ± 1	4.53 ± 0.01	26.2 ± 0.5	38.19 ± 0.71
0.19	290 ± 1	3.45 ± 0.01	382 ± 1	2.62 ± 0.01	47.7 ± 0.5	20.96 ± 0.24
0.09	400 ± 1	2.50 ± 0.01	525 ± 1	1.91 ± 0.01	71.4 ± 0.6	14.01 ± 0.11

Based on the obtained measurement results and analysis of relaxation times, the Figures 53 and 54 below show the dependence of relaxation rates R_1 and R_2 on the gadolinium concentration or nanoparticle concentration, in the case of POSS-based studies.

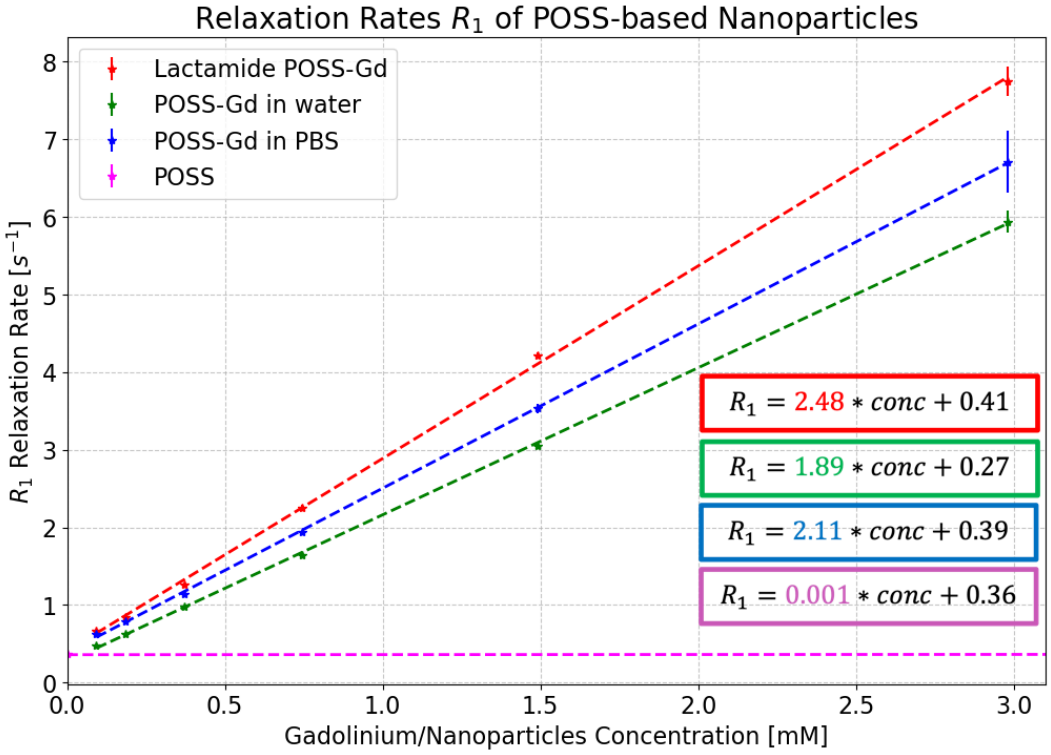

Figure 53: Dependence of relaxation rate R_1 on gadolinium/nanoparticle concentration for POSS-based nanoparticles.

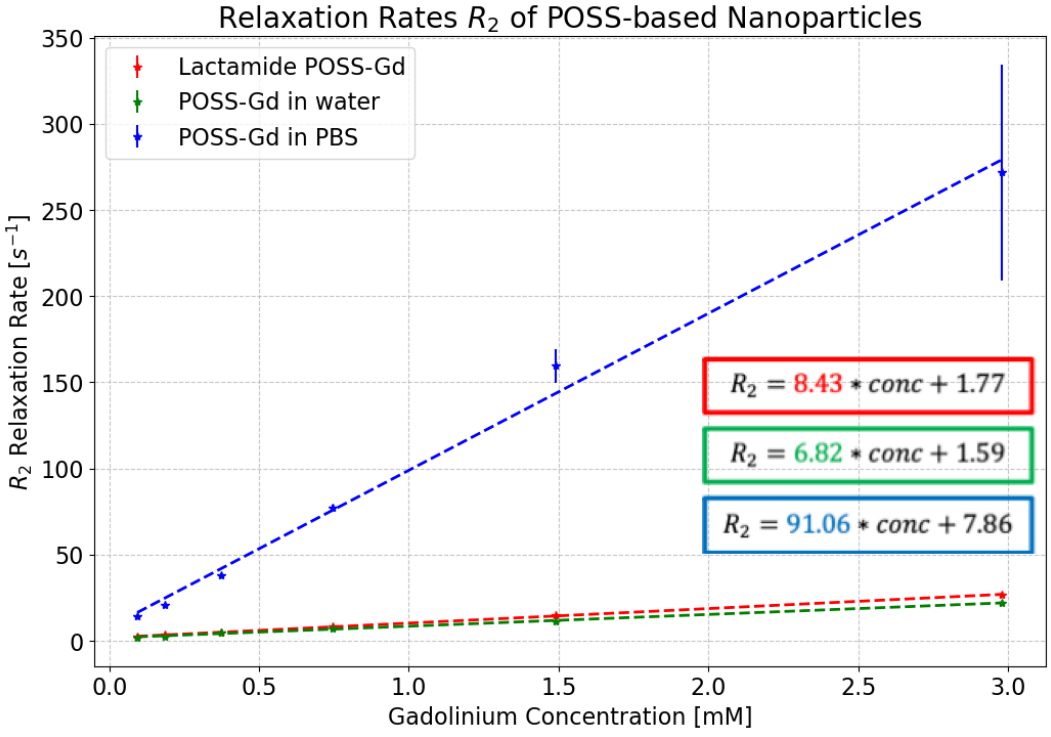

Figure 54: Dependence of relaxation rate R_2 on gadolinium concentration for POSS-Gd-based nanoparticles.

Based on the conducted POSS studies, it was found that molar relaxivities r_1 for POSS-based nanoparticles were: 2.48 ± 0.03 $mM^{-1}s^{-1}$ for Lactamide POSS-Gd, 1.89 ± 0.01 $mM^{-1}s^{-1}$ for POSS-Gd in water, 2.11 ± 0.01 $mM^{-1}s^{-1}$ for POSS-Gd in PBS, and 0.001 ± 0.0002 $mM^{-1}s^{-1}$ for POSS nanoparticles without gadolinium labeling. In turn, the obtained molar relaxivities r_2 were: 8.43 ± 0.06 $mM^{-1}s^{-1}$ for Lactamide POSS-Gd, 6.82 ± 0.21 $mM^{-1}s^{-1}$ for POSS-Gd in water, and 91.06 ± 3.76 $mM^{-1}s^{-1}$ for POSS-Gd in PBS. Due to the low r_1 effect in POSS nanoparticles, the analysis of these nanoparticles in order to determine r_2 value was abandoned.

8.1.4 Cerium Oxide-based Nanoparticles

The last type of nanoparticles analyzed were nanoparticles based on cerium oxide. Among them, the CeO2-Gd, CeO2, and CeO2-Gd-PAA nanoparticles can be distinguished. All mentioned nanoparticles were subjected to the filtration process through a 450 nm filter due to cell line testing. In this last case, adding polyacrylic acid (PAA) to the chemical structure should reduce the agglomeration of nanoparticles and improve biocompatibility. The Figure 55 below presents the T_1-weighted and T_2-weighted images of CeO2-Gd and CeO2 nanoparticles with additional CQD-Gd nanoparticles, analysed in previous subsection.

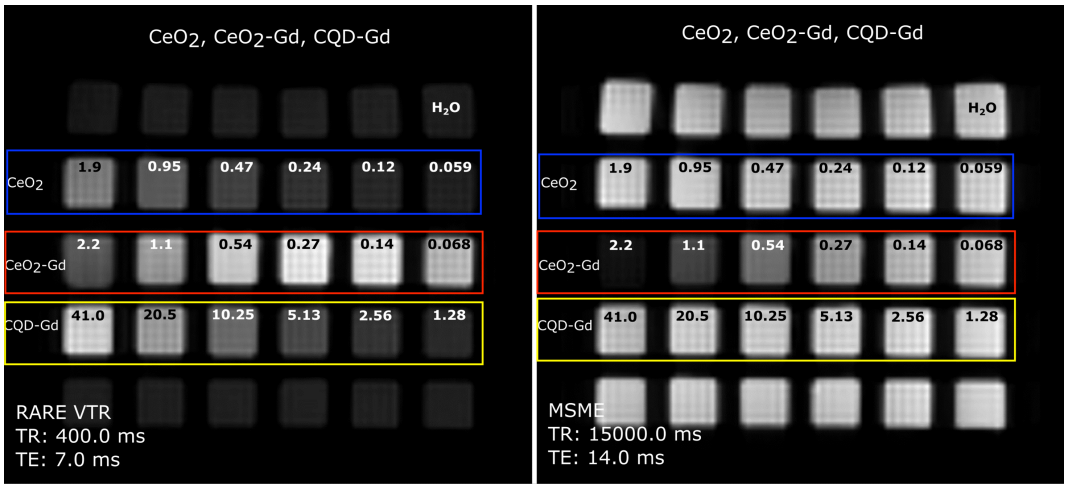

Figure 55: Example of obtained T_1-weighted (on the left) and T_2-weighted (on the right) images of CeO2-Gd, CeO2 and CQD-Gd nanoparticles with following parameters: RARE VTR (TR = 400 ms, TE = 7ms) and MSME (TR = 15000 ms and TE = 14 ms).

The Tables below provide the results of T_1 and T_2 relaxation times as well as the calculated R_1 and R_2 relaxation rates of ceria-based nanoparticles.

Table 18: Relaxation times T_1 and relaxation rates R_1 for CeO2-Gd-based nanoparticles.

Gadolinium concentration [mM]	**CeO2-Gd**		**CeO2-Gd-PAA**	
	T1 [ms]	**R1 [s^{-1}]**	**T1 [ms]**	**R1 [s^{-1}]**
0.512	56 ± 2	17.9 ± 0.63	962 ± 18	1.04 ± 0.02
0.256	106 ± 1	9.41 ± 0.04	1408 ± 20	0.71 ± 0.01
0.128	192 ± 1	5.22 ± 0.02	1852 ± 69	0.55 ± 0.02
0.064	313 ± 2	3.19 ± 0.02	2174 ± 142	0.47 ± 0.03
0.032	532 ± 3	1.89 ± 0.01	2500 ± 125	0.40 ± 0.02
0.016	893 ± 6	1.12 ± 0.01	2632 ± 139	0.39 ± 0.03
0.008	1370 ± 8	0.73 ± 0.01	-	-
0.004	1852 ± 7	0.55 ± 0.01	-	-

Table 19: Relaxation times T_1 and relaxation rates R_1 for CeO2 nanoparticles without gadolinium compounds.

Nanoparticle concentration [mM]	**CeO2**	
	T1 [ms]	**R1 [s^{-1}]**
1.89	565 ± 2	1.78 ± 0.01
0.95	893 ± 6	1.13 ± 0.01
0.47	1316 ± 14	0.76 ± 0.01
0.24	1786 ± 19	0.56 ± 0.01
0.12	2222 ± 15	0.45 ± 0.01
0.06	2564 ± 20	0.39 ± 0.01
0	2857 ± 24	0.35 ± 0.01

Table 20: Relaxation times T_2 and relaxation rates R_2 for CeO2-Gd nanoparticles.

Gadolinium concentration [mM]	**CeO2-Gd**	
	T1 [ms]	**R1 [s^{-1}]**
1.09	12 ± 1	82.76 ± 1.08
0.54	22 ± 1	44.85 ± 0.33
0.27	42 ± 1	23.69 ± 0.11
0.14	74 ± 1	13.51 ± 0.07
0.07	111 ± 1	8.99 ± 0.03
0.03	179 ± 1	5.59 ± 0.01
0.02	274 ± 1	3.66 ± 0.01
0.008	422 ± 1	2.38 ± 0.01
0.004	529 ± 1	1.89 ± 0.01
0	617 ± 1	1.63 ± 0.01

Table 21: Relaxation times T_2 and relaxation rates R_2 for CeO2-Gd-PAA nanoparticles.

Gadolinium concentration [mM]	**CeO2-Gd-PAA**	
	T1 [ms]	**R1 [s^{-1}]**
1.89	267 ± 1	3.76 ± 0.01
0.95	375 ± 1	2.68 ± 0.01
0.47	467 ± 1	2.14 ± 0.01
0.24	538 ± 1	1.87 ± 0.01
0.12	578 ± 1	1.73 ± 0.01
0.06	606 ± 1	1.65 ± 0.01
0	568 ± 1	1.76 ± 0.01

Using the obtained measurement results, a graph of the dependence of R_1 and R_2 on the concentration of gadolinium or nanoparticles was created and presented below.

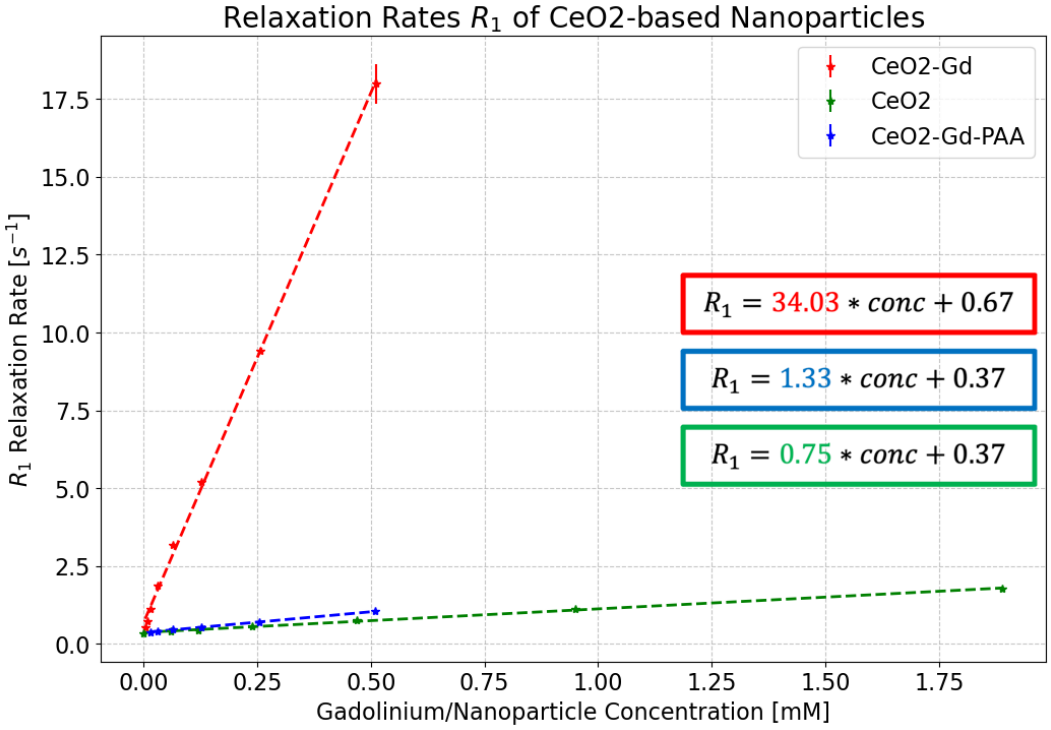

Figure 56: Dependence of relaxation rate R_1 on gadolinium or nanoparticle concentration for CeO2-based nanoparticles.

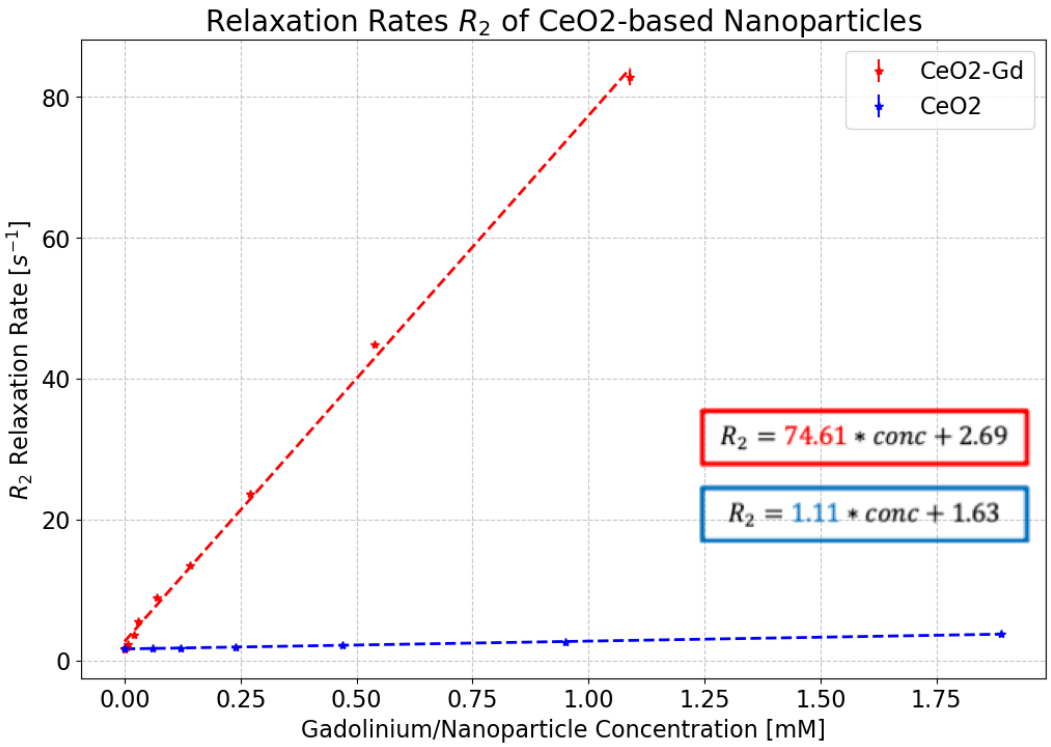

Figure 57: Dependence of relaxation rate R_2 on gadolinium or nanoparticles concentration for CeO2-based nanoparticles.

Based on these results, it can be concluded that the molar relaxivities r_1 were as follows: 34.03 $\pm$ 0.48 $mM^{-1}s^{-1}$ for $CeO_2 - Gd$, 0.75 $\pm$ 0.02 $mM^{-1}s^{-1}$ for CeO_2, and 1.33 $\pm$ 0.02 $mM^{-1}s^{-1}$ for $CeO_2 - Gd - PAA$. On the other hand, molar relavivities r_2 were as follows: 74.61 $\pm$ 1.12 $mM^{-1}s^{-1}$ for $CeO_2 - Gd$, and 1.11 $\pm$ 0.04 $mM^{-1}s^{-1}$ for CeO_2.

In this section, the focus is on the contrast properties of different nanoparticles. All obtained relaxivities r_1 and r_2 are presented in the table below.

Table 22: Obtained molar relaxivities r_1 and r_2 for investigated nanoparticles.

Nanoparticle	r_1 $[mM^{-1}s^{-1}]$	r_2 $[mM^{-1}s^{-1}]$
AOT/PLL 1xGd	3.65 ± 0.18	11.88 ± 1.33
AOT/PLL 2xGd	2.53 ± 0.03	15.49 ± 0.47
PCL 1xGd	3.65 ± 0.18	22.79 ± 1.84
PCL 2xGd	3.28 ± 0.03	16.81 ± 0.28
CQD-Gd	0.09 ± 0.0004	0.13 ± 0.0003
Lactamide POSS-Gd	2.48 ± 0.03	8.43 ± 0.06
POSS-Gd in water	1.89 ± 0.01	6.82 ± 0.21
POSS-Gd in PBS	2.11 ± 0.01	91.06 ± 3.76
POSS	0.001 ± 0.0002	-
CeO2-Gd	34.03 ± 0.48	74.61 ± 1.12
CeO2	0.75 ± 0.02	1.11 ± 0.04
CeO2-Gd-PAA	1.33 ± 0.02	-

8.2 Optimization of MCAO Induction and MRI Analysis

8.2.1 Deep Learning Skull Stripping

The MRI image data analysis consists of several preprocessing processes. One of the most important process is extracting the brain from the image. This is known as a skull stripping. This is an extremely time-consuming process and depends on human knowledge, because this operation encounters challenges related to low contrast in the image, differences in the image resolution and blurred boundaries between the brain and other tissues. Therefore, it is extremely important to use good tool for brain extraction purposes, especially when a larger number of animals are analysed. The use of deep neural network algorithms can be a great help in this type of preprocessing operations.

The RS^2-Net architecture is a neural network based on the Swin-UNETR network, which was trained on 1037 rats and 1142 images from 89 preclinical research centers. The network was proposed by Lin Y. et al. [103]. The Figure 58 below presents a whole used framework.

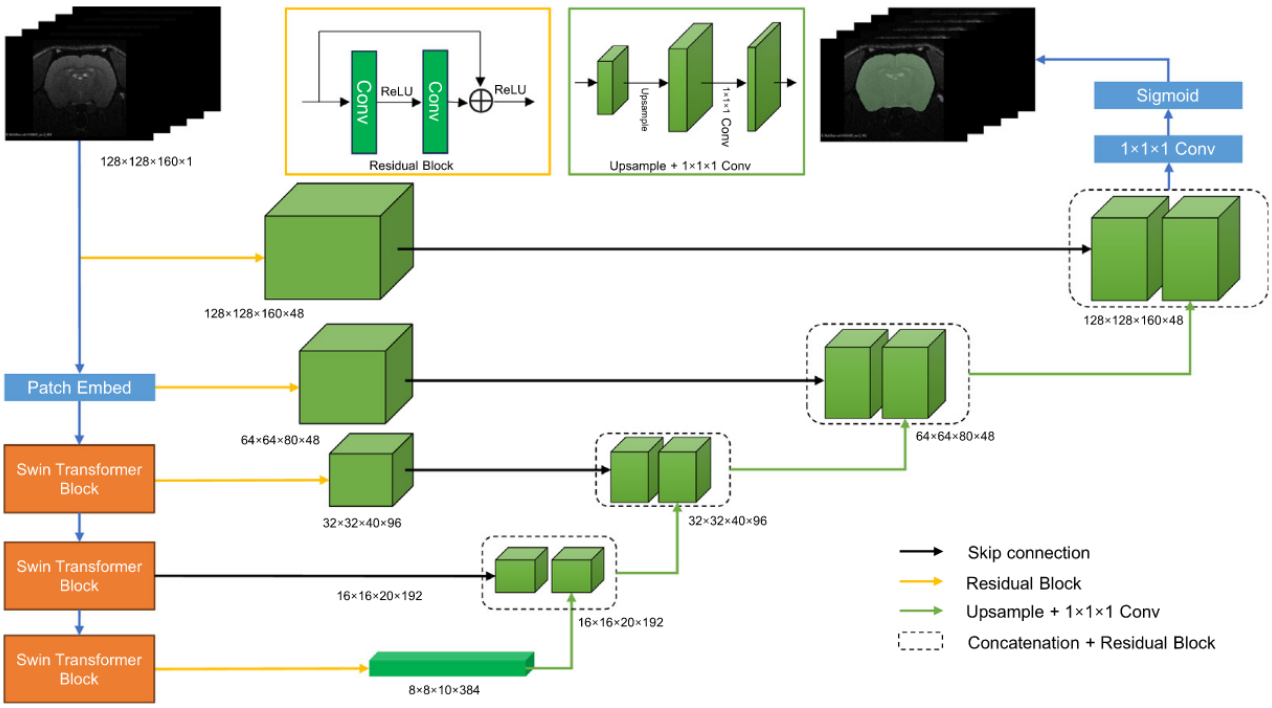

Figure 58: A framework of the used model. The image size after data augmentation is 128 x 128 x 160 and it is input to the Patch Embed layer in the Swin Transformer module and a Residual Block respectively. The features obtained from Swin Transformer are input in next step. After obtaining an output with size 128 x 128 x 160 x 48, it is concatenated with the first Residual Block's output and then go through Conv Layer and Sigmoid to get final segmentation result. Reprinted with permission from [103].

The entire described deep learning framework architecture has been included in the GitHub repository: https://github.com/VitoLin21/Rodent-Skull-Stripping.

In the model described by Lin Y., Transformer Swin is used to extract features from an image. It replaces the multi-head self attention block (MCA) by window-based multi-head self attention (W-MSA) and shifted window-based multi-head self attention (SW-MSA). In the W-MSA block, image is divided to non-overlapping windows and then self-attention is calculated in each window. Oh the other hand, in SW-MSA block, the window is shifted to introduce connections and relations between windows. The multi-layer perceptron (MLP) consists fully connected layers with GELU activation functions. It is used to integrate features from W-MSA and SW-MSA. The Swin Transformer Block is presented on Figure 59 below.

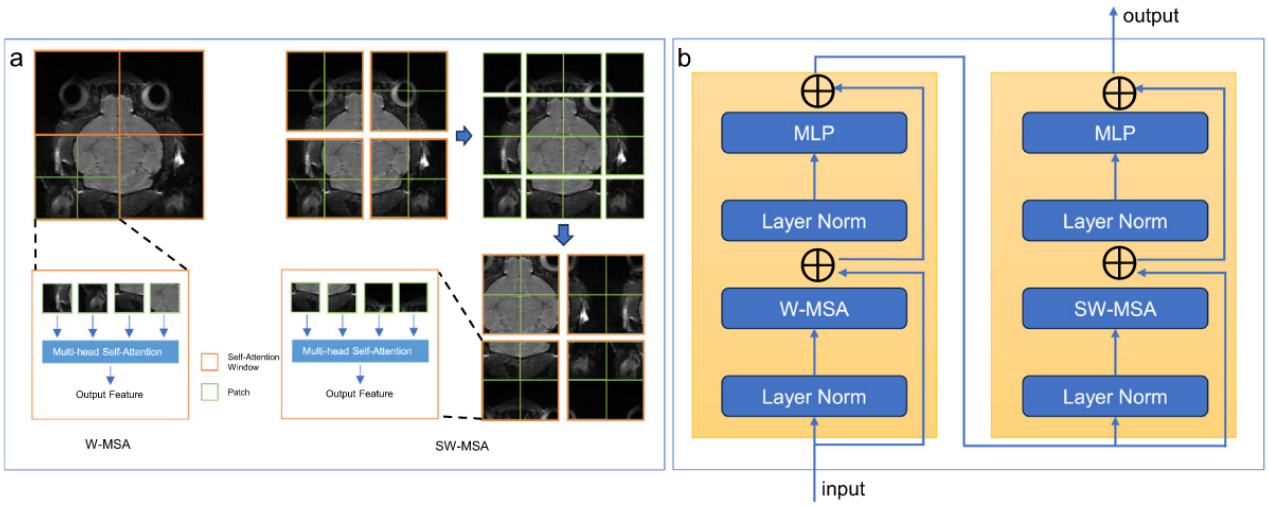

Figure 59: Structure of the Swin Transformer Block. Reprinted with permission from [103].

The MRI image data were converted to *.nii.gz* format using the *brkraw* tool [104], which allows access to data obtained from ParaVision software. Then, tha image data were appropriately rotated and flipped to ensure correct orientation and position. This data was fed into a neural network to create a binary mask of the brain. This mask was finally overlayed on the original image. Mask prediction was performed on the NVIDIA GeForce RTX 4070 graphics card. Below is an example of the resulting mask with the extracted brain.

Figure 60: The result of MCAO 8 rat brain extraction using neural network.

In order to quantitatively evaluate the segmentation process, the Dice coefficient was used. The formula for this coefficient is presented below:

$$Dice\ Coefficient = \frac{2\times \mid G \cap P \mid}{\mid G \mid + \mid P \mid} \tag{67}$$

where P is the result of image segmentation using a neural network model and G is the area manually drawn as the ground truth brain region. The coefficient takes values from 0 to 1. The higher value, the better segmentation quality. The Table below presents the results of the Dice coefficients for all rats.

Table 23: Dice coefficients of TurboRARE and DTI_EPI images from all rats after 24h-post MCAO.

Rat Name	**Dice Coefficient TurboRARE [%]**	**Dice Coefficient DTI_EPI [%]**
MCAO 0	97	53
MCAO 1	84	67
MCAO 2	93	63
MCAO 3	98	73
MCAO 4	98	43
MCAO 5	98	61
MCAO 6	98	66
MCAO 7	99	64
MCAO 8	99	73

Segmentation and dice coefficient were performed 24 hours after MCAO procedure, using deep learning framework and calculating accuracy on single brain slice.

Based on the above table, it can be seen that segmentation using deep learning method gives very good results for T_2-weighted images using the TurboRARE protocol. However, the diffusion measurements have worse results. Nevertheless, this study shows usefulness of deep learning for the proper analysis of MRI data, including animals with the MCAO model. Having a properly extracted mask is crucial, because it allows to be applied to different scans and different images. This is certainly an area that is worth spending time on future studies to allow make segmentation on all types of MRI images.

8.2.2 Volumetric Stroke Analysis of the Preliminary MCAO

The second stage of *in vivo* studies was the volumetric measurements of stroke size in rat brain in order to optimize induction of the MCAO stroke for further studies. At this stage, T_2-weighted pilot images obtained from TurboRARE protocol in the coronal plane were used, with following parameters: $T_E = 31.50$ ms, $T_R = 2500$ ms, RARE Factor = 8, 15 slices with thickness of 0.8 mm each. MRI imaging was performed 24 hours after the MCAO stroke induction. In each of the obtained image slices, the stroke area was manually outlined, because it was clearly visible. The Figure 61 below shows sample T_2-weighted images of a rat with stroke in different planes.

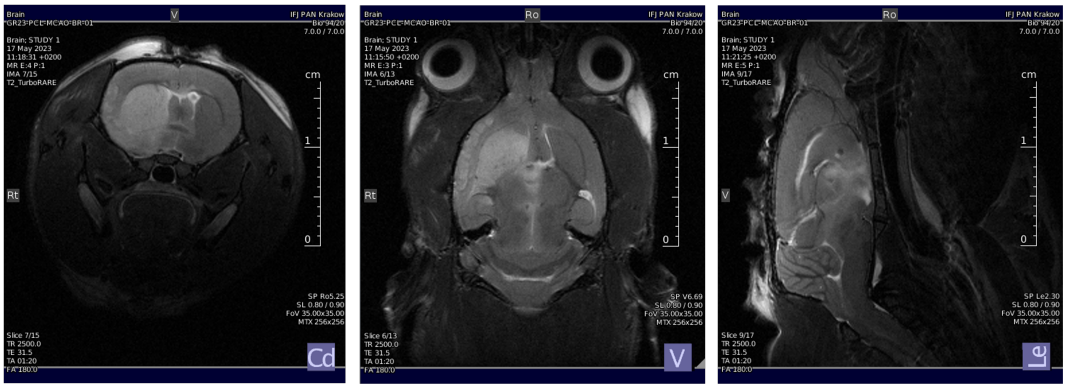

Figure 61: T_2-weighted images of MCAO 6 rat brain with stroke, obtained with TurboRARE protocol in different planes.

In order to calculate the stroke size, the pixel dimensions, image slice thickness and the number of pixels in the stroke area and whole brain were used. The resolution in all measurements was the same and was equale 0.137 x 0.137 mm. The Table 24 below presents the obtained stroke dimensions, the dimensions of the whole brain, as well as the ratio of the ischemic lesion to the whole brain volume for each of the tested rats.

Table 24: Results of volumetric measurements of rats with the MCAO model. Rats were divided into groups based on the size of the stroke. The CON group is the control group.

Rat Name	**Stroke Volume [mm^3]**	**Brain Volume [mm^3]**	**Ratio [%]**	**MRI Stroke Group**
MCAO 0	-	1315 ± 64	-	CON
MCAO 1	86 ± 4	1341 ± 67	6.4	I
MCAO 2	192 ± 10	1206 ± 60	15.9	II
MCAO 3	31 ± 2	1323 ± 66	2.4	I
MCAO 4	182 ± 9	1225 ± 61	14.9	II
MCAO 5	42 ± 2	1283 ± 64	3.3	I
MCAO 6	388 ± 19	1337 ± 67	29.1	III
MCAO 7	348 ± 17	1282 ± 64	27.1	III
MCAO 8	68 ± 3	1235 ± 62	5.5	I

The errors of determining the volume of the stroke and brain area were determined using the propagation of uncertainty law with this equation:

$$u(V) = \sqrt{P^2 d^2 u^2(N)} \tag{68}$$

where P is a pixel area, d is a slice thickness and $u(N)$ is the uncertainty in the pixel count, assumed as 5% due to the manually determined stroke and whole brain area. Based on the obtained results, it can be seen that the stroke sizes are different and it is possible to assign each rat to one of three MRI Stroke Groups, based on the ratio of the stroke area to the healthy area. The first group is the ratio up to 10%, the second group 11 - 20% and the third above 21%. The MCAO 0 rat was assigned to the *CON* category, because it was a healthy, control rat. The Table 25 below provides statistical metrics for each of the three groups.

Table 25: Statistic metrics of each MRI Stroke Group.

MRI Stroke Group	**Mean Stroke Volume [mm^3]**	**Median Stroke Volume [mm^3]**	**Mean Brain Volume [mm^3]**	**Mean Ratio [%]**
I	57 ± 25	55	1295	4.4
II	187 ± 7	187	1216	15.4
III	368 ± 29	368	1310	28.1

This studies were performed for optimisation of the stroke induction procedure. In further studies, the optimised MCAO procedure was used generating strokes belonging to the group number III.

8.2.3 MRI Parametric Map Analysis

An important part of the MRI preclinical imaging of the MCAO rats model was the stroke model characterization. To achieve this goal, the T_1, T_2, ADC images were obtained in the rat brain. The MSME sequence was used to obtain T_2-weighted images. The DTI_EPI protocol was used to obtain ADC diffusion images. In turn, T_1 images were obtained using ASL methodology, using the FAIR_EPI protocol. The Figures 62, 63, 64 below show an example of T_1-weighted, T_2-weighted and diffusion-weighted images.

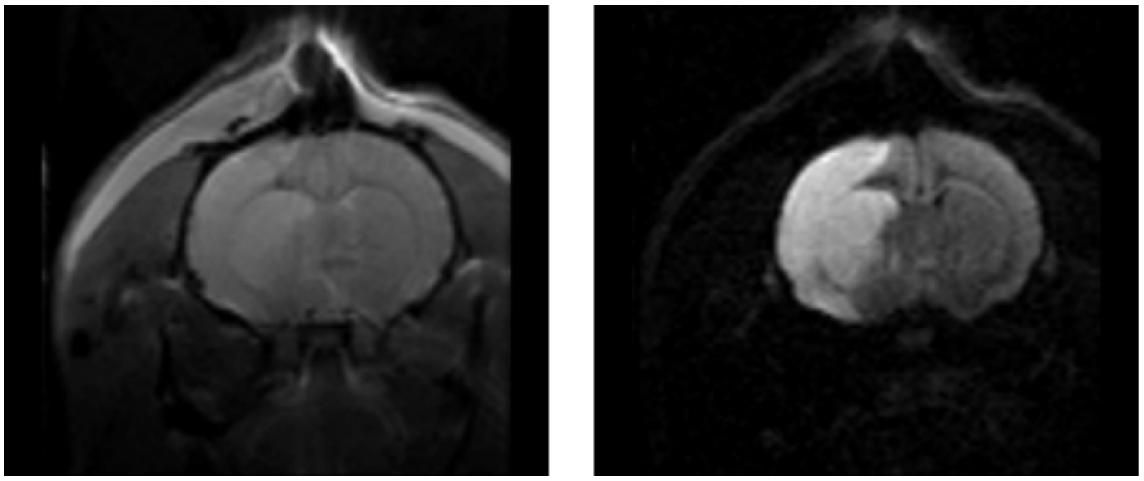

Figure 62: Diffusion-weighted images of rat MCAO 7 brain obtained from DTI_EPI protocol. On the left image A_0 image without diffusion gradient was presented. On the right side, diffusion weighted image with b = 1437 s/mm^2 was presdented. The image sequence parameters: T_R = 3000 ms, T_E = 21,5 ms.

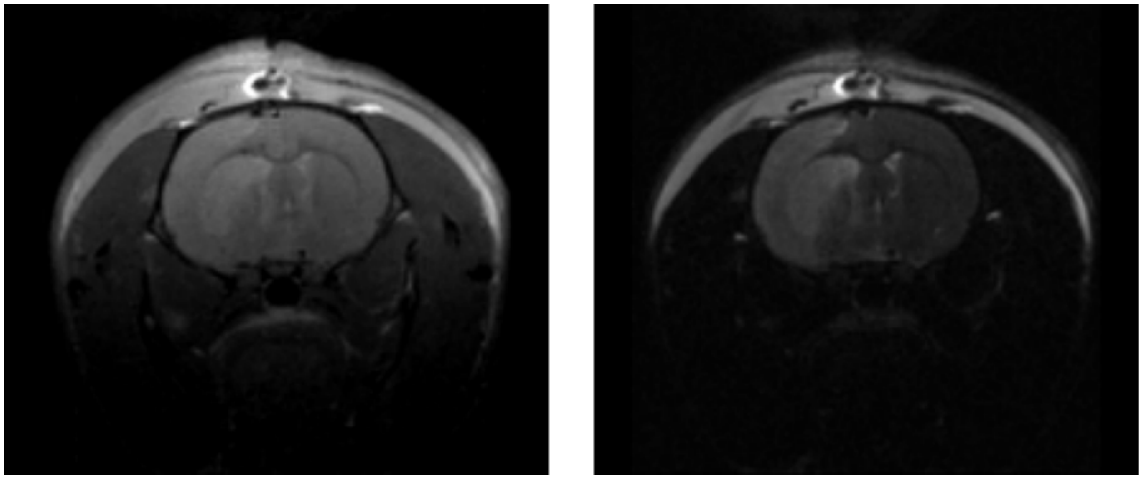

Figure 63: The T_2-weighted images obtained from MSME protocol of rat MCAO 7 brain. The image sequence parameters: T_R = 2200 ms, T_E = 7 ms on the left image and T_E = 56 ms on the right image.

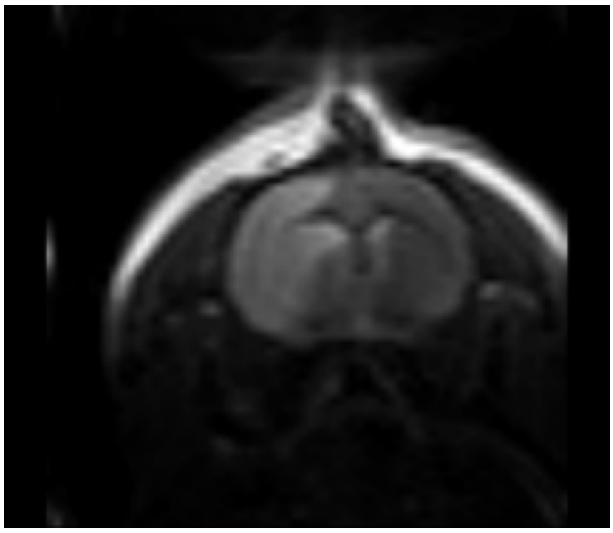

Figure 64: The T_1-weighted MCAO 7 brain image obtained via ASL method with FAIR_EPI imaging protocol. The image sequence parameters: T_R = 10816,3 ms, T_E = 17,5 ms.

The above images were obtained 24 hours after MCAO stroke induction. In the case of diffusion studies, it can be seen that for A_0 image (image without diffusion gradients) T_2 weighting occurs. In contrast, when the b-value is set, the effect of diffusion in the brain is visible, allowing to distinct the stroke area and healthy brain tissue area. In the stroke region, the signal is higher than in the healthy tissue region. For T_2-weighted imaging, the stroke region is also brighter. A similar situation occurs in T_1-weighted imaging using ASL technique.

For quantitative analysis of the obtained images, T_1, T_2, diffusion and perfusion maps were calculated. The T_2 and diffusion (ADC) maps were determined using exponential decay of signal for successive T_E and b-values, respectively. In turn, water in arterial blood was used as a natural marker in the case of perfusion maps. Magnetic labeling of water molecules in arteries occurs before blood reaches the brain. Imaging is then performed after a specified T_I inversion time to allow the labeled blood to reach the brain. Comparison two T_1-weighted images allows for determining the signal difference, which is proportional to brain perfusion. The folowing Figures 65, 66, 67, 68 show the T_1, T_2, diffusion and perfusion maps in the rat brain with the applied MCAO model.

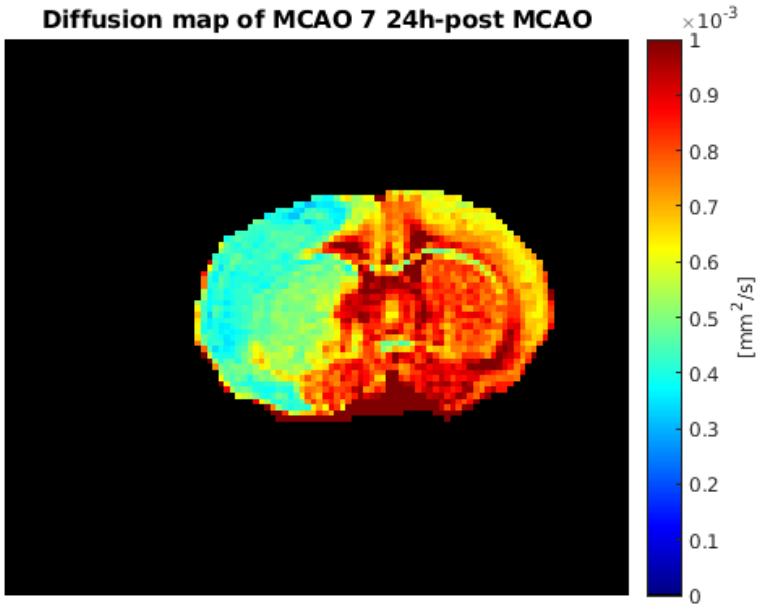

Figure 65: The diffusion map of rat brain with MCAO model.

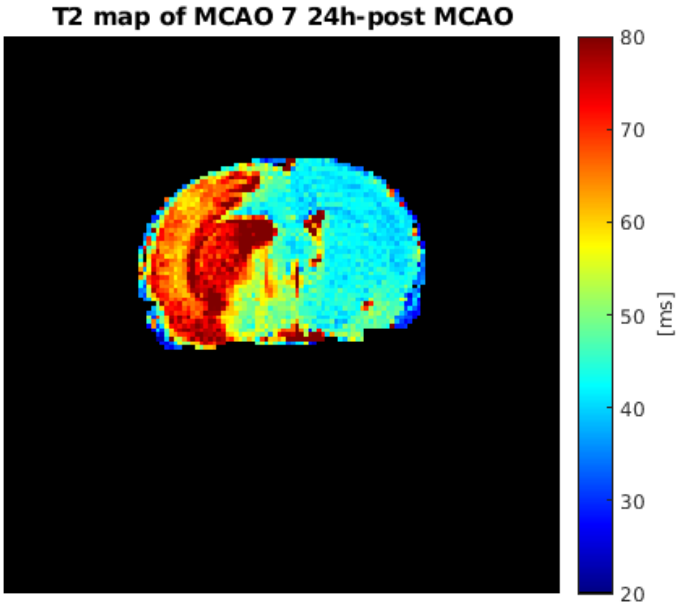

Figure 66: The T_2 relaxation time map of rat brain with MCAO model.

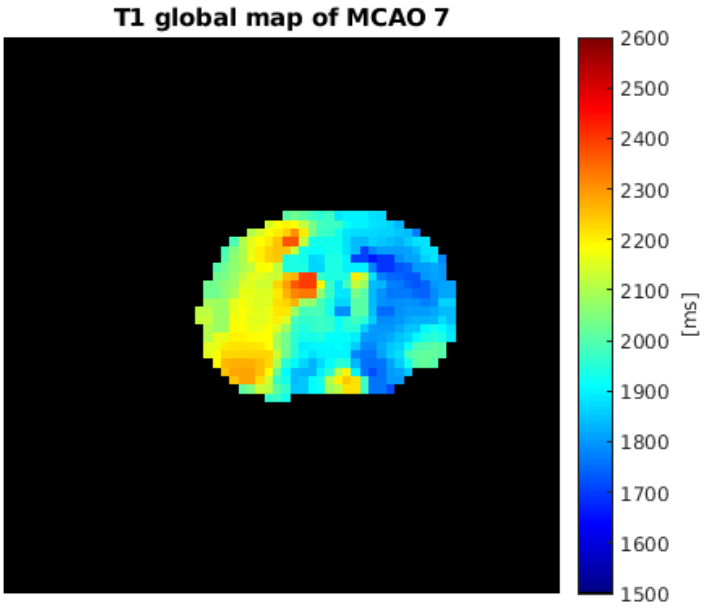

Figure 67: The T_1 relaxation time map of rat brain with MCAO model.

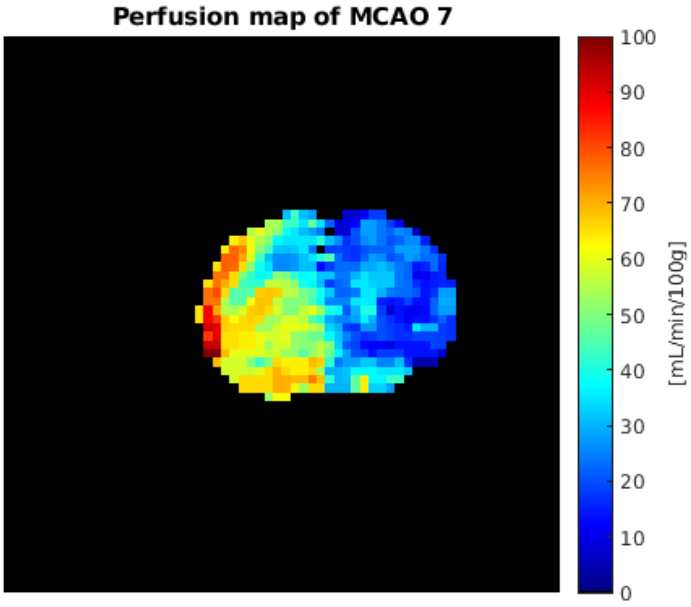

Figure 68: The perfusion map of rat brain with MCAO model.

In the above maps, manual brain extraction (skull-stripping) was performed using a MATLAB script. The presented maps show the same anatomical slice of the brain. In clinical practice, diffusion-perfusion imaging is used to find a mismatch , which defines the penumbra area [102]. The penumbra is an area, where stroke damage is reversible. This is the area of brain tissue surrounding the ischemic core. The results of T_1 and T_2 relaxation times, as well as diffusion

and perfusion in the stroke and healthy areas are presented as a box plots in the Figures 69, 70, 71, 72 below.

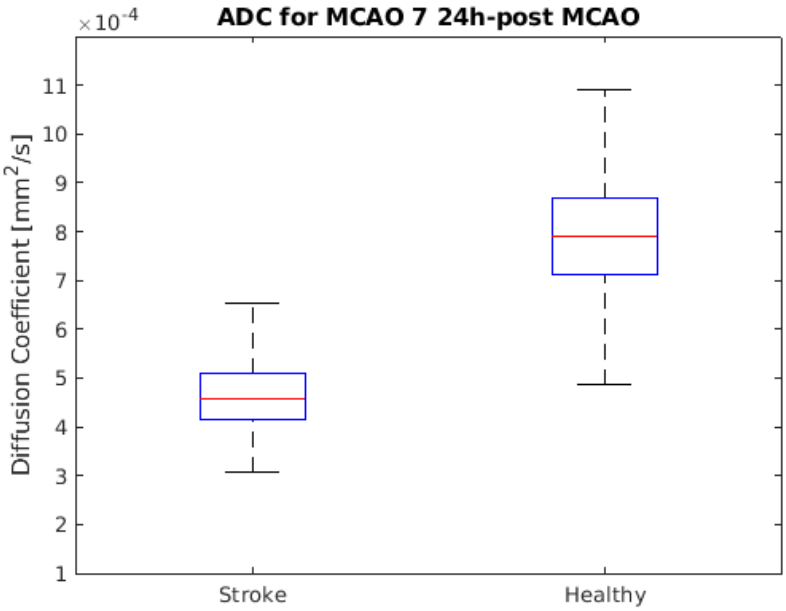

Figure 69: The box plot of ADC values in stroke and healthy brain tissue.

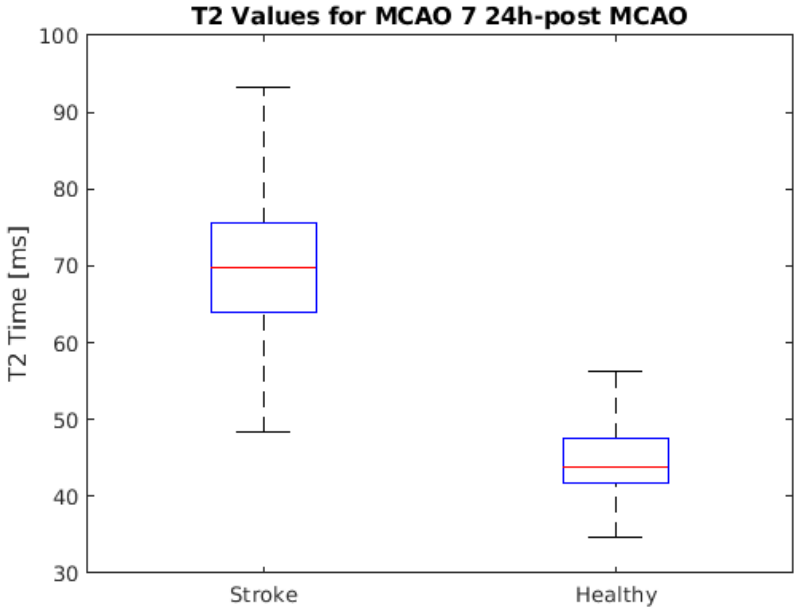

Figure 70: The box plot of T_2 relaxation times values in stroke and healthy brain tissue.

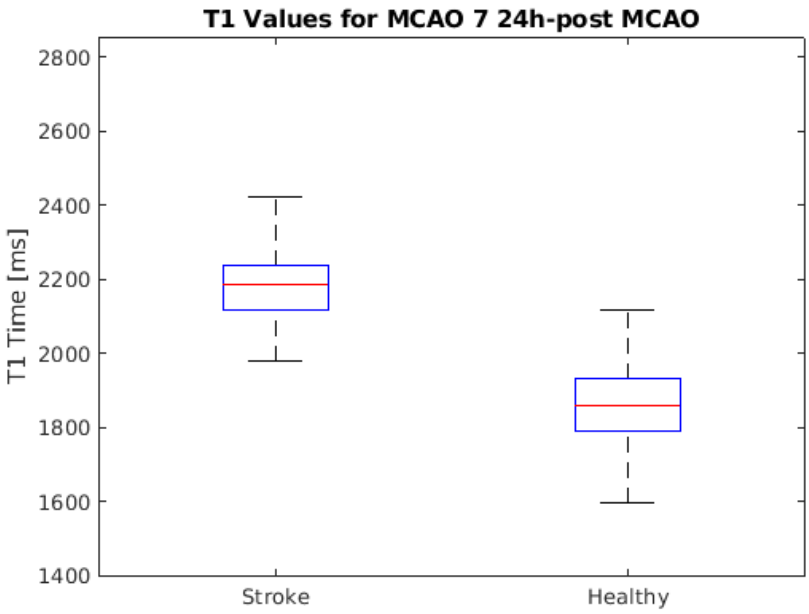

Figure 71: The box plot of T_1 relaxation times values in stroke and healthy brain tissue.

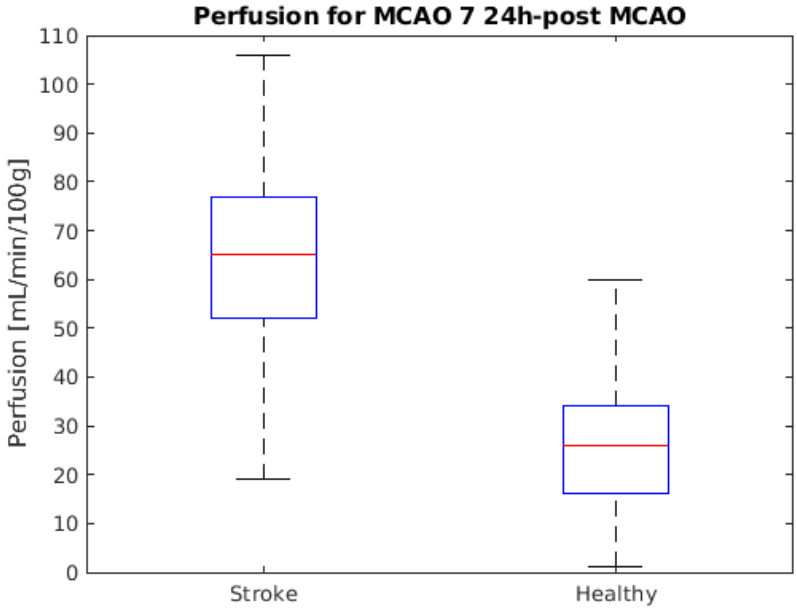

Figure 72: The box plot of perfusion values in stroke and healthy brain tissue.

In the above analysis, the stroke area and healthy tissue were marked by hand on the obtained maps. The box plots allow determining the median, first and third quartiles and the maximum and minumum values.

Based on the obtained graphs, it can be noted that in the stroke area T_1 and T_2 relaxation times values increase due to edema. Edema causes an increase in the amount of water in the extracellular space, which leads to increase relaxation times and it is visible on T_1- and T_2-

weighted images. In turn, diffusion in stroke area is lower. This is result of cytotoxic edema. This results in decrease in water mobility in stroke tissue and it is also visible on diffusion-weighted images, especially for higher b-values. On the other hand, perfusion in the stroke area is higher, which may be result of reperfusion, because during the MCAO induction procedure, the cerebral artery was closed for some time. After its opening, an attempt is made to repair ischemic damage by increasing perfusion.

Above description is the analysis of the MCAO 7 rat, while a similar analysis was performed for the MCAO 0 rat, which was the healthy control rat. The T_1, T_2, diffusion and perfusion images of the healthy rat with the corresponding maps were presented below on Figure 73.

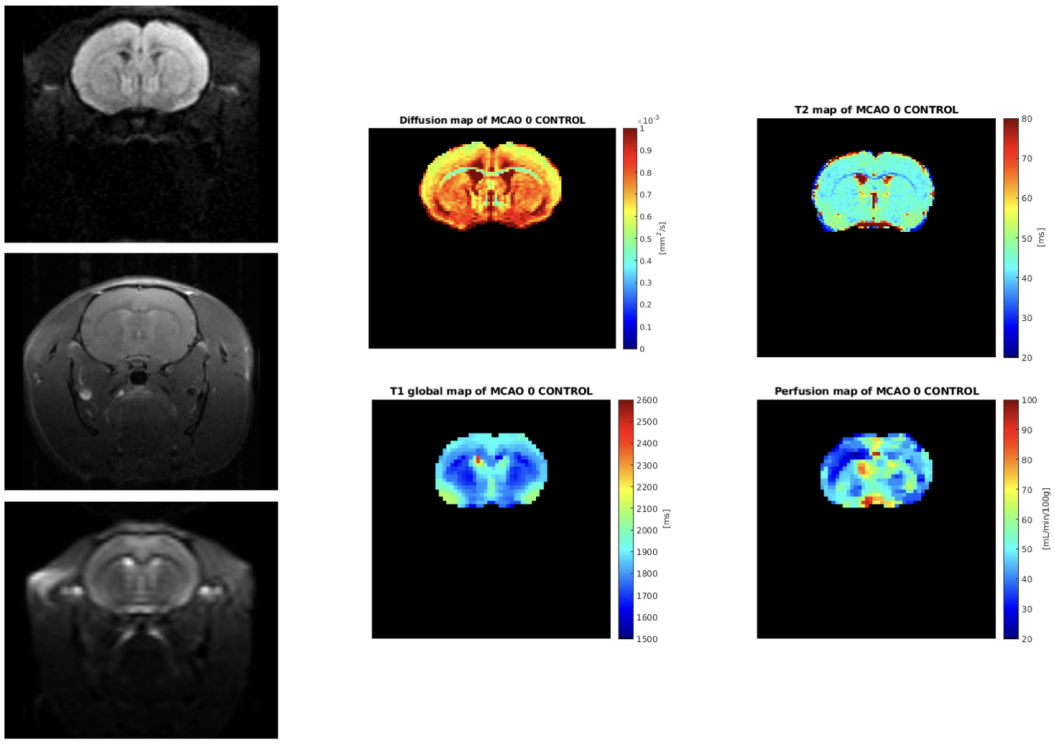

Figure 73: The DWI, T_2-weighted and T_1-weighted images of control healthy rat on the left. Corresponding ADC, T_2, T_1 and perfusion maps on the right side. The image sequence parameters: DTI_EPI (T_R = 3000 ms, T_E = 21,5 ms), MSME (T_R = 2200 ms, T_E = 7,0 ms), FAIR_EPI (T_R = 10816,3 ms, T_E = 17,5 ms).

The characterization of the MCAO model used is crucial to deliver theranostic agents to the brain. The analysis presented in this section was the first step in the characterization process of the ischemic stroke model. It allowed to answer the question of how stroke affects the relaxation times, diffusion and perfusion in brain.

8.3 Diffusion Temporal Evolution

Diffusion in the ischemic stroke brain is one of the key physical and chemical quantities [105] [106]. It is measured in clinical studiec to assess the size of the stroke and penumbra area. It turns out, that diffusion coefficient evolves over time in the ischemic region tissue [107]. Therefore, another set of animals was prepared and DWI imaging was performed at different time intervals after occlusion. These animals are presented in the Table below.

Table 26: Animal set prepared for ADC evolution studies.

Rat Name	**DTI Days After MCAO**
MCAO E	1, 3, 5, 7, 9, 11
MCAO F	1, 3, 5, 7, 9, 11
MCAO G	1, 3, 7, 9, 11

For these studies, diffusion was measured using an EPI sequence with T_E equals 20.5 ms and T_R equals 3000 ms. Diffusion was measured in 9 directions with five b-values in range from 200 s/mm^2 to 1500 s/mm^2. The image size was 96x96 and the FOV was 30x30 mm. FOV saturation was also used to limit diffusion signal originating from outside the brain. DWI imaging with different b-values allowed to calculate ADC diffusion coefficients using diffusion tensor trace. Based on this, diffusion maps were generated for each measurement point after occlusion for each slices. The resulting maps for an example rat are presented on the Figure 74 below.

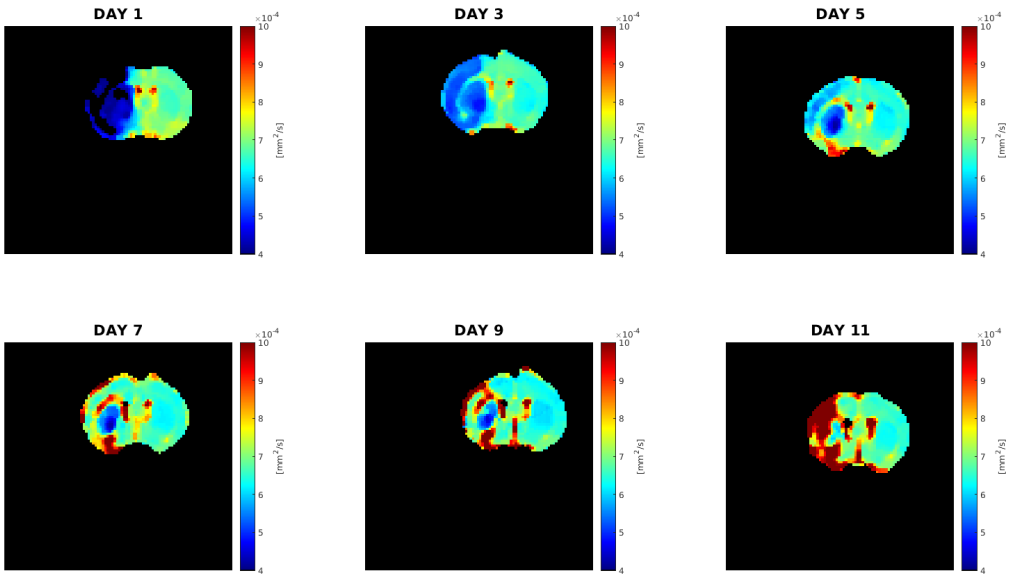

Figure 74: ADC maps of rat MCAO E in different time points after MCAO occlusion.

Registration was used on the diffusion maps to make these results in different time points more comparable. These maps show that diffusion in the ischemic region changes over time and increases. However, a quantitative analysis is required here. Therefore, the machine learning GMM (Gaussian Mixture Model) was used to assess the diffusion. This is a probabilistic unsupervised learning model, which describes a normally distributed subpopulation in the entire population. The model learns to which subpopulation, a given data point belongs. This algorithm uses a multimodal Gaussian distribution, which fits to a given data distribution. It is parameterized by component weights, component means and variances. For a GMM with K components, k_{th} component have a mean μ_k and variance σ_k. The mixture component weights are defined as ϕ_k.

$$p(x) = \sum_{i=1}^{K} \phi_i N(x|\mu_i, \sigma_i) \tag{69}$$

$$N(x|\mu_i, \sigma_i) = \frac{1}{\sigma_i\sqrt{2\pi}} exp(-\frac{(x-\mu_i)^2}{2\sigma_i^2}) \tag{70}$$

$$\sum_{i=1}^{K} \phi_i = 1 \tag{71}$$

For diffusion studies, the GMM model was used to estimate the temporal evolution of the mean brain diffusion. Using previously calculated ADC maps, histograms of diffusion values were created. An example of a histogram was presented on Figure 75 below.

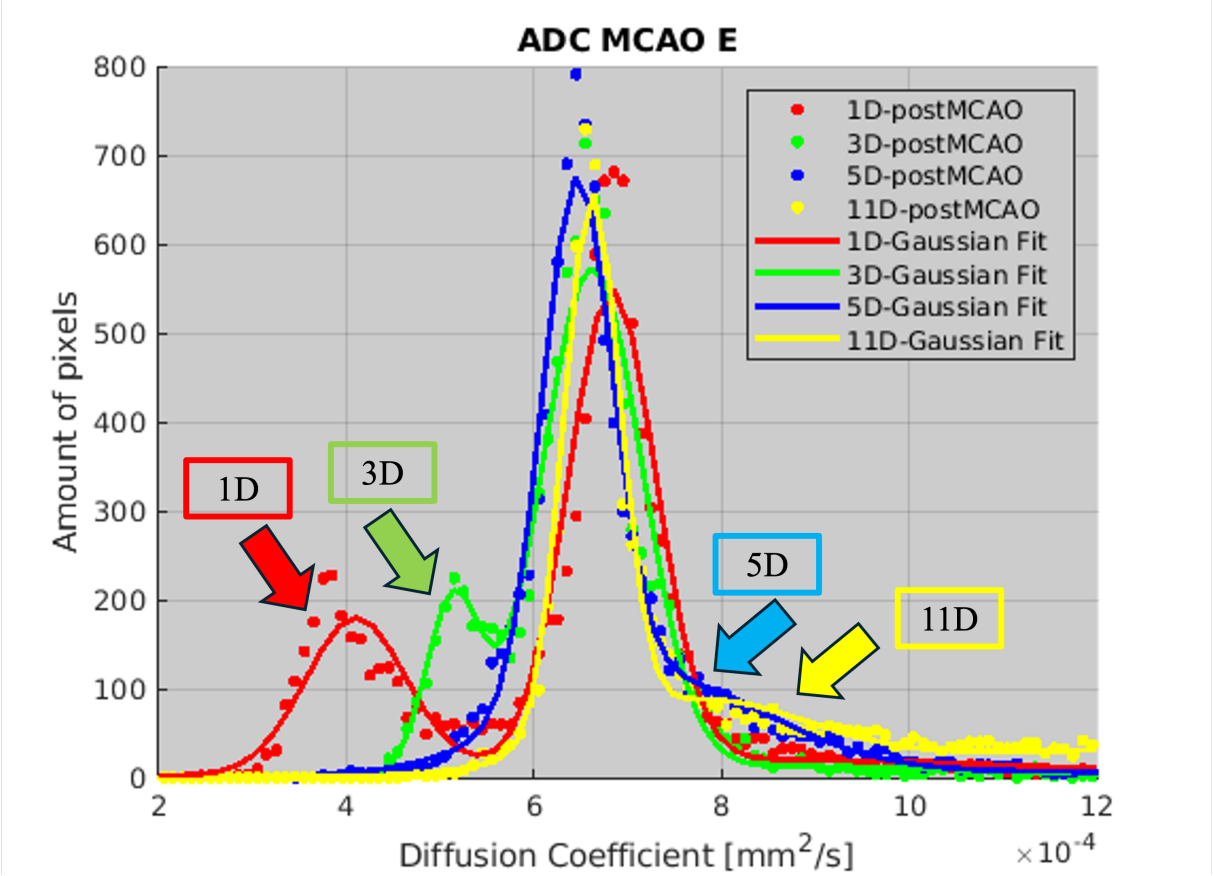

Figure 75: ADC histograms of MCAO E rat with GMM result. There are four histograms for four time points after occlusion. The arrows indicate the evolving first component, which is responsible for the ischemic region.

Based on obtained histogram, it was possible to fit trimodal Gaussian distribution, a sum of three Gaussian curves (for each tested animal). Using GMM, Gaussian curves were fitted to the ADC distribution in the rat brain. The first Gaussian curve describes ADC values in the ischemic area, the second in the healthy tissue area, while the third component describes ADC values from brain ventricles (CSF). It was observed that the mean of the first component, the stroke component, changes over time after oclusion and increases. The first component moves to the right side of the histogram ultimately exceeding the ADC value in healthy tissue. The Tables and Figures below provide the mean ADC results for each GMM component for all tested rats.

Table 27: The mean ADC results for all GMM components for rat MCAO E.

MCAO E			
Days After MCAO	**ADC Stroke** $[*10^{-3}mm^2/s]$	**ADC Healthy** $[*10^{-3}mm^2/s]$	**ADC CBF & Scar** $[*10^{-3}mm^2/s]$
1	0.41 ± 0.05	0.68 ± 0.05	0.85 ± 0.29
3	0.51 ± 0.03	0.66 ± 0.05	0.88 ± 0.22
5	0.72 ± 0.13	0.65 ± 0.04	1.13 ± 0.32
7	0.75 ± 0.13	0.65 ± 0.03	1.13 ± 0.29
9	0.74 ± 0.13	0.63 ± 0.03	1.22 ± 0.22
11	0.74 ± 0.13	0.63 ± 0.03	1.22 ± 0.33

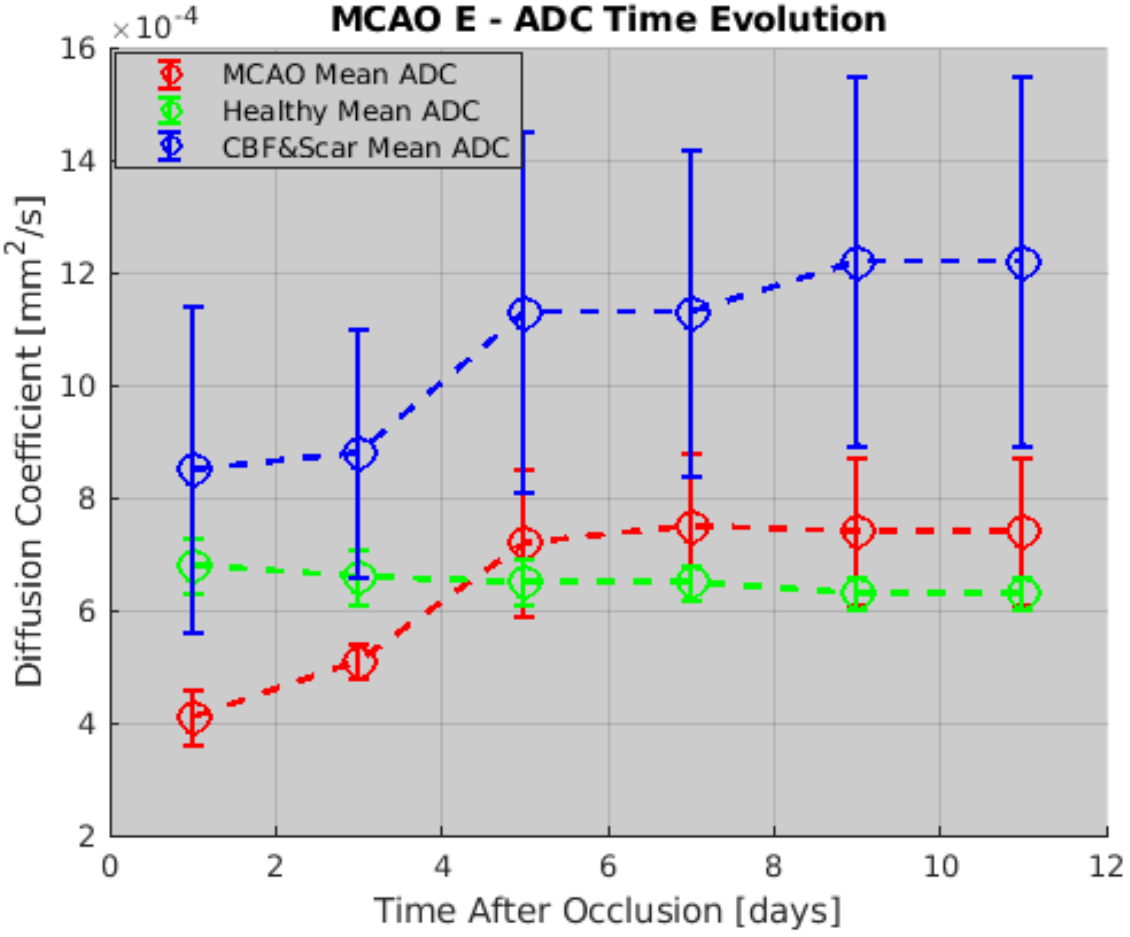

Figure 76: Mean ADC time evolution for rat MCAO E.

Table 28: The mean ADC results for all GMM components for rat MCAO F.

MCAO F			
Days After MCAO	**ADC Stroke** $[*10^{-3}mm^2/s]$	**ADC Healthy** $[*10^{-3}mm^2/s]$	**ADC CBF & Scar** $[*10^{-3}mm^2/s]$
1	0.46 ± 0.05	0.65 ± 0.05	0.94 ± 0.31
3	0.52 ± 0.03	0.64 ± 0.04	0.81 ± 0.22
5	0.72 ± 0.11	0.67 ± 0.03	1.09 ± 0.29
7	0.71 ± 0.12	0.63 ± 0.03	1.14 ± 0.31
9	0.74 ± 0.13	0.64 ± 0.03	1.15 ± 0.29
11	0.76 ± 0.14	0.63 ± 0.03	1.27 ± 0.34

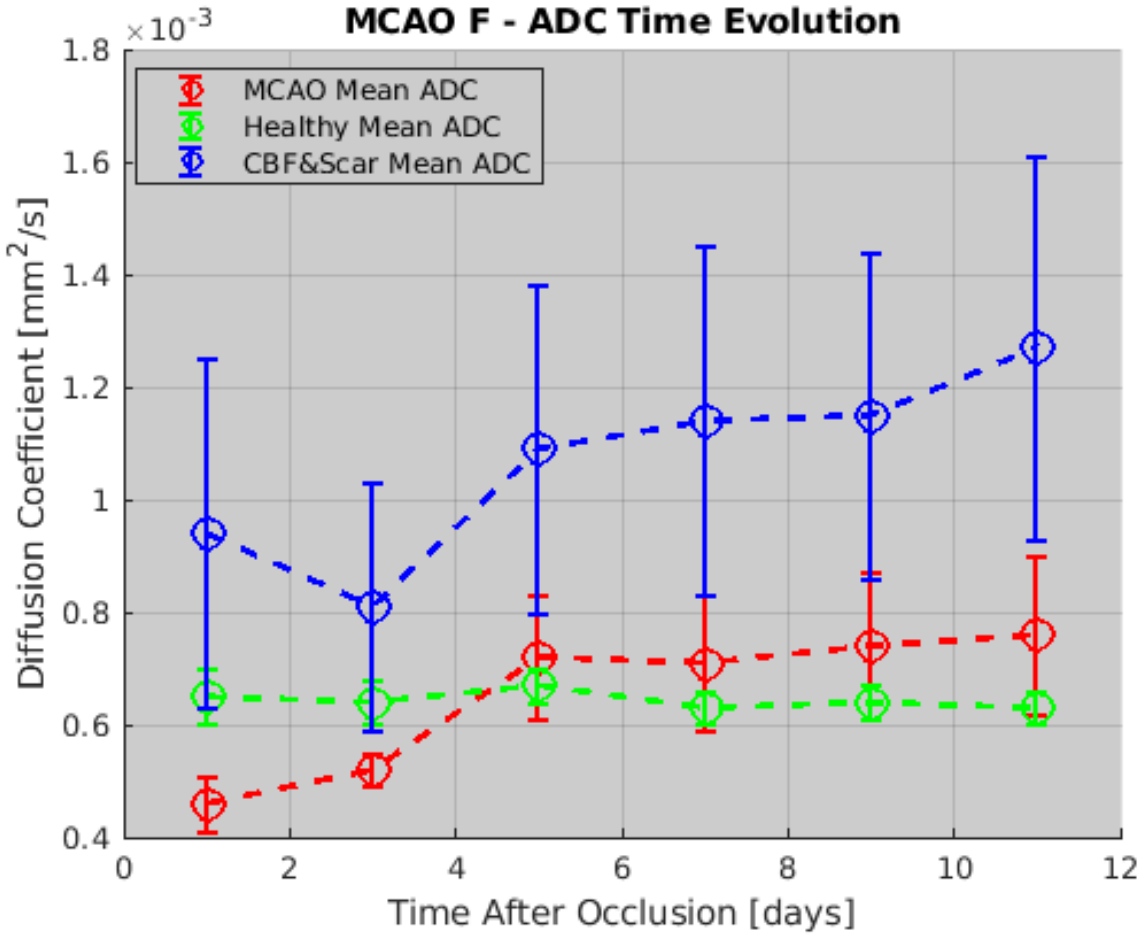

Figure 77: Mean ADC time evolution for rat MCAO F.

Table 29: The mean ADC results for all GMM components for rat MCAO G.

MCAO G			
Days After MCAO	**ADC Stroke** $[*10^{-3}mm^2/s]$	**ADC Healthy** $[*10^{-3}mm^2/s]$	**ADC CBF & Scar** $[*10^{-3}mm^2/s]$
1	0.49 ± 0.03	0.63 ± 0.05	0.75 ± 0.16
3	0.69 ± 0.11	0.66 ± 0.03	1.02 ± 0.29
7	0.73 ± 0.14	0.63 ± 0.03	1.16 ± 0.32
9	0.80 ± 0.15	0.67 ± 0.04	1.28 ± 0.31
11	0.82 ± 0.14	0.64 ± 0.04	1.25 ± 0.31

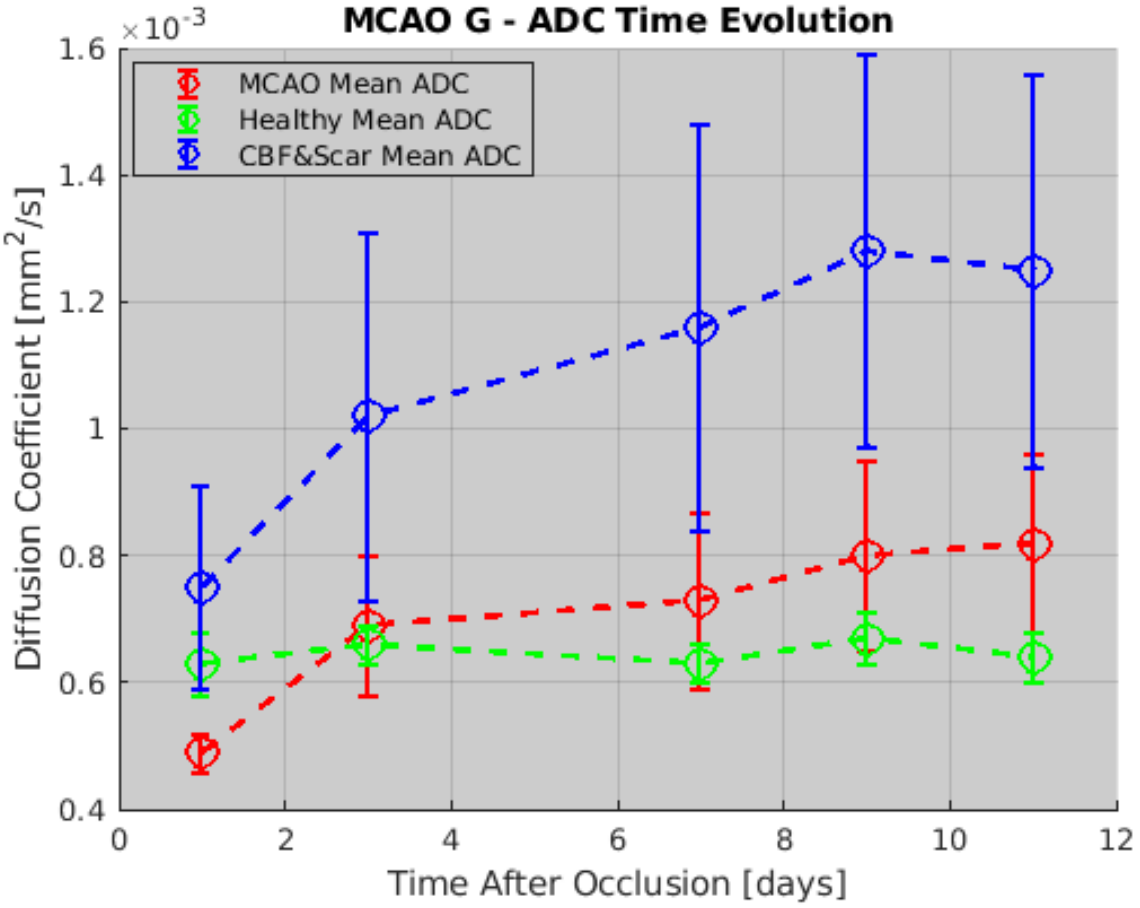

Figure 78: Mean ADC time evolution for rat MCAO G.

Based on above analysis, the mean ADC value of the ischemic stroke area increases over time after occlusion. After about 3 - 4 days, the mean ischemia ADC value increases above the ADC in healthy tissue, due to stroke scar formed in the ischemic region. It affects the third component of the GMM. The diffusion value in the stroke area is about 0.45 $*10^{-3}mm^2/s$ one

day after occlusion. After five days, ADC is about 0.72 $*10^{-3}mm^2/s$. After fifth day, the ADC increasing rate is lower. On the other hand, the ADC value in the healthy tissue doesn't change over time after occlusion and it is equal about 0.65 $*10^{-3}mm^2/s$.

The used GMM model assigns to each pixel a probability of which component it belongs to. In other words, the model assigns each pixel to the stroke area, to the healthy area or to the Cerebrospinal fluid, based on ADC values. This is an unsupervised learning aspect, because the pixel is assigned to appropriate component without human interaction. Based on that, it is possible to generate stroke and healthy mask. The Figure below presents a mask of the stroke and healthy region based on GMM overlayed on the DWI image.

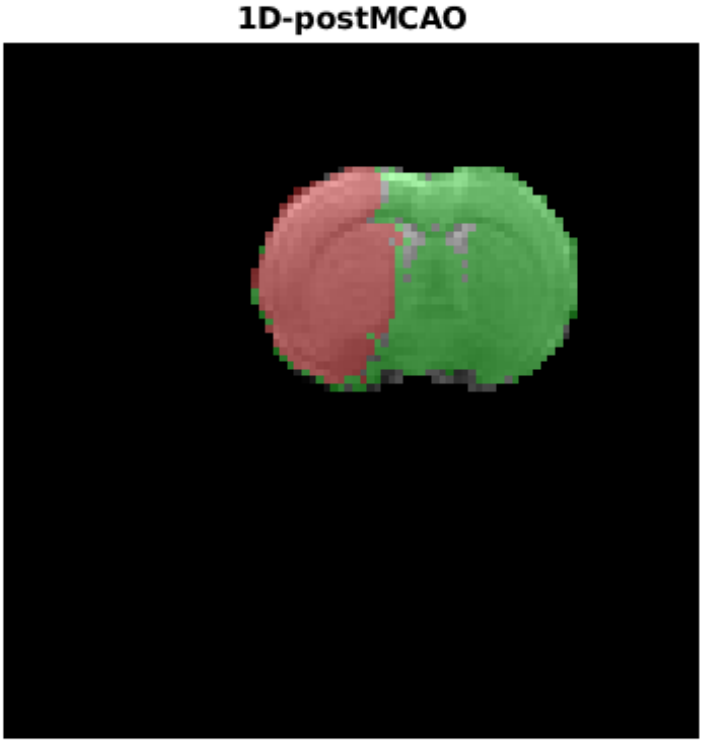

Figure 79: GMM generated stroke and healthy masks.

The best results are achieved by masking the brain 1 - 2 days after occlusion. In the later days, the stroke component begins overlap the healthy area, so it is difficult to distinguish ischemic and unaffected regions using this method. Nevertheless, this is important knowledge about GMM in ADC evolution studies. It shows that using GMM it is possible to track the ADC evolution and stroke size based only on ADC values. This will be an important research area in the future, especially in the case of delivering neuroprotective drugs to the brain and assessing the ischemia size reduction in preclinical and clinical works.

8.4 Biodistribution Studies

8.4.1 Limit of Detection

The biodistribution studies of the contrast agent in the animal model of MCAO stroke are a complex issue. The main idea is to deliver theranostic agents with a drug and contrast agent to the ischemic area in brain under the influence of the damaged BBB . However, to do that, it is worth to note what can be observed using MRI and what is the detection limit. The Figure 80 below presents a T_1 brain map before and after administration of the gadolinium-based contrast agent Magnevist^{TM} in a healthy rat.

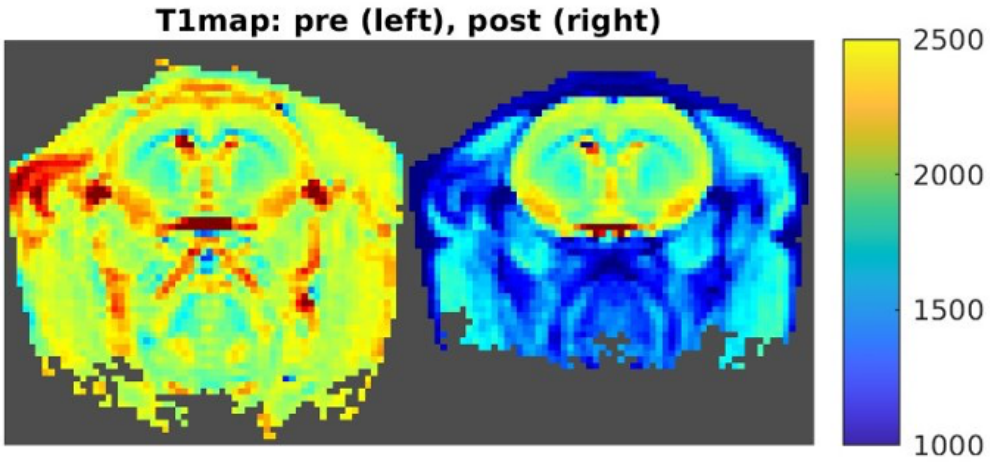

Figure 80: The T_1 map of the heatlhy rat before (on the left) and after (on the right) contrast agent (Magnevist^{TM}) administration.

The gadolinium-based contrast agent decreases relaxation times (especially T_1). The illustration above shows that the relaxation times shortened mainly in the muscles aroung the skull. However, in the brain tissue the T_1 relaxation time didn't change after contrast injection. Using the 35 equation it is possible to convert the above obtained map from T_1 relaxation times to the gadolinium concentration. On the Figure 81 below, the calculated map was presented.

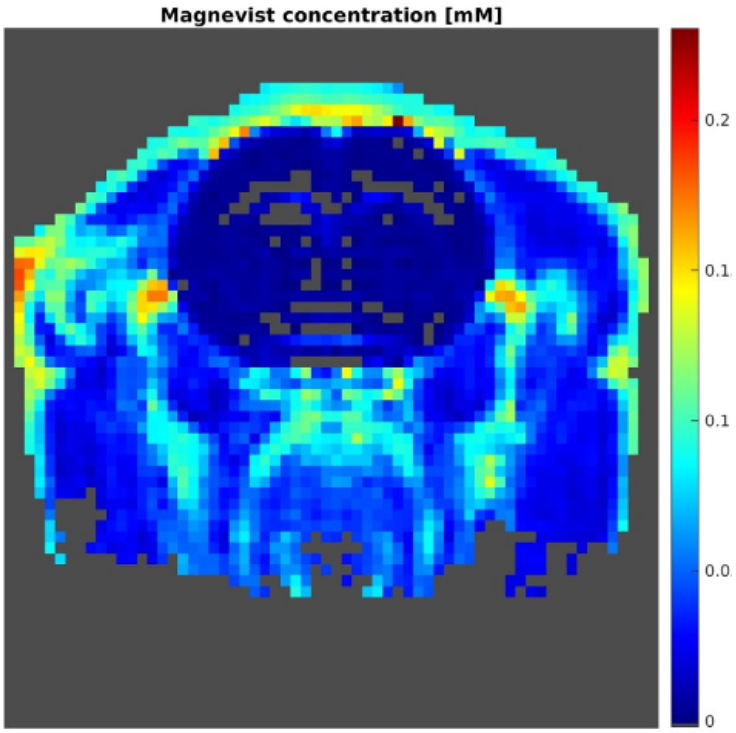

Figure 81: The gadolinium concentration in the brain after administration of Magnevist^{TM} contrast agent.

From this map, it can be seen that gadolinium was in the brain blood vessels, but didn't reach the brain tissue or reached in very small amounts, which aren't visible due to the sensitivity of the MRI method. This is reason why detection limit analysis was performed.

In the DCE biodistribution studies, the FLASH sequence was used. The signal of this sequence is dependent on sequence parameters such as the repetition time T_R and the magnetization vector flip angle FA. It is also dependent on the relaxation time T_1 and T_2^* (which can be neglected for short echo time T_E). The formula for the signal in the FLASH sequence was described in equation 64 in the previous section. Based on the previous results, the T_1 relaxation time in the stroke area was equal on average 2300 ms. After contrast agent administration and its passage through the BBB, the T_1 relaxation time in the stroke region should decrease, causing increase the signal in the FLASH sequence. The detection limit was assumed to be the concentration of gadolinium in ischemic tissue, which causes the 15% increase in the FLASH sequence signal. On the Figure 82 below, the simulation of 15% increase in signal was presented.

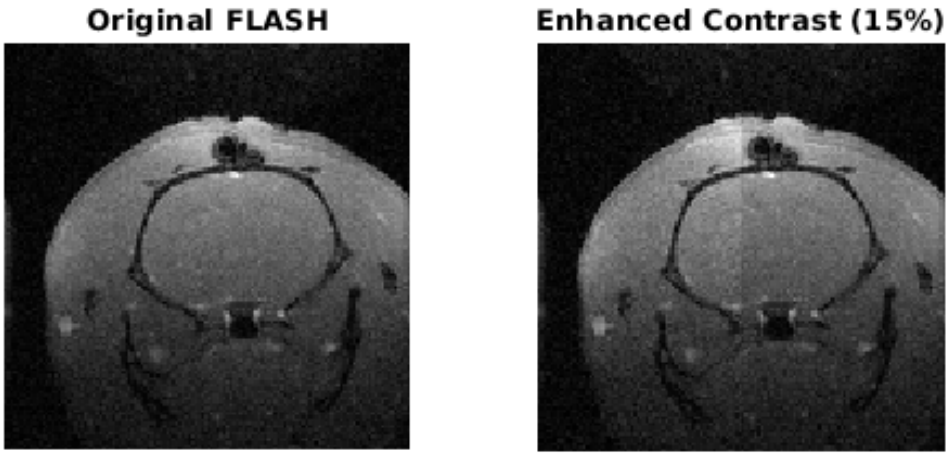

Figure 82: Simulation of 15% signal increase in FLASH MRI sequence.

In the above example, in the image labeled as "Enhanced Contrast (15%)", the area on the left side has been enhanced by 15%. This is a simulation of what is planned to be obtained. In the Figure 83 below, the dependence of the signal gain in the FLASH sequence and the gadolinium contrantration was presented.

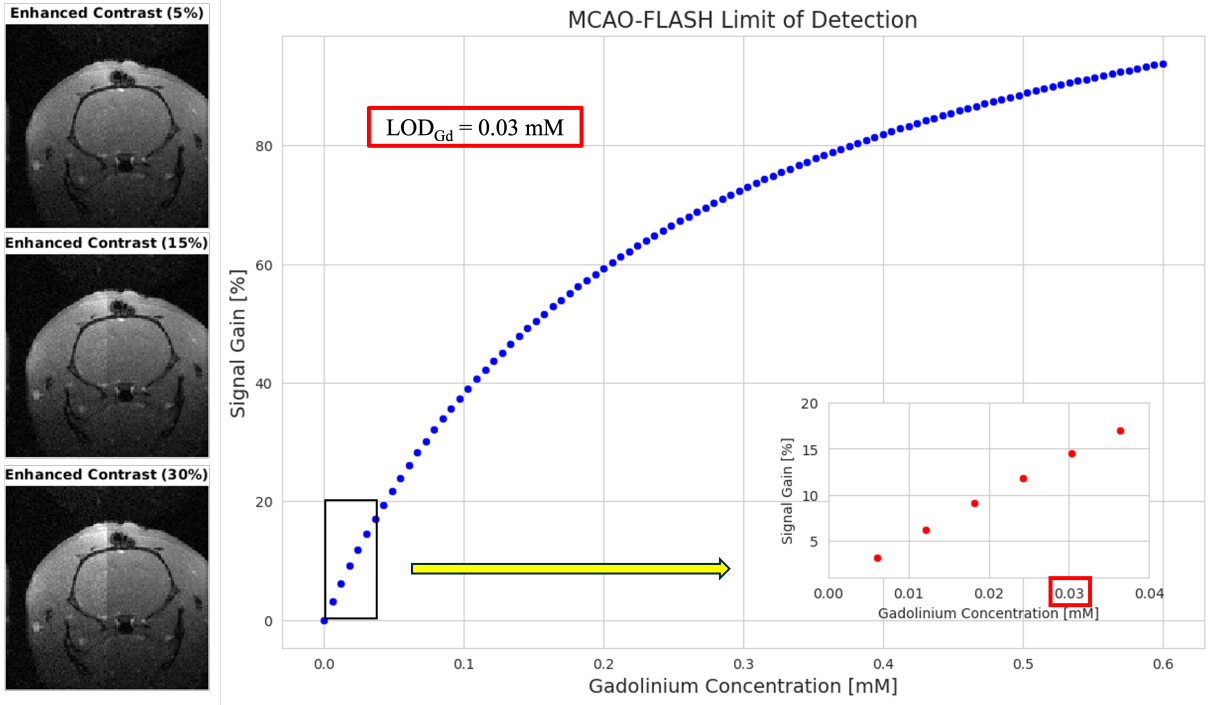

Figure 83: Dependence of FLASH signal gain on gadolinium concentration in stroke tissue.

Defining the detection limit as a 15% increate in the signal, the resulting limit of detection is a concentration of 0.03 mM gadolinium in the ischemic brain tissue. This is an important conclusion, because future potential theranostics must have a final gadolinium concentration in tissue greater or equal this value. It should be note that the contrast agent in the theranostics nanomaterial is also diluted in the blood before it reaches the stroke region.

To experimentally confirm gadolinium limit detection, the contrast agent $Gadovist^{TM}$ was used. Below is the change in the T_1-weighted image as a result of contrast agent administration.

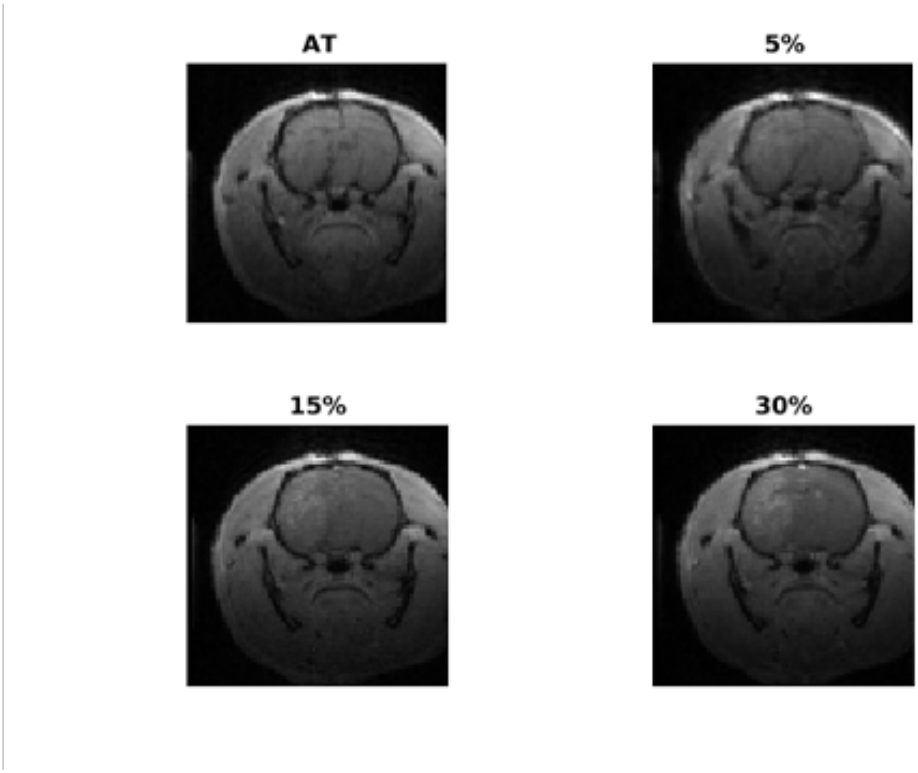

Figure 84: Signal change of T_1-weighted image, caused by contrast agent injection, third day after stroke. AT means arrival time of contrast agent. Consecutive images show 5%, 15% and 30% signal enhancement in the ischemic area caused by the influx of the gadolinium-based contrast agent $Gadovist^{TM}$.

Based on this change, it is possible to convert above image to accumulated gadolinium concentration in tissues. Below maps present a gadolinium acculumation over the experiment time.

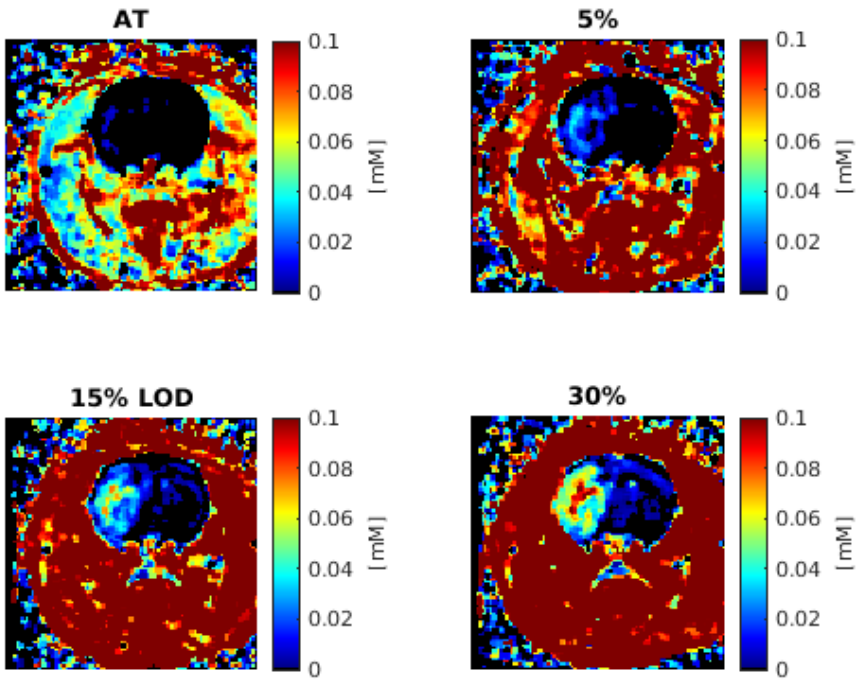

Figure 85: Gadolinium accumulation in function of signal enhancement caused by contrast agent administration in third day after stroke. AT is defined as a contrast agent arrival time and LOD is defined as gadolinium limit of detection, which corresponds to a 15% signal increase in the ischemic brain tissue.

The obtained results show that a concentration of about 0.02 - 0.05 mM corresponds to the 15% signal amplification in the impact region. This result may vary depending on the selected anatomical region, but it confirms the theoretically determined detection limit.

As already mentioned, the FLASH sequence depends on T_R, T_E, FA, T_1 and also T_2^*. For short T_E times, the dependence on T_2^* can be neglected. The selection of optimal magnetization flip angle is crucial for the signal intensity. In the FLASH sequence, the signal is maximixed at the Ernst angle, which can be calculated using this equation:

$$\alpha_E = arccos(exp(-\frac{T_R}{T_1})) \tag{72}$$

This equation is a result of calculating the derivative of the signal. For example, the analysing tissue has $T_1 = 800ms$. In this case, for $T_R = 3000ms$, the Ernst angle is equal 89^o and for $T_R = 100ms$, the angle is 28^o. Although the Ernst angle maximizes signal intensity in FLASH sequence for a specific tissue with known T_1, it doesn't maximize the contrast between two different tissues with different T_1 times. The Figure 86 below presents dependence of the FLASH signal on the flip angle for different repetition times.

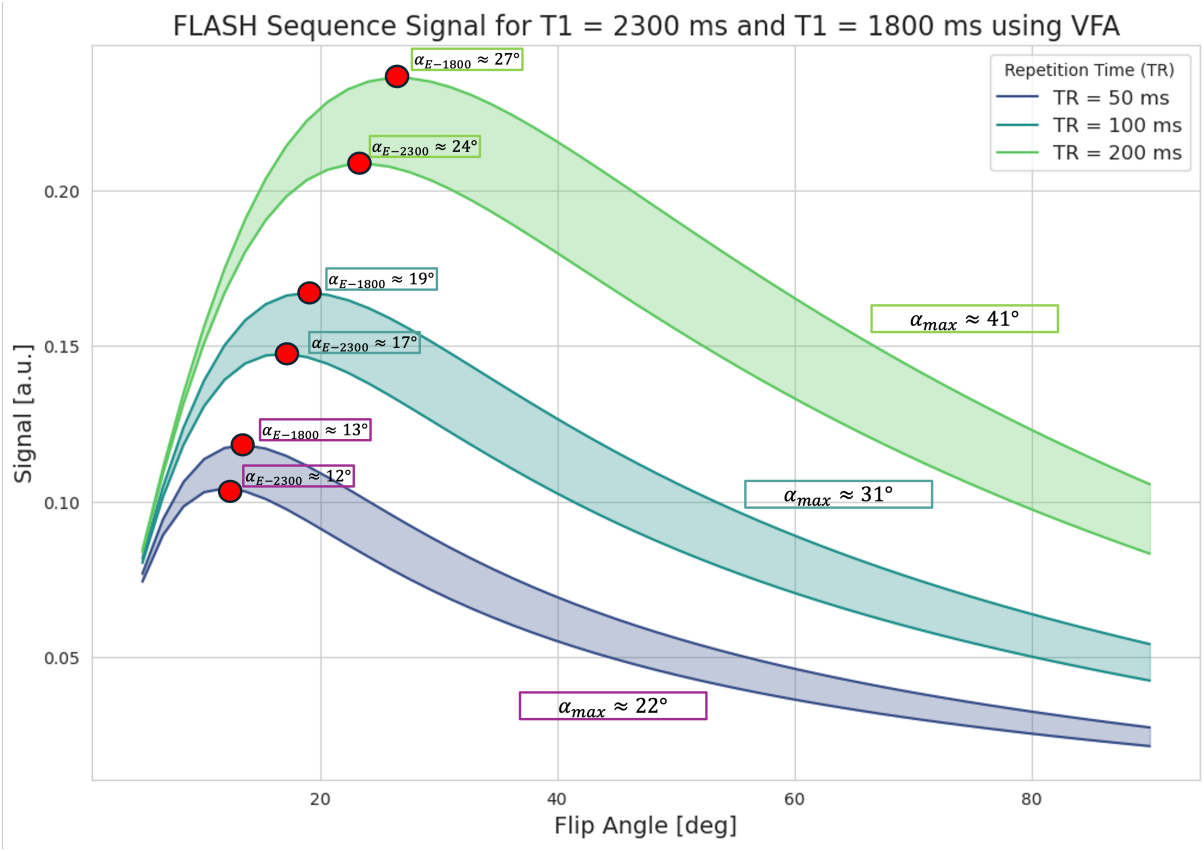

Figure 86: Dependence of FLASH signal and the flip angle with values of the highest difference and Ernst angles.

In reference to previous results, the T_1 time in the stroke area is about 2300 ms. The above figure assumes that the detection limit has been reached and that 0.03 mM gadolinium was accumulated in the ischemic region, which is equivalent to T_1 relaxation time of 1800 ms (according to formula 34). In the case of T_R equals 50 ms, the maximum image contrast is for angle 22^o, for T_R equals 100 ms, this angle was 31^o and finally for T_R equals 200 ms, the optimal flip angle is 41^o. For these angles, for given repetition times, the image contrast before and after gadolinium contrast agent administration in the stroke area is the greatest. The highest contrast always occurs for the flip angle greater then the Ernst angle. It is also worth to note that longer T_R time increases the difference of signal, but also increases the total acquisition time.

8.4.2 Blood-Brain Barrier Leaking

An extremely important aspect in the case of stroke and drug delivery to the brain is the presence of the blood-brain barrier BBB. It protects brain from harmful substances from outside. It is possible to assess the permability of the BBB using MRI imaging. For this purpose,

the animals described in the previous section with some additional animals were used, but at different measurement times after occlusion. They are presented in the Table below.

Table 30: Animal set prepared for biodistribution evolution studies.

Rat Name	**Biodistribution Days After MCAO**
MCAO D	7, 11
MCAO E	3, 7, 11
MCAO F	3, 7, 11
MCAO G	3, 7, 11
MCAO H	1, 3, 5
MCAO I	1, 5
MCAO J	3, 5

The T_1-weighted imaging using the RARE sequence with Inversion Recovery was used. This is a type of MRI sequence, which initially uses a π pulse. The time between the π inversion pulse and the $\frac{\pi}{2}$ pusle is called the inversion time T_I. Inversion recovery signal is described with this equation:

$$S_{IR} = k * [H] * (1 - 2 * exp[-\frac{T_I}{T_1}] + exp[-\frac{T_R}{T_1}]) * exp[-\frac{T_E}{T_2}] \tag{73}$$

The function of the inversion pulse is to invert the initial longitudinal magnetization of all tissues in the imaging slice, so it is in the opposite direction to the external magnetic field B_0. During the T_I interval, these tissues undergo T_1 relaxation. When signal is obtained with the $\frac{\pi}{2}$ pulse, the initial longitudinal magnetizations of different tissues are now seperated based on their different T_1 relaxation times. The rate of separation and therefore the image contrast is controlled by changing the T_I parameter. Additional contrast effects are also obtained by manipulating T_R and T_E. An example image obtained from RARE_IR sequence is shown on Figure 87 below.

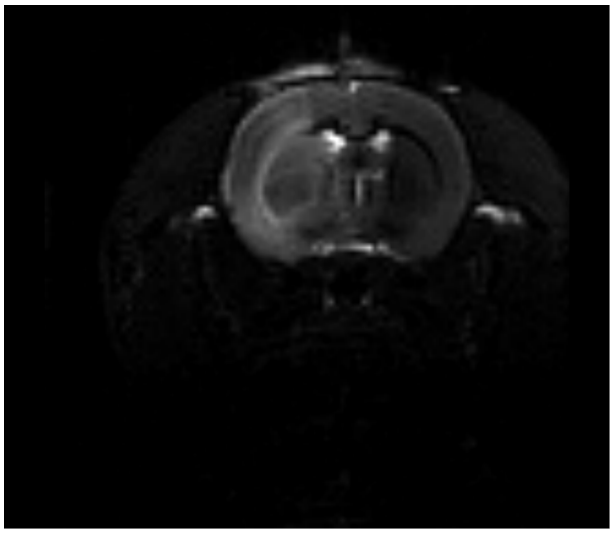

Figure 87: Image obtained through the RARE_IR sequence with inversion time T_I equals 1000 ms.

Based on the images obtained for different T_I times, it is possible to calculate T_1 value for each pixel and thus the T_1 map. An example map before and after $Gadovist^{TM}$ (200 μL + 200 μL NaCl) contrast agent administration in dose 0.6 $mmol/kg$ for different times after occlusion is presented below.

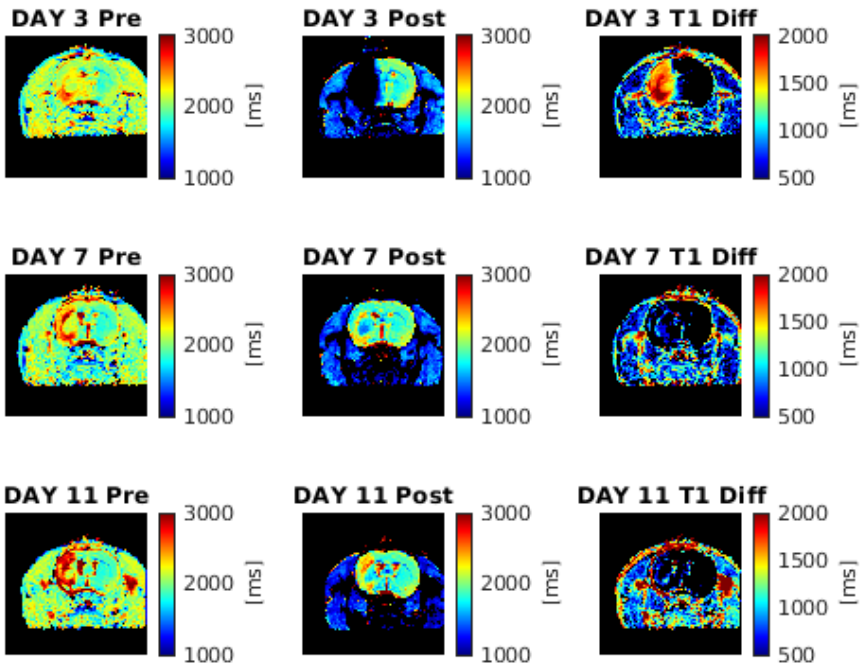

Figure 88: T_1 map of rat MCAO E brain pre and post contrast agent administration ($Gadovist^{TM}$) and their differences in T_1 times.

It can be seen that the contrast agent descreases the T_1 relaxation time in the ischemic area the most 3 days after MCAO occlusion. In the next few days, the T_1 difference aren't large, which indicated the dynamic nature of the BBB permability after ischemic stroke. Using T_1 data before and after contrast administration, it is possible to calculate the accumulation of the gadolinium in the brain. An example maps of gadolinium concentration for different times after occlusion are presented below.

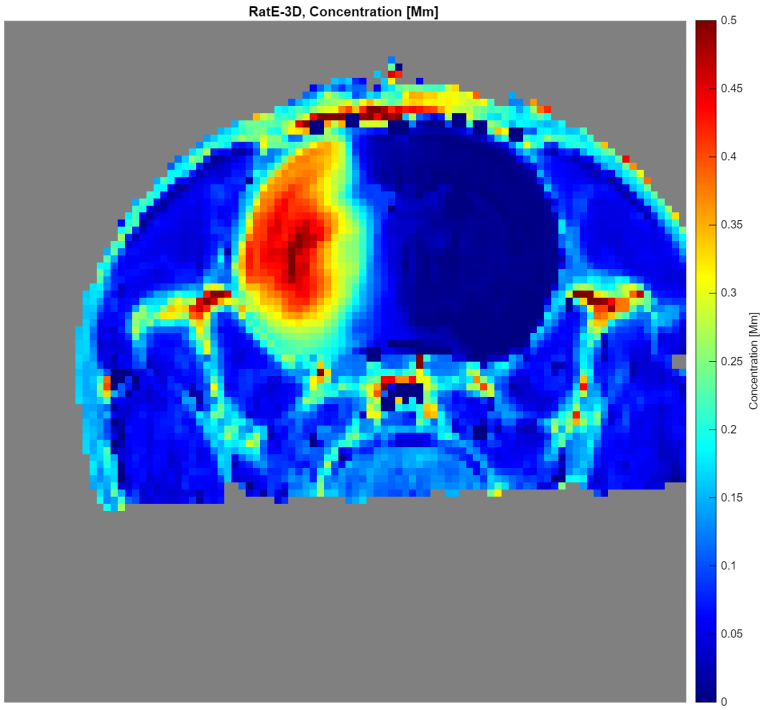

Figure 89: Gadolinium concentration map after $Gadovist^{TM}$ contrast agent administration 3 days after occlusion.

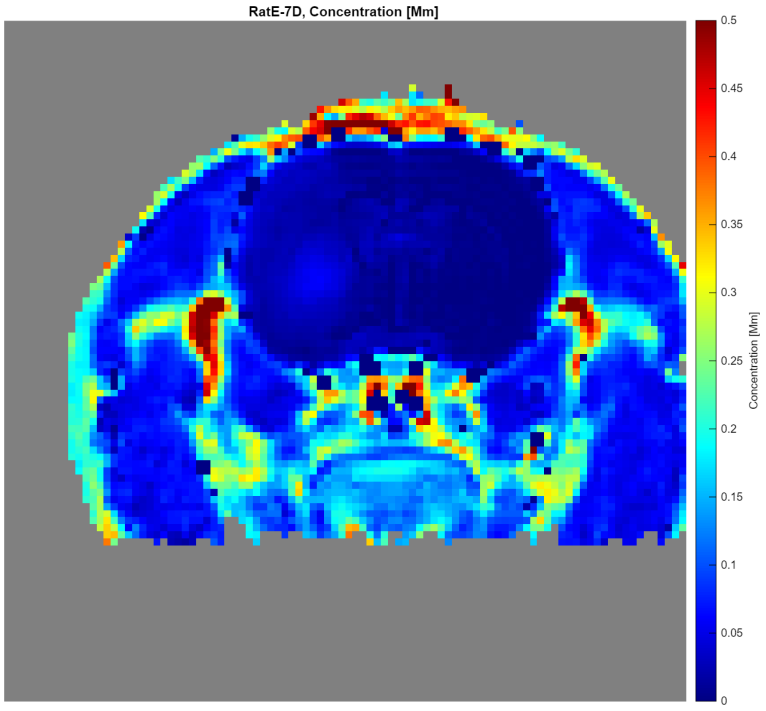

Figure 90: Gadolinium concentration map after $Gadovist^{TM}$ contrast agent administration 7 days after occlusion.

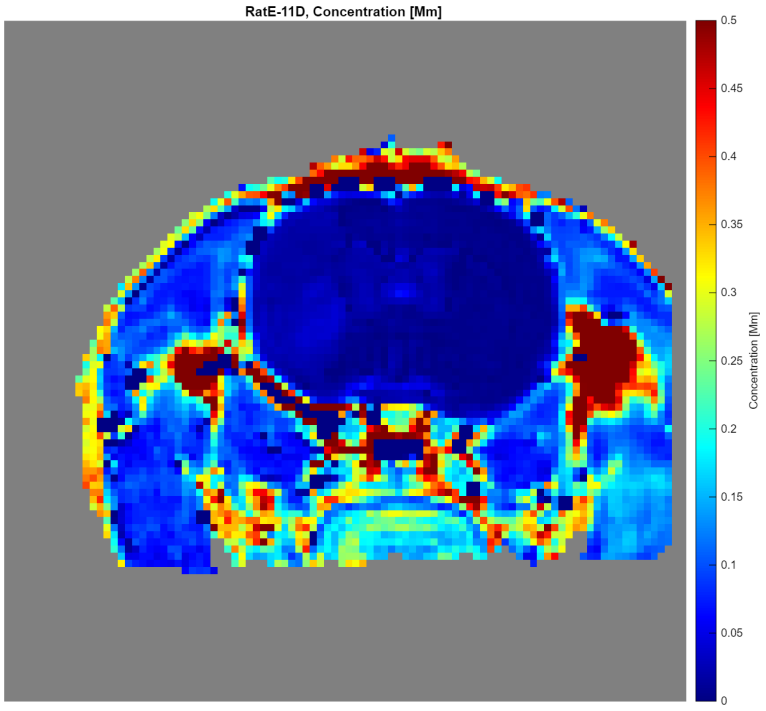

Figure 91: Gadolinium concentration map after $Gadovist^{TM}$ contrast agent administration 11 days after occlusion.

These maps confirmed that the highest amount of gadolinium accumulates in the stroke area around the third day after occlusion. After 3 days after stroke, the gadolinium concentration in

the ischemic area fluctuates aroung 0.4 mM, after 7 days after stroke this value drops to 0.15 mM and after 11 days it was already aroung 0.07 mM.

Biodistribution analysis can be also performed using DCE-FLASH imaging. The measurements consisted of obtaining T_1-weighted images in a short time interval, in this case in period of 20 minutes, during which the $Gadovist^{TM}$ contrast agent was administered to the rat's bloodstream. It caused enhancement in the image, where it accumulated. Based on the analysis of the detection limit, the optimal FLASH sequence parameters were T_R=0.05 ms and FA = 22 degrees. An example of a T_1-weighted image obtained via FLASH sequence for different timepoints and the same slice was presented below.

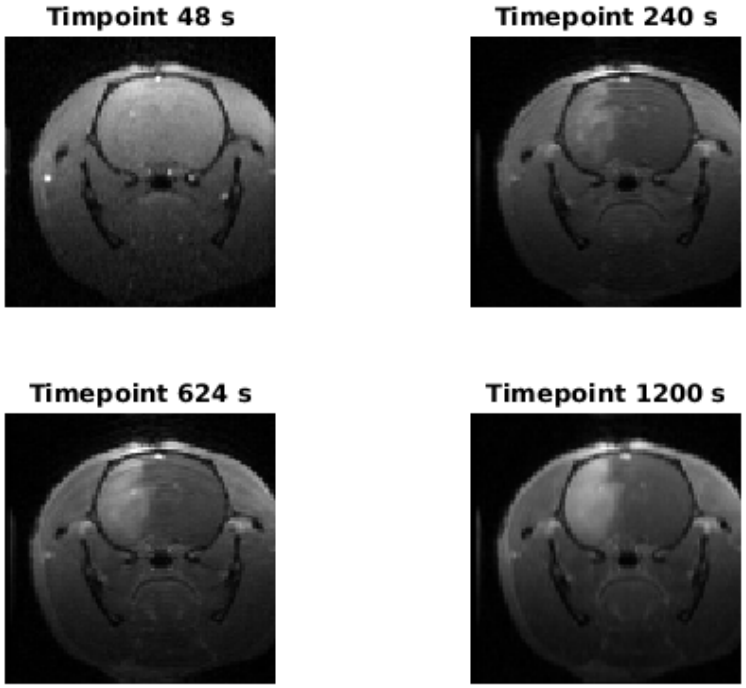

Figure 92: T_1-weighted images obtained via FLASH sequence for different time after $Gadovist^{TM}$ contrast administration, three days after MCAO.

It can be seen, the stroke region becomes brighter with time after contrast agent administration. This suggests that the BBB is leaky, which is consistent with theory. Now, it is possible to determine the pharmacokinetic curves of DCE. For this purpose, all FLASH images were registred to the first image in each slice. This operation removes the effects of possible animal movements. An example of obtained raw DCE curves of the FLASH signal in time is presented below.

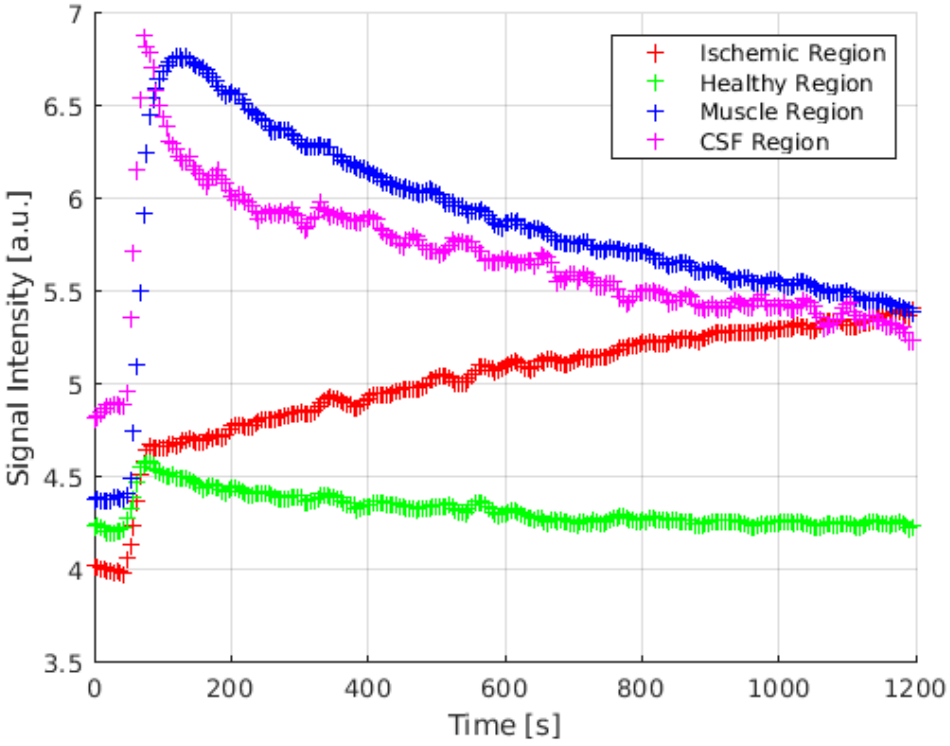

Figure 93: Dependence of raw FLASH signal in function of measurement time for third day after stroke.

This figure presents the obtained signal enhancement curves due to the $Gadovist^{TM}$ contrast agent administration for four areas: ischemic area, healthy area, cerebrospinal fluid area and muscles. These curves can be converted to a gadolinium concentration in function of time. For this purpose, the following equations were used:

$$R_1(t) = -\frac{1}{T_R} ln(\frac{1-(A(t)+B)}{1-cos(FA)(A(t)+B)}) \tag{74}$$

$$A(t) = \frac{S(t)-S(0)}{M_0 sin(FA)} \tag{75}$$

$$B = \frac{1-e^{-T_R/T_{10}}}{1-cos(FA)e^{-T_R/T_{10}}} \tag{76}$$

$$C(t) = \frac{1}{r_1}(R_1(t)-R_{10}) \tag{77}$$

where: M_0 is equilibrium magnetization, S is steady state signal and T_{10} is the pre-contrast longitudinal relaxation time [111]. Converting the raw signal to gadolinium concentration is crucial and necessary for quantitative analysis. An example of converted data showing dependence of gadolinium concentration in time with FLASH image in different timepoints after stroke are presented below.

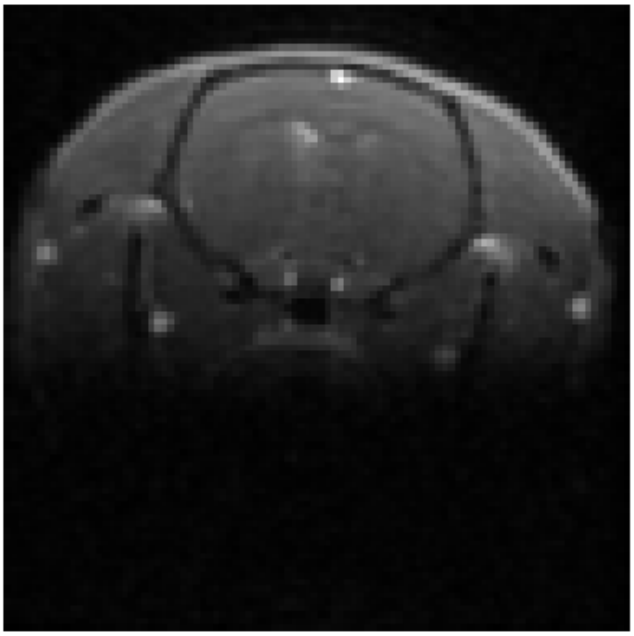

Figure 94: The FLASH image obtained 1 day after stroke.

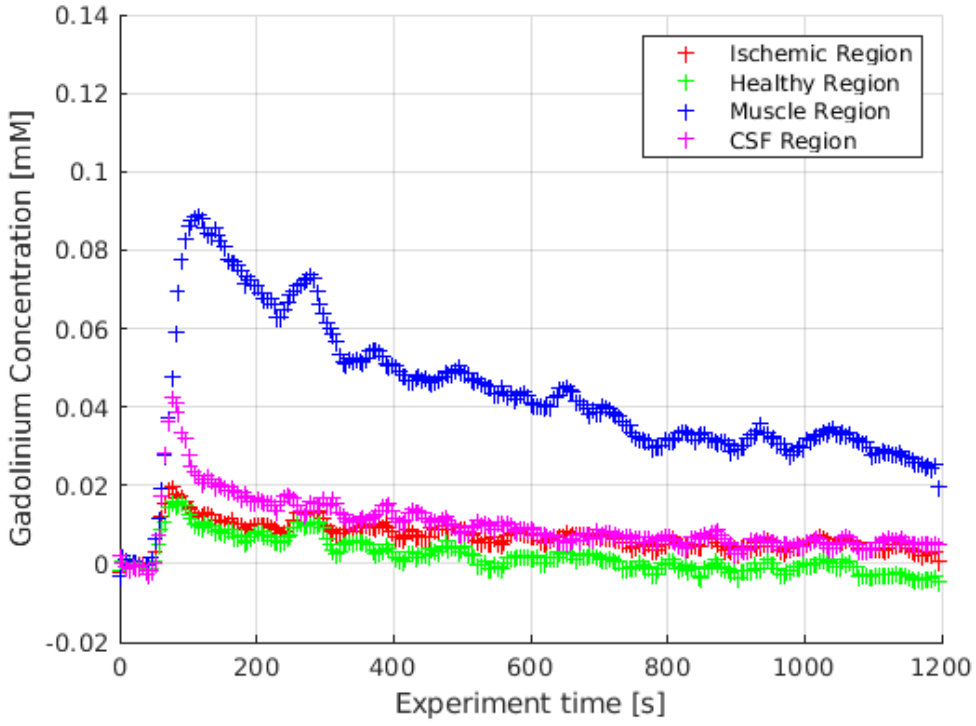

Figure 95: Gadolinium accumulation 1 day after stroke.

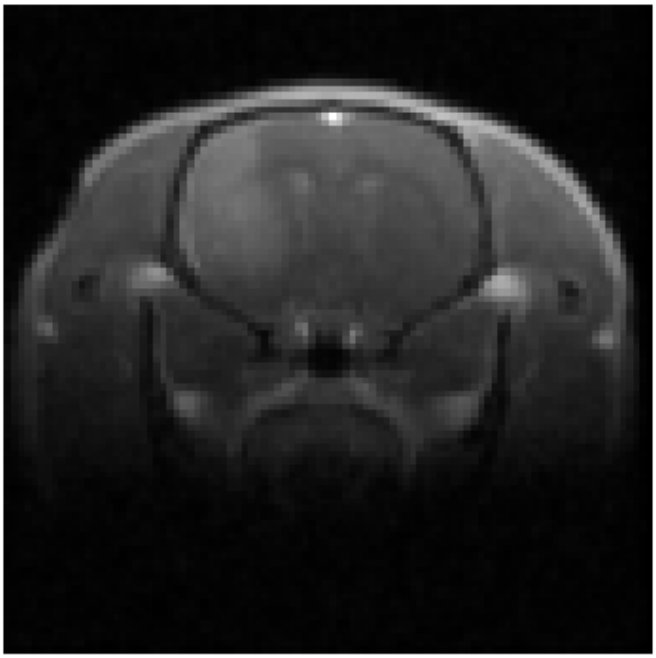

Figure 96: The FLASH image obtained 3 day after stroke.

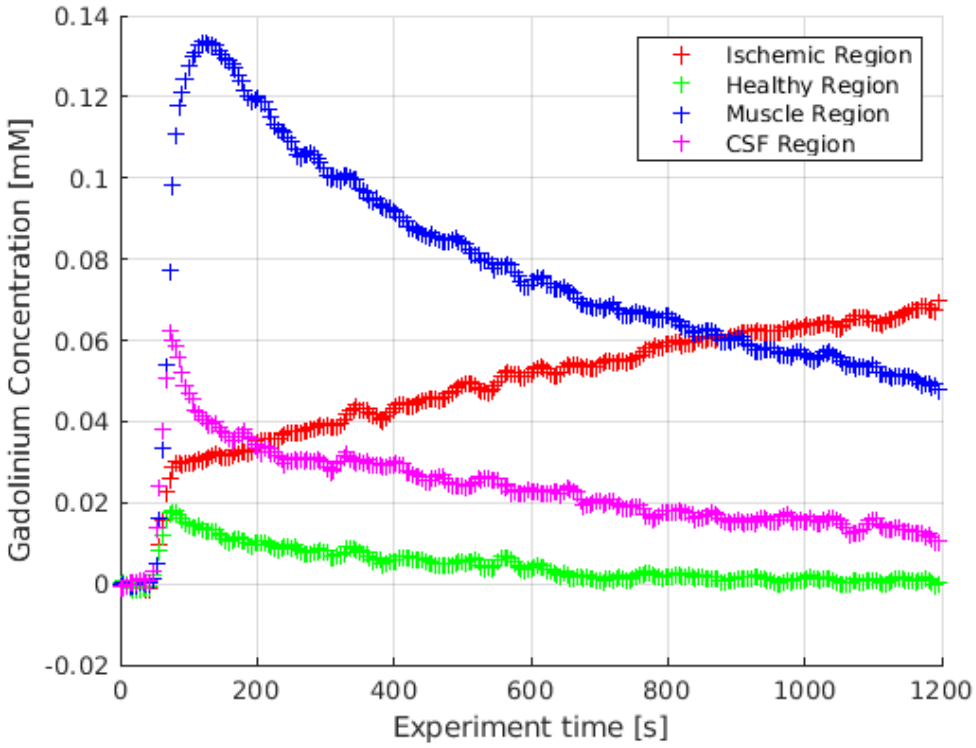

Figure 97: Gadolinium accumulation 3 day after stroke.

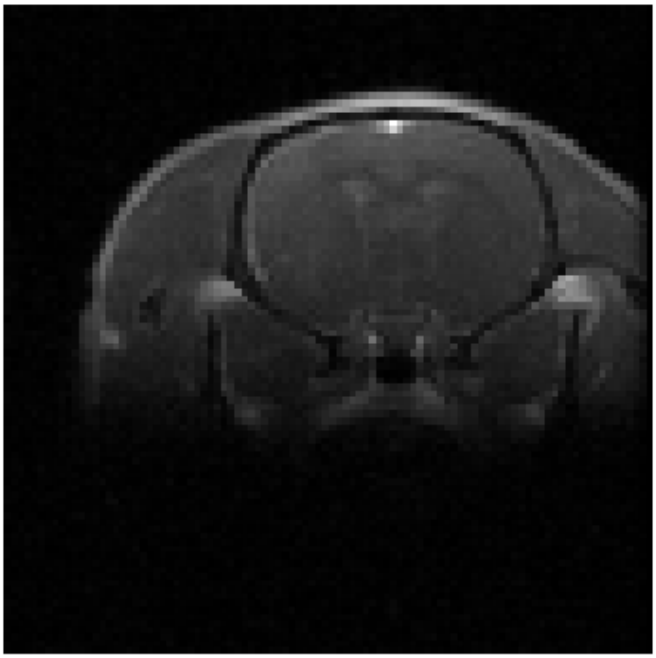

Figure 98: The FLASH image obtained 5 day after stroke.

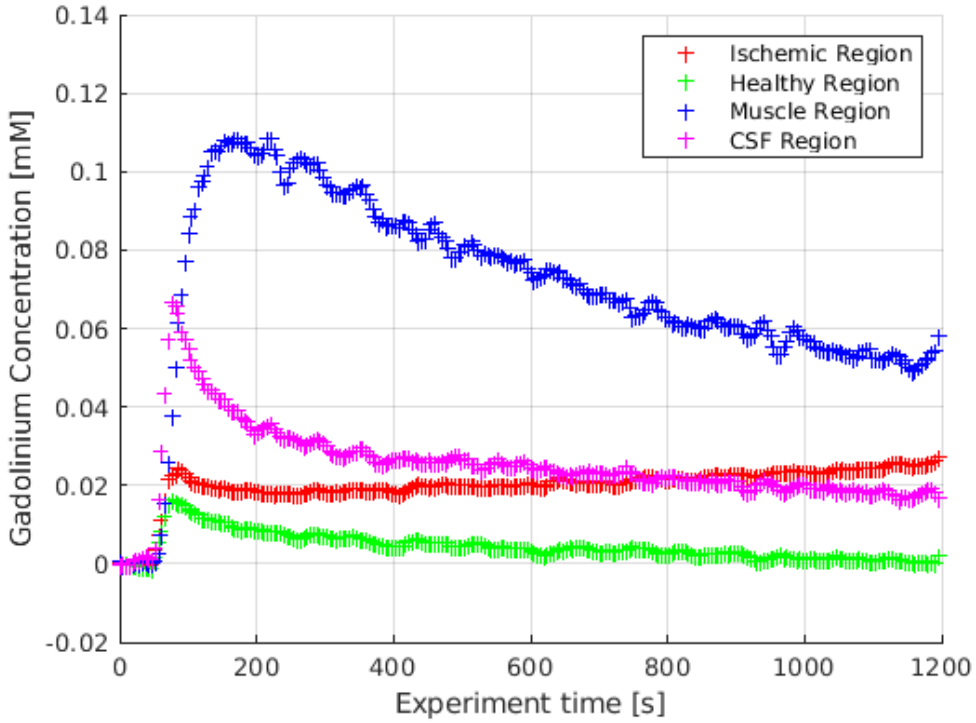

Figure 99: Gadolinium accumulation 5 day after stroke.

Additionally, to analyze biokinetic parameters, additional imaging was performed on a slice passing through neck. From this slice, the Region of Interest was selected defining the carotid artery from which the Arterial Input Function AIF was determined. The AIF is the concentration of tracer in blood-plasma in brain artery measured over time. The obtained AIF curve was presented below.

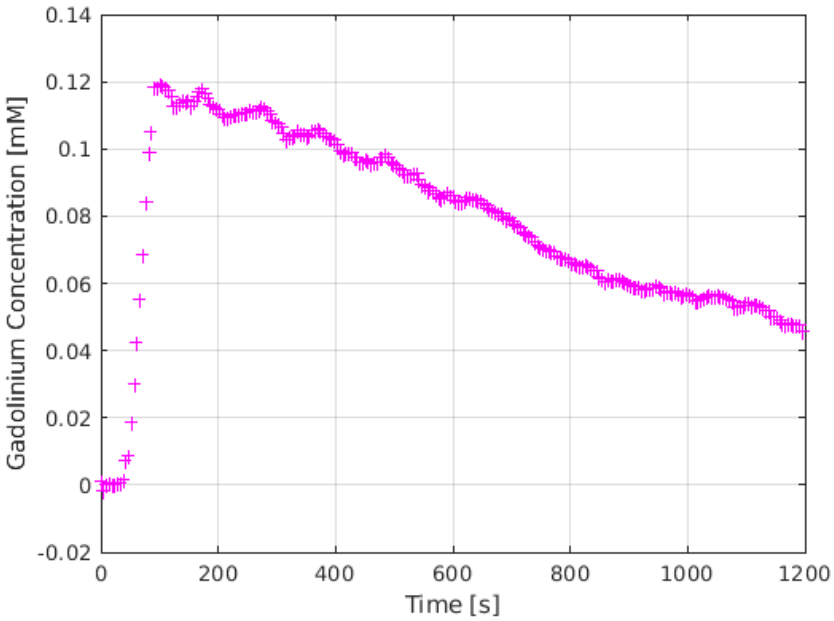

Figure 100: Gadolinium concentration of AIF.

From this figure, it can be seen that the gadolinium concentration in the blood is about 0.12 mM. Using the above conversion, the gadolinium maps in the brain and brain with muscles were calculated over the entire FLASH protocol. These maps are presented below.

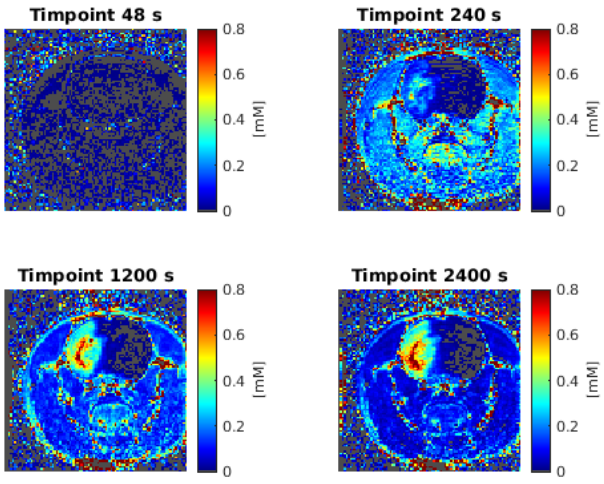

Figure 101: Gadolinium concentration maps in different timepoints, three days after MCAO. Cross-section through the head of a rat.

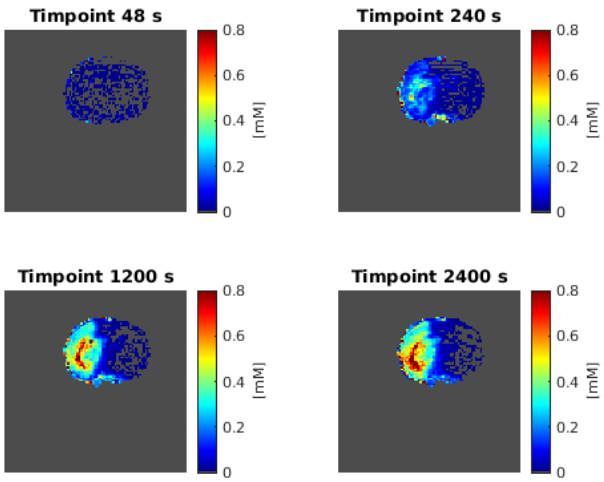

Figure 102: Brain gadolinium concentration maps in different timepoints, three days after MCAO. Section through the rat brain.

As can be seen, in this case of three days after occlusion, the contrast is mainly leaked into the stroke area. In the ischemic brain tissue, about 0.4 mM of gadolinium was accumulated, while in the muscle about 0.2 mM was accumulated. In healthy tissue, the gadolinium concentration is unnoticeable, at least based on MRI imaging, due to the detection limit. For the above DCE curves, the imaging was performed in time interval betwenn 1 and 5 days after stroke episode. The ishcemic region, healthy region, CSF region and muscle region were analyzed. In the healthy tissue, the contrast agent doesn't cross the BBB for each measurement timepoint, caused by integrity of the BBB. For the CSF region, the BBB is permeable for each time point,

due to the physiology of the barrier in this case. In the muscle region, where there isn't BBB, the contrast agent hasn't problem crossing the endothelium, hence the significantly higher concentrations in the muscle region. The contrast agent crosses the endothelium by simple diffusion. For the stroke region, it appears that at day 1 after stroke, the barrier is only slightly leaky, as indicated by the low concentrations in the DCE graphs. On the other hand, 3 days after the stroke, the maximum BBB permeability occurs in the ischemic area, which indicates that the future theranostic can cross the barrier and reach the brain tissue at this time point. At a later timepoint - 5 days after the stroke, the barrier permeability decreases again. These studies were performed at a Gadovist dose of 0.1 mmol/kg.

For pharmacokinetic modeling and determination of the K^{trans} coefficient, a rat was used with a time interval of 3, 7, and 11 after a stroke with a $Gadovist^{TM}$ dose of 0.6 mmol/kg. In this case, due to the high dose and the presence of a bolus, two effects occur simultaneously: the T_1 effect (DCE) and the T_2^* effect (DSC), hence the determined K^{trans} is apparent. Firstly, the DSC effect dominates, but later the T_1 DCE effect begins to dominate. Based on that and obtained gadolinium concentration and AIF, it is possible to calculate the transfer constant K^{trans} using the Tofts pharmacokinetic model. The parameter was estimated pixel-by-pixel using the least squares method. Below are examples of K^{trans} maps for the same rat and different timepoints after ischemic episode.

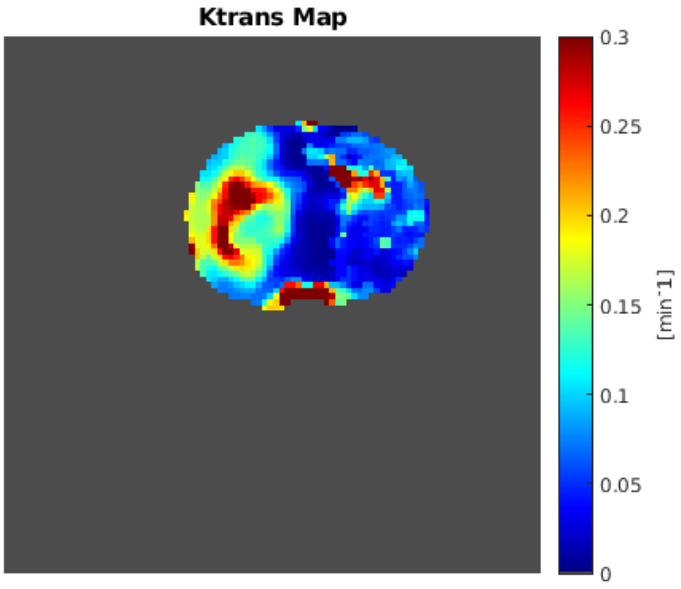

Figure 103: The K^{trans} map three days after occlusion. The area with the highest K^{trans} values coincides with the area of ischemia suggesting that the BBB is permeable at this time point.

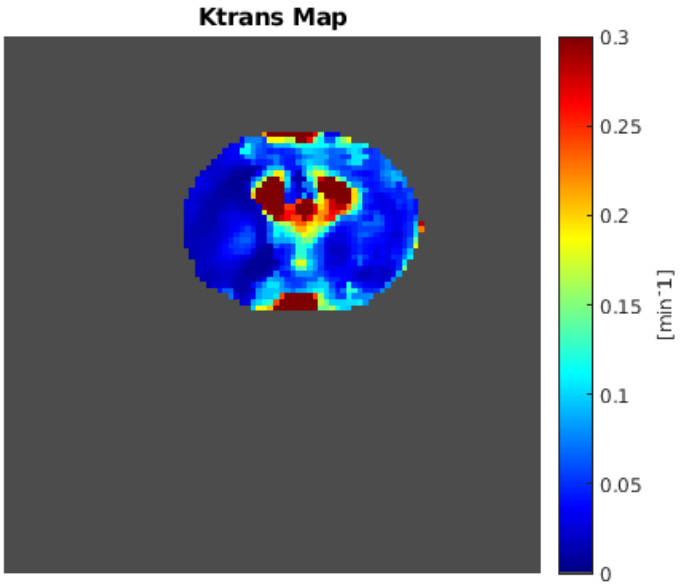

Figure 104: The K^{trans} map seven days after occlusion.

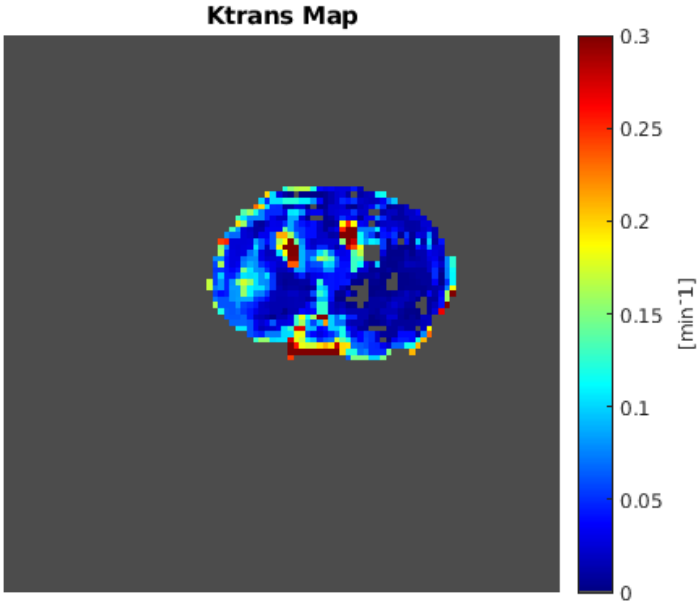

Figure 105: The K^{trans} map eleven days after occlusion.

Based on these maps, it turns out that the BBB has the highest permeability on day 3, and then the permeability decreases. In the case of the 3-day post-stroke time interval, the penumbral area is visible. In the case of seven-day time interval, tke K^{trans} permability was already lower. In the case of eleven days, K^{trans} was even lower. Conveniently, the stroke nucleus had the greatest changes in K^{trans} values, because it dropped from 0.3 min^{-1} to 0.05 min^{-1}

and later to the noise limit. The obtained results are confirmed for each tested animal. It is also worth remembering that the K^{trans} measurement was apparent, due to the presence of the second DSC effect, however after precise fitting of the Tofts curves to the data, the obtained results give some insight into how the BBB permeability changes over time. This experiment also allowed for writing special software, which uses the data processing pipeline and calculates apparent K^{trans}.

9 Discussion

The experimental part of this thesis is divided into two areas. The first one is *in vitro* analysis of the contrasting properties of potential theranostic nanomaterials, aimed as a carriers for neuroprotective drugs. The second area concern characterisation of *in vivo* animal model of experimental stroke (MCAO) in order to establish baseline data for potential application of the developed most promising theranostic agents.

In the first stage, different new potential theranostic nanocarriers with a gadolinium-based contrast agent in chemical structure were studied via *in vitro* methodology. Among these, several types of nanoparticles can be distinguished like AOT/PLL and PCL nanocapsules with one and two gadolinium layers on their shells; nanoparticles based on quantum dots labeled with gadolinium; nanoparticles based on the new theranotic approach POSS [95] and nanoparticles based on cerium oxide. The aim of this analysis was the evaluation of the contrast properties of these nanomaterials using MRI for future *in vivo* biodistribution studies.

In the first step, the AOT/PLL and PCL nanocapsules were studied. The idea of using nanocapsules is as follows: a drug with neuroprotective properties is placed in the core of the nanocapsule, while layers located on the outside are containing gadolinium. Therefore, there is a dual theranostic functionality - diagnostic and therapeutic. These nanocapsules were synthetized using the layer-by-layer method, which consists in successive addition layers with opposite charges. Tha aim was to evaluate contrasting properties of nanoparticles with one gadolinium layer on the shell (layers sequence: PLL/PGA/PLL-Gd/PGA-g-PEG) and with two gadolinium layers (layers sequence: PLL/PGA/PLL-Gd/PGA/PLL-Gd/PGA-g-PEG). The initial gadolinium concentration for nanocapsules with one gadolinium layer were 55 μM, while for nanocapsules with two gadolinium layers was 120 μM. Nanocapsule solutions were successively diluted to prepare a set of samples with different concentrations for contrast properties studies. The T_1-weighted and T_2-weighted imaging was performed on the prepared set of samples with T_1 and T_2 mapping. This allowed to obtain T_1 and T_2 relaxation times for each sample. These values were converted to the relaxation rates R_1 and R_2, which allowed to draw a graph of dependence of R_1/R_2 on the gadolinium concentration. From this graph, the molar relaxivities r_1 and r_2 were determined, which describe the effect on longitudinal and transverse relaxation, respectively. Due to the fact that the structure of the nanoparticles contains a positive contrast agent - gadolinium, during the analysis a great attention was paid to determining the molar relaxivity r_1. The molar relaxivities r_1 for nanocapsules were: 3.71 $\pm$ 0.05 $mM^{-1}s^{-1}$ for AOT/PLL 1xGd, 3.65 $\pm$ 0.18 $mM^{-1}s^{-1}$ for PCL 1xGd, 2.53 $\pm$ 0.03 $mM^{-1}s^{-1}$ for AOT/PLL

2xGd and 3.28 ± 0.03 $mM^{-1}s^{-1}$ for PCL 2xGd. In turn, the molar relaxivities r_2 were 11.88 ± 1.33 $mM^{-1}s^{-1}$ for AOT/PLL 1xGd, 22.79 ± 1.84 $mM^{-1}s^{-1}$ for PCL 1xGd, 15.49 ± 0.47 $mM^{-1}s^{-1}$ for AOT/PLL 2xGd and 16.81 ± 0.28 $mM^{-1}s^{-1}$ for PCL 2xGd. The obtained results showed that nanocapsules based on AOT/PLL and PCL exhibit reasonable contrast properties, comparable to those of commercially available contrast agents [45]. Addition of the second Gd layer significantly increases contrasting effects per nanocapsule concentration, however, they are slightly decreased when calculated per Gd concentration. Thus, nanocapsules with one gadolinium layer have slightly higher r_1 value than nanopartile with two gadolinium layers, which results from the fact that Gd complexes are slightly less available to interaction with water molecules in case of double layer geometry. Moreover, during the synthesis of nanocapsules with an extra gadolinium layer, the total nanocapsules concentration decreases in the resulted Gd-doped nanocapsules solution. This effect reduces contrasting properties of the resulting solution, unless it will undergo further concentration. It is also important to balance increase of the contrasting properties per nanocapsule concentration (which is higer for two-layer geometry) allowing to use lower nanocapsule concentrtion for the same contrasting effect , with drug load which is directly proportional to the nanocapsule concentration. Thus balancing necessary drug concentration with contrasting effects should lead to the choice of the most reasonable solution. Therefore, for the future *in vivo* studies, it is recommended to focus on the usage nanocapsules AOT/PLL and PCL with one gadolinium layer for maximizing drug delivery, while two-gadolinium layer (with subsequent increase of NCs concentration) for MRI biodistribution studies.

The second stage focused on the evaluation of contrast properties of quantum dots nanoparticles labelled with gadolinium CQD-Gd. In this case, the initial gadolinium concentration was 41 mM. These samples were also subjected to dilution, followed by T_1- and T_2-weighted imaging and mapping of these values. The obtained molar relaxivity r_1 was equaled 0.09 ± 0.0004 $mM^{-1}s^{-1}$ for CQD-Gd and the molar relaxivity r_2 was 0.13 ± 0.0003 $mM^{-1}s^{-1}$ for CQD-Gd. These results showed that CQD-Gd nanoparticles labelled with gadolinium doesn't have good contrast properties for MRI imaging, due to the low r_1 and r_2 values. It was therefore rejected as a potential theranostic nanoparticles for MRI imaging.

The next type of tested nanoparticles were POSS-based nanoparticles. Among them, the following modifications can be distinguished: Lactamide POSS-Gd, POSS-Gd in water, POSS-Gd in PBS solution and POSS without gadolinium labeling. Modifications of the chemical structure of POSS were intended to improve biodistribution. The initial concentrations of gadolinium were

2.98 mM for samples of Lactamide POSS-Gd, POSS-Gd in water and POSS-Gd in PBS. In turn, the nanoparticle concentration of POSS without gadolinium was 23.85 mM. The initial concentrations were successively diluted for samples, which were subjected to T_1- and T_2-weighted imaging and mapping. According to the theory in T_1-weighted images, a higher gadolinium concentration in the samples caused a brighter area on the image, due to higher signal value (Fig. 49). In turn, in T_2-weighted images, a darker area corresponded to a higher gadolinium concentration, due to a lower signal value. This is also in line with the theory, because this analysis was based on nanoparticles with a positive contrast properties. Also, the obtained T_1 and T_2 relaxation curves showed that the more gadolinium in solution, the faster increasement in longitudinal magnetization or decreasement in transverse magnetization. Based on the obtained T_1 and T_2 relaxation times and their R_1 and R_2 relaxation rates, the molar relaxivities r_1 and r_2 were determined. The obtained molar relaxivities r_1 were: 2.48 $\pm$ 0.03 $mM^{-1}s^{-1}$ for Lactamide POSS-Gd, 1.89 $\pm$ 0.01 $mM^{-1}s^{-1}$ POSS-Gd in water, 2.11 $\pm$ 0.01 $mM^{-1}s^{-1}$ for POSS-Gd in PBS and 0.001 $\pm$ 0.0002 $mM^{-1}s^{-1}$ for POSS without gadolinium labeling, respectively. The molar relaxivities r_2 were 8.43 $\pm$ 0.06 $mM^{-1}s^{-1}$ for Lactamide POSS-Gd, 6.82 $\pm$ 0.21 $mM^{-1}s^{-1}$ for POSS-Gd in water and 91.06 $\pm$ 3.76 $mM^{-1}s^{-1}$ for POSS-Gd in PBS. Due to the low r_1 value for POSS without gadolinium labeling, the contrast properties in terms of T_2 relaxation were not calculated. The obtained results suggest that POSS-based nanoparticles exhibit reasonable contrast properties, described by molar relaxivities r_1 comparable to commercially available contrasts. Additionally, it was confirmed that the source of the contrast properties in POSS-based nanoparticles is the presence of gadolinium in the chemical structure. The key factor is location of gadolinium in structure, whether it is inside the molecule or outside. The result, which is different from others is result of r_2 for POSS-Gd in PBS nanoparticles. This result is caused by the fact, that PBS macromolecules cause T_2 relaxation themselves. The use of PBS was aimed at stabilizing nanoparticles.

The last type of studied nanoparticles were cerium oxide. Cerium oxide has a neuroprotective properties itself, so it is a natural that it can be treated as a potential theranostic [97]. The following types of cerium oxide nanoparticles can be distinguished: cerium oxide labeled with gadolinium CeO2-Gd and cerium oxide without gadolinium labeling CeO2. Due to the tests on cell lines, the nanoparticles were filtred through a 450 nm filter. The initial concentration of gadolinium in CeO2-Gd was 4.34 mM, while the nanoparticles concentration in CeO2 solution was 3.78 mM. The obtained molar relaxivities r_1 were 34.03 $\pm$ 0.48 $mM^{-1}s^{-1}$ for CeO2-Gd and 0.75 $\pm$ 0.02 $mM^{-1}s^{-1}$ for CeO2. In turn, the molar relaxivities r_2 were 74.61 $\pm$ 1.12 $mM^{-1}s^{-1}$

for CeO2-Gd and 1.11 ± 0.04 $mM^{-1}s^{-1}$ for CeO2. These results indicate that the source of contrast properties is the presence of gadolinium in the cage structure. The molar relaxivities values for ceria nanoparticles are very high, which suggests that this nanoparticles have excellent contrast properties for MRI imaging purposes, which was aslo shown in the obtained T_1- and T_2-weighted images (Fig. 55). However, another problem arose for the cerium oxide nanoparticles. It turned out that these nanoparticles quickly agglomerate, forming a kind of jelly. After just a few hours after filtration and sonification of the nanoparticles, it was observed that a jelly forms in the test sample, which prevents the usage of these nanoparticles for theranostic *in vivo* purposes, even after several times dilution of the original solution. For this reason, the polyacrylic acid PAA was added to the cerium oxide structure CeO2-Gd, creating the compound CeO2-Gd-PAA. Adding PAA to the structure should improve the biodistribution of the nanoparticles and reduce agglomeration. That was observed. These nanoparticles were subjected to the same imaging protocol, which allowed determining the molar relativity r1, which was 1.33 ± 0.02 $mM^{-1}s^{-1}$ for CeO2-Gd-PAA. The addition of PAA was found to reduce nanoparticle agglomeration, but at the expense of MRI contrast properties.

That was the first step of research for the purposes of the doctoral dissertation. The main aim was *in vitro* measurements of different nanoparticles in terms of MRI contrast properties and their comparison with commercially available contrast agents. Great attention was paid to the synthesis of new nanoparticles as a potential theranostics. This is a key stage, because nanoparticles will be tested preclinically *in vivo* in animal and it is necessary to have appropriate contrast properties to be able to see them and study their biodistribution in the body, first with the contrast agent and ultimately with the therapeutic drug. In future, is is worth paying attention to nanocapsules based on AOT/PLL and PCL with one gadolinium layer on the shell, Lactamide POSS-Gd nanoparticles and CeO2-Gd-PAA.

The second step of experimental part of dissertation focused on the results on *in vivo* studies using an animal rat model of ischemic stroke MCAO. This model is based on blocking the middle cerebral artery with a special filament, causing ischemic changes. Afer 90 minutes, this filamet was removed from artery, leading to reperfusion. The induction of MCAO model took place at the Faculty of Pharmacy Jagiellonian University Medical College, at least 24 hours before the first imaging, which had place in the Department of Magnetic Resonance Imaging in Institute of Nuclear Physics PAS. This time of 24 hours was strongly important, because it allowed animals to acclimatize in new place. These studies focused on two sets of animals and on characterizing the MCAO model, establishing an imaging protocol for biodistribution stud-

ies, optimizing used sequences and establishing the limit of detection of gadolinium in ischemic tissue using MRI methodology.

During the MRI image analysis, it is important to extract the brain region for its analysis of various parameters in the brain. Usually, the brain was extracted manually using a own scipt in MATLAB, due to clear UI. However, considering the fact that the image has many slices and multi-dimensional shapes, the process of skull stripping of these images becomes very time-consuming. Reults of this manual extraction depends on the operator's skills and experiance, what is also to note. Therefore, the RS^2-Net neural network model was tested to extract the stroke brain. Image preprocessing consisted of reshaping the image to the appropriate format, its normalization and conversion to $.nifti$ format. This was done using own script in MATLAB and Python via VS Code. Using the NVIDIA GeForce RTX 4070 graphics card and Python, a binary mask of the brain region was created by neural network, which was applied to the original image, before it was fed to deep neural network. To evaluate the brain extraction, the Dice coefficient was used, which is a metric used in the segmentation processes. Based on obtained results, it can be seen that for all rats (MCAO 0-8) for T_2-weighted images obtained through TurboRARE sequence, the Dice coefficient is over 93%. This suggests that this neural network works very well with T_2-weighted images, which is extremely important, because traditional skull stripping methods are based on T_1-weighted images. On the other hand, for DWI images, the Dice coefficient is already lower and ranges between 42% and 72%. This result is worse, because here is a poorer resolution of diffusion images and the artifacts resulting from the nature EPI sequence. Nevertheless, the obtained results show the usefulness of the deep learning methodology for skull stripping for the future analysis of rats with MCAO model. This method allows for significant reduction of the analysis time and its automation.

In the next stage, volumetric analysis of the first series of rats with MCAO model was performed (these rats were described as MCAO 1-8 and MCAO 0 as a control rat). The T_2-weighted imaging was performed using the TurboRARE sequence in the coronal plane. The first volumetric imaging was performed 24 hours after reperfusion. The approximate stroke volume and the whole brain volume were calculated. The ratio of the ischemic volume to the whole brain volume allowed to create appropriate MRI Stroke Groups, based on the stroke size. The obtained brain volumes are comparable for all rats and range from 1206 mm^3 to 1341 mm^3. All rats were assigned to a group based on the ration of stroke area in brain. In first group, the average stroke size was equaled 57 mm^3, in second group was 187 mm^3 and in third group was 368 mm^3. The obtained results suggest that the obtained rats were very different in terms

of effects of ischemia. Nevertheless from these volumetric measurements the conclusion was that the induction of the MCAO model should be improved to make results more comparable. It is also important to increase the number of animals studied in the future to have higher population. Is is also to note that obtained T_2-weighted images were very good by quality and resolution. In the following measurements, these sequences with these parameters were used as a pilot protocols, but already on three planes: axial, coronal and sagital.

With these pilot protocols in three planes, next step was focused on characterizing the MCAO stroke model. The T_2-weighted imaging was preformed with MSME seqence. Also DWI imaging was performed using DTI_EPI protocol and T_1-weighted imaging was performed using the ASL approach and the FAIR-EPI protocol, which is mainly used for perfusion imaging. Based on the obtained images, it can be seen that the stroke area is brighter on T_1- and T_2-weighted images. For A_0 images in diffusion measurements, the images have T_2-weighted characteristic, which is in accordance with theory in the case of turned off diffusion-sensitizing gradients. With diffusion gradient turned on, a higher contrast between the stroke and healthy tissue is visible, due to the difference in ADC in these areas. Nevertheless this is a kind of qualitative analysis. To perform quantitative analysis, the ADC, T_1, T_2 and perfusion maps were calculated. The T_2 and ADC maps were determined using exponential decay of the signal for each T_E and b-values, respectively. The perfusion map was calculated using T_1-weighted images before and after magnetic labeling of water moelcules in the neck arteries. Comparison of the T_1-weighted images before and after labeling allows to determine the difference in the signal, which in this case is proportional to the perfusion. The obtained results suggest that ADC in the stroke area is lower than in healthy tissue ($ADC_{Stroke} \sim 0.45 * 10^{-3} mm^2/s$, $ADC_{Healthy} \sim 0.8 * 10^{-3} mm^2/s$), the T_2 relaxation time value is higher in the stroke area than in healthy tissue ($T2_{Stroke} \sim 70ms$, $T2_{Healthy} \sim 42ms$) and T_1 relaxation times value is also higher ($T1_{Stroke} \sim 2300ms$, $T1_{Healthy} \sim 1800ms$). The perfusion measurement gave different results, sometimes higher, sometimes lower than in healthy area. This is a direct result of the methodology of MCAO induction. During this operation, after 90 minutes, the filament is removed from the cerebral artery and to maintain homeostasis, the reperfusion occurs, which may proceed differently in each animal. It is also to note that mentioned images were performed 24 hours after the stroke. The perfusion measurements make sense only immediately after the ischemic episode or during it. In clinical applications, diffusion and perfusion measurements are used to find corresponding mismatch, which define the penumbra area [102]. The penumbra area is the area surrounding the core of neurofibrosis and endothelial cell death after ischemic stroke,

where necrosis hasn't occurred due to the presence of collateral circulation. This is a strategic area for stroke therapy, where normal function and circulation should be restored. Additionally, a similar analysis was performed for a control rat, measuring its diffusion, relaxation times and perfusion.

As mentioned earlier, one of the most important parameters in the case of ischemic stroke imaging using MRI is the measurement of ADC diffusion. This measurement allows to determine the area of ischemia and to determine the area of the penumbra. However, it turned out that diffusion in the ischemic area is variable over the time after occlusion. At this stage, another set of MCAO E-G animals was prepared in which the mothod of anethesia during the stroke induction was changed. In this case, ketamine and xylazine was administered together with a low dose of isoflurane during MCAO surgery. This procedure resulted in reproducible strokes, in the same place and comparable size. MRI imaging was performed at 1, 3, 7, 9 and 11 days after reperfusion. Diffusion was measured using a DTI_EPI protocol with $T_E = 20.5$ ms and $T_R = 3000$ ms. Diffusion was measured in 9 directions with five b-values in the range from 200 s/mm^2 to 1500 s/mm^2. Based on the obtained images, ADC maps were calculated for different time intervals after occlusion. On Figure 74, it can be seen that the ADC in the stroke region increases over time. To quantify this, the diffusion was analyzed using a new method using the GMM machine learning model. This model is based on the ADC distribution in the brain, trying to fit a trimodal Gaussian distribution. Trimodal, because the first mode correspondeds to the ischemic region, the second to the healthy area in the brain and finally the third to the CBF area and the stroke scar, which develops over time. This model returns the probability of whether a given pixel belongs to the stroke region (1 component), to the healthy region (2 component) or to CBF/scar (3 component). An example of histogram with the fitted Gaussian is shown in Figure 75. It can be seen that the first stroke component evolves over time and shifts to the right side of the histogram, so the average ADC in the stroke region increases. After about 3-4 days from occlusion, the ADC value in the stroke part increases above in the healthy tissue and the increasement rate begins to be slower. The stroke ADC changes over time from $0.41 * 10^{-3} mm^2/s$ to $0.75 * 10^{-3} mm^2/s$, while in the healthy part it is constant and is equal about $0.65 * 10^{-3} mm^2/s$. Using this model, it is possible to automatically extract the stroke area based only the ADC value. This is extremely interesting, because it is possible to track the progression of ischemia over the time without the presence of human, but automatically. This is an example of unsupervised machine learning, because this tracking is automatically, which is shown in Figure 79. This is a very important tool, because in the future, when theranostic

agent will be administred with a drug, the GMM model will allow for the assessment of the size of ischemia and the effect of a given theranostic on the potential decreasing stroke size.

The idea of theranostics in ischemic stroke is to deliver therapeutic agents through the damages BBB, which occurs in the case of stroke. Currently, for the doctoral dissertation purposes and preliminary research stage, nanoparticles containing only gadolinium in the chemical structure were studied. It was the main source of the contrast in tested nanoparticles. At the preliminary stage, the contrast agent passes through the BBB and accumulates in the stroke area. However, here is a key question - what concentration of gadolinium is detectable in the image using MRI. This is extremely important, because we need to have information about the concentration of gadolinium in nanoparticles, which allows to be visible in the ischemic area using MRI. For this purpose, T_1-weighted imaging of healthy rat was performed before and after the Magnevist contrast agents administration. Based on the obtained images, the T_1 maps were calculated before and after contrast injection. Based on these maps, it can be seen that the contrast agent significantly descreased the T_1 relaxation time in the muscles (from 2500 ms to 1600 ms). In the brain area, the T_1 time didn't change significantly and remained constant about 1800 ms. Based on these maps, it was possible to determine the corresponding the gadolinium concentration. The Figure 81 confirms that the gadolinium concentration in the brain is low at the noise limit, which is consistent with the theory, because BBB is integral in this case. The value of the gadolinium concentration in the brain may be very low here, below the MRI sensitivity, hence the detection limit analysis had to be performed.

In the case of biodistribution studies, the FLASH imaging sequence was used, which depends on sequence parameters such as T_R and FA. Based on the previous results of T_1 in the stroke area, the T_1 time is on average 2300 ms in the stroke. The administered contrast agent should cross BBB in the stroke area and cause descreasement of T_1 relaxation time, thus causing a brighter area in the FLASH image. The limit of detection was determined as a gadolinium concentration in ischemic tissue, which caused a 15% increase in the signal. After determining the FLASH signal amplification curve in function of gadolinium concentration, it can be seen that 15% increase in signal corresponds to 0.03 mM of gadolinium in stroke tissue. This is an extremely important conclusion because future theranostic, in order to be visible using MRI, must have a concentration greater than or equal to 0.03 mM gadolinium. It is also worth to note that nanoparticles dilute in the blood before thay reach the ischemic area, so initial gadolinium concentration in the nanoparticles must be even higher. This studies were performed for the $Magnevist^{TM}$ contrast agent. Therefore, this is an example assessment of minimum gadolinium

concentration. For other contrast agents, this result may be slighty different, but it gave some idea about the range of gadolinium concentration, which is able to be observed in stroke using MRI.

Another important point is the optimization the FLASH sequence for biodistribution studies. As already mentioned, the FLASH signal is dependent on T_R, T_E, FA, T_1 and T_2^*. For a given tissue with a known T_1 and given T_R, the maximum signal is obtained using the Ernst angle. Using this angle as FA, it maximize the signal, but doesn't maximize the contrast in the image of areas with different T_1 values. Assuming that 0.03 mM gadolinium has accumulated in the stroke tissue (which is equivalent to a T_1 relaxation time of 1800 ms), it is possible to plot signal in function of FA for different T_R times, as it has done in Figure 86. In each of the curves, the upper edge corresponds to the relaxation time before contrast administration, while the lower edge after it. It turns out that the maximum contrast is obtained for an angle FA larger than the Ernst angle. For higher T_R values, this contrast obviously increases, at the expense of a longer acquisition time. Therefore it was decided to optimize the FLASH sequence using $T_R = 50$ ms and FA $= 22\ ^o$, taking 250 images every 4.8 seconds. Final biodistribution protocol takes 20 minutes.

The protocol prepared in this way allowed for the study of BBB permeability over time after occlusion. Permeability assessment was based on the analysis of gadolinium concentration maps in the brain, quantitative analysis of gadolinium DCE accumulation curves and determination of K^{trans} coefficients. It turns out that BBB permeability is variable over time after the occurrence of an ischemic episode and is maximal on the third day after stroke. The literature contains information on time intervals, where the BBB is permeable [108], but this assessment was not performed using MRI. The obtained results are consistent, because according to the literature, the first stage of opened BBB occurs a few hours after occlusion and the next window is a few days after stroke - based on studies conducted using MRI, it results that that most permeability of BBB is on the third day after occlusion.

10 Conclusions

This doctoral dissertation aimed to evaluate the theranostic potential of different new nanocarriers in terms of their contrast efficiency for MRI imaging, characterize the MCAO animal model of stroke and establish and optimize mesurement sequences for advanced biodistribution studies of future theranostic nanomaterials.

The first stage of the study was *in vitro* measurements of various nanocarriers. Amoung them, it can be distinguished these nanocarriers based on AOT/PLL and PCL nanocapsules, CQD, POSS and CeO2 nanoparticles. In each case, gadolinium compound was incorporated to chemical structure of the nanoparticle and it was a largely responsible for the MRI contrast properties. Nanocarriers with various ligands were also tested. Summary, the following nanocarriers were tested: AOT/PLL 1xGd, AOT/PLL 2xGd, PCL 1xGd, PCL 2xGD, CQD-Gd, Lactamide POSS-Gd, POSS-Gd in PBS, POSS-Gd in water, POSS, CeO2-Gd, CeO2 and CeO2-Gd-PAA. The contrast properties were obtained using the Solomon-Bloembergen-Morgan theory and determination of molar relaxivities r_1 and r_2. Nanocapsules AOT/PLL and PCL with both one and two gadolinium layers present good contrast properties, comparable to commercially available contrast agents. However, due to the method of synthesis using layer-by-layer method, nanocapsules with one gadolinium layer are easier to prepared as contrast agents for MRI imaging, as well as allows for higer drug load to be carried. This result from fact that during their synthesis and the addition of subsequent layers, the total concentration of nanocapsules in the solution decreases. In the case of POSS nanoparticles, the best results were achieved by Lactamide POSS-Gd. On the other hand, CeO2-Gd showed very good contrast properties described by very high r_1 value. However, the problem here was the high agglomeration of CeO2-Gd, which prevented to use this nanoparticles in *in vivo* conditions. For this reason, CeO2-Gd-PAA nanoparticles were studies, in which this problem was eliminated at the expense of contrast properties. Nevertheless, the final molar relaxivity properties are decent.

The second stage of the doctoral dissertation was focused on results of the *in vivo* animal model of MCAO. This is a model of ischemic stroke in rat brain. The first stage, volumetric analysis was performed, which showed significant differences in stroke size and it stability. These results led to a change in the stroke model induction method. In the next step, T_1, T_2, DWI and PWI imaging were performed to characterize the ischemic area. Skull stripping was also used to extract the brain using the deep learning methodology. It turned out that the accuracy of the neural network brain extraction is very high, about 97%. In the next step, the detection limit of gadolinium in ischemic tissue was tested. It turned out that the minimum gadolinium

concentration in ischemic tissue visible in MRI is about 0.03 mM. Using this knowledge, the standard FLASH sequence was optimize for future biodistribution studies. Next, the temporal evolution of ADC in the stroke brain was studies using the machine learning approach. It turned out that the stroke is very dynamic based on theirs ADC values. The value increases after the ischemic episode, causing creation of stroke scar. The last step was to perform biodistribution studies with the optimized FLASH sequence. Due to this measurements, it was possible to determine the influx mass transfer rate of gadolinium K^{trans} and their evolution over time, which is crucial considering the therapeutic window and BBB permability.

In summary, it has been shown that among the studied theranostic nanocarriers there are those, which generate very good contrast needed for their detection by MRI and that are candidates for theranostic applications. In this case, contrast properties were assessed by calculating specific molar relaxivities r_1 and r_2 and assessment of contrast in MRI images. The MCAO ischemic stroke model and the time evolution of ADC and K^{trans} parameters were also characterized, which are very dynamic. The limit of detection in the ischemic region was also determined and the imaging protocol for biodistribution studies was optimized. Thus, the goal of the doctoral dissertation was achieved.

References

[1] Béjot Y., Bailly H., Durier J., Giroud M., Epidemiology of stroke in Europe and trends for the 21st century, Presse medicale (Paris, France : 1983) vol. 45,12 Pt 2 **2016**: e391-e398. doi:10.1016/j.lpm.2016.10.003

[2] Keeler J., Understanding NMR Spectroscopy, Apollo - University of Cambridge Repository, **2002**, doi:10.17863/CAM.968

[3] Elster A. D., Questions and Answers in MRI: Spin, Available from: https://mriquestions.com/what-is-spin.html

[4] Stachurski K., Zastosowanie metod obrazowania magnetyczno-rezonansowego do oceny zmian w układzie nerwowym w modelu zwierzęcym stwardnienia rozsianego, Master of Science Thesis in Department of Medical Physics and Biophysics AGH University of Science and Technology, **2021**, Cracow

[5] Nathoo N., Yong V. W., Dunn J. F., Understanding disease processes in multiple sclerosis through magnetic resonance imaging studies in animal models, NeuroImage. Clinical vol. 4 743-56. 24 Apr. **2014**, doi:10.1016/j.nicl.2014.04.011

[6] Kaseman D., Ozcan S., Du S., NMR Theory, LibreTexts Chemistry, Available from: https://chem.libretexts.org

[7] Larmor precession, in Wikipedia - The Free Enclycopedia, Available from: https://en.wikipedia.org/wiki/Larmor_precession

[8] Elster A. D., Questions and Answers in MRI: Bloch equations, Available from: https://mriquestions.com/bloch-equations.html

[9] Łopuszyńska N., Magnetic resonance imaging of theranostic drug carriers – from relaxation studies to image contrast assessment, PhD Thesis in the Henryk Niewodniczański Institute of Nuclear Physics Polish Academy of Sciences, **2021**, Available from: https://rifj.ifj.edu.pl/handle/item/360

[10] Elster A. D., Questions and Answers in MRI: T1 Relaxation – Definition, Available from: https://mriquestions.com/what-is-t1.html

[11] Elster A. D., Questions and Answers in MRI: T2 Relaxation - Definition, Available from: https://mriquestions.com/what-is-t2.html

[12] Hornak J. P., The Basics of MRI, Rochester Institute of Technology, **1996**, Available from: https://www.cis.rit.edu/htbooks/mri/

[13] Elster A. D., Questions and Answers in MRI: Fourier Transform (FT), Available from: https://mriquestions.com/fourier-transform-ft.html

[14] Magnetic resonance imaging, in Wikipedia – The Free Encyclopedia, Available from: https://en.wikipedia.org/wiki/Magnetic_resonance_imaging

[15] Hennel J W., Development of NMR methodology and applications, Available from: https://www.ifj.edu.pl/oddzialy/no5/nz56/historia/

[16] Micheau A., Hoa D., MRI instrumentation and MRI safety, IMAIOS: e-MRI, Available from: https://www.imaios.com/en/e-mri/mri-instrumentation-and-mri-safety

[17] Moratal D., Vallés-Luch A., Martí-Bonmatí L., Brummer M., k-Space tutorial: an MRI educational tool for a better understanding of k-space, Biomedical imaging and intervention journal vol. 4,1 **2008**: e15. doi:10.2349/biij.4.1.e15

[18] Ennis D., Hargreaves B., MRI Signals and Sequences, Lecture-02C – k-space and imaging, Stanford University, Available from: https://web.stanford.edu/class/

[19] Elster A. D., Questions and Answers in MRI: k-space, Available from: https://mriquestions.com/what-is-k-space.html

[20] Stingaciu L. R., Characterization of natural porous media by NMR and MRI techniques: High and low magnetic field studies for estimation of hydraulic properties, Available from: https://inis.iaea.org/collection/NCLCollectionStore/_Public/42/103/42103672.pdf?r=1

[21] Tritt-Goc J., Tomografia magnetyczno-rezonansowa, Instytut Fizyki Molekularnej PAN, Poznań, **2007**, Available from: https://foton.if.uj.edu.pl/documents/12579485/f0f454df-ec0d-436b-8e26-75912b98b9e0

[22] Correspondence principle, in Wikipedia – The Free Encyclopedia, Available from: https://en.wikipedia.org/wiki/Correspondence_principle

[23] Magnetization, in Wikipedia – The Free Encyclopedia, Available from: https://en.wikipedia.org/wiki/Magnetization

[24] *ParaVision 7.0 - User Manual*, Bruker Corporation, **2019**

[25] Szczepanowicz K., Procner M., Szczęch M., Łopuszyńska N., Jantas D., Regulska M., Leśkiewicz M., Jasiński K., Stachurski K., Szyk-Warszyńska L., Roman A., Lasoń W., Węglarz W. P., Warszyński P., Polymeric-based theranostic nanocarriers of neuroprotective drugs: development, imaging and bioanalysis, Molecular Pharmaceutics, **2025**, doi.: https://doi.org/10.1021/acs.molpharmaceut.5c00170

[26] Hashemi R. H., Bradley W. G., Lisanti C. J., MRI: The Basics. Second Edition, Lippincott Williams & Wilkins, **2004**

[27] Geraldes Carlos F G C, Laurent S., Classification and basic properties of contrast agents for magnetic resonance imaging, Contrast media & molecular imaging vol. 4,1 **2009**: 1-23. doi:10.1002/cmmi.265

[28] MRI Physics Course Lecture 7, Available from: https://www.youtube.com/watchv=nxQGBYVJumE&list=PLSANNgDr6l7prVZdFx24IxN72x2KwFJhb&index=7

[29] Elster A. D., Questions and Answers in MRI: TR and TE, Available from: https://mriquestions.com/tr-and-te.html

[30] Xiao Y. D., Paudel R., Liu J., Ma C., Zhang Z. S., Zhou S. K., MRI contrast agents: Classification and application (Review), International Journal of Molecular Medicine, **2016**, 1319-1326, doi.: 10.3892/ijmm.2016.2744

[31] Łopuszyńska N., Węglarz W. P., Contrasting Properties of Polymeric Nanocarriers for MRI-Guided Drug Delivery - Review, Nanomaterials **2023**, 13, 2163, https://doi.org/10.3390/nano13152163

[32] I. Solomon, N. Bloembergen, Nuclear Magnetic Interactions in the HF Molecule, The Journal of Chemical Physics **1956**, pp. 261-266, https://doi.org/10.1063/1.1742867

[33] Lauterbur P., Image Formation by Induced Local Interactions: Examples Eploying Nuclear Magnetic Resonance, Nature, **1973**, vol. 242, https://doi.org/10.1038/242190a0

[34] Mansfield P., Grannell P. K., Garroway A. N., Stalker D. C., Multi-Pulse Line Narrowing Experiments: NMR "Diffraction" in Solids?, Pulsed Nuclear Magnetic Resonance and Spin Dynamics in Solids, First Specialized Colloque Ampere Kraków, **1973**

[35] Hennel J. W., Materiały XIX Ogólnopolskiego Seminarium na temat: Magnetycznego Rezonansu Jądrowego i Jego Zastosowań, **1987**, Kraków

[36] Hennel J. W., Wstęp do Teorii Magnetycznego Rezonansu Jądrowego, Wydawnictwo Instytutu Fizyki Jądrowej im. H. Niewodniczańskiego, **1997**, ISBN: 83-902980-7-4

[37] Elster A. D., Questions and Answers in MRI: T1 Relaxation - Definition, Available from: https://mriquestions.com/what-is-t1.html

[38] Bloembergen N., Morgan L. O., Proton Relaxation Times in Paramagnetic Solutions. Effects of Electron Spin Relaxation, J. Chem. Phys. 1 March **1961**; 34 (3): 842–850, https://doi.org/10.1063/1.1731684

[39] Solomon, I. Relaxation Processes in a System of Two Spins, Phys. Rev. **1995**, 99, 559–565, https://doi.org/10.1103/PhysRev.99.559

[40] Caravan P., Ellison J. J., McMurry T. J., Lauffer R. B., Gadolinium(III) Chelates as MRI Contrast Agents: Structure, Dynamics, and Applications, Chemical reviews vol. 99,9 **1999**: 2293-352. doi:10.1021/cr980440x

[41] Bloembergen, N. Spin Relaxation Processes in a Two-Proton System, Phys. Rev. **1956**, 104, 1542–1547, https://doi.org/10.1103/PhysRev.104.1542

[42] Wahsner J., Gale E. M., Rodríguez-Rodríguez A., Caravan P., Chemistry of MRI Contrast Agents: Current Challenges and New Frontiers, Chemical reviews vol. 119,2 **2019**: 957-1057. doi:10.1021/acs.chemrev.8b00363

[43] Tóth, É.; Helm, L.; Merbach, A.E. Relaxivity of MRI Contrast Agents, In Contrast Agents I; Krause, W., Ed.; Topics in Current Chemistry; Springer: Berlin/Heidelberg, Germany, **2002**; Volume 221, pp. 61–101. ISBN 978-3-540-42247-1, doi: 10.1007/3-540-45733-X_3

[44] Elster A. D., Paramagnetic Relaxation, Available from: https://www.mriquestions.com/paramagnetic-relaxation.html

[45] Rohrer M., Bauer H., Mintorovitch J., Requardt M., Weinmann H. J., Comparison of magnetic properties of MRI contrast media solutions at different magnetic field strengths, Investigative radiology vol. 40,11 **2005**: 715-24. doi:10.1097/01.rli.0000184756.66360.d3

[46] Elster A. D., Gadolinium, Available from: https://www.mriquestions.com/why-gadolinium.html

[47] McLachlan A. D., Line widths of electron resonance spectra in solution, Proc. R. Soc. Lond. A 280:271–288 **1964**, http://doi.org/10.1098/rspa.1964.0145

[48] Verwilst, P.; Park, S.; Yoon, B.; Kim, J.S. Recent Advances in Gd-Chelate Based Bimodal Optical/MRI Contrast Agents. Chem. Soc. Rev. **2015**, 44, 1791–1806, https://doi.org/10.1039/C4CS00336E

[49] Knobloch G., Colgan T., Wiens C. N., Wang X., Schubert T., Hernando D., Sharma S. D., Reeder S. B., Relaxivity of Ferumoxytol at 1.5 T and 3.0 T, Investigative radiology vol. 53,5 **2018**: 257-263. doi:10.1097/RLI.0000000000000434

[50] Jung C. W., Jacobs P., Physical and chemical properties of superparamagnetic iron oxide MR contrast agents: ferumoxides, ferumoxtran, ferumoxsil, Magnetic resonance imaging vol. 13,5 **1995**: 661-74. doi:10.1016/0730-725x(95)00024-b

[51] Bernstein M. A., King K. F., Zhou X. J., Handbook of MRI Pulse Sequences. San Diego, CA: Elsevier Academic Press. **2004** p. 960. ISBN 0-12-092861-2 – via archive.org

[52] Weast R. C., Astle M. J., eds., Handbook of Chemistry and Physics. Boca Raton, FL: CRC Press. **1982** p. E66. ISBN 0-8493-0463-6

[53] Elster A. D., MRS of Other Nuclei, Available from: https://mriquestions.com/other-nuclei.html

[54] X. Staal, O. Koshkina and M. Srinivas, "In vivo 19-fluorine magnetic," Fluorine in Life Sciences: Pharmaceuticals, Medicinal Diagnostics, and Agrochemicals, Elsevier Inc., pp. 397-424, 2019

[55] Bober Z., Aebisher D., Ożóg Ł, Tabarkiewicz J., Tutka P., Bartusik-Aebisher D., 19F MRI As a tool for imaging drug delivery to tissue and individual cells, Eur J Clin Exp Med **2017**; 15 (2): 99–109, doi: 10.15584/ejcem.2017.2.2

[56] Flögel U., Ding Z., Hardung H., Jander S., Reichmann G., Jacoby C., Schubert R., Schrader J., In vivo monitoring of inflammation after cardiac and cerebral ischemia by fluorine magnetic resonance imaging, Circulation, **2008** Jul 8;118(2):140-8. doi: 10.1161/CIRCULATIONAHA.107.737890

[57] Vinogradov E., Sherry A. D., Lenkinski R. E., CEST: From basic principles to applications, challenges and opportunities, Journal of Magnetic Resonance, **2013**; 229:155-172. doi:10.1016/j.jmr.2012.11.024

[58] Zhou J., P.C.M. van Zijl, Chemical exchange saturation transfer imaging and spectroscopy, Progress in Nuclear Magnetic Resonance Spectroscopy, 48 **2006** 109 - 136, 10.1016/j.pnmrs.2006.01.001

[59] Gillis P., Moiny F., Brooks R. A., On T2-shortening by strongly magnetized spheres: A partial refocusing model, Magn. Reson. Med. **2002**, 47: 257-263, https://doi.org/10.1002/mrm.10059

[60] Tong S., Hou S., Zheng Z., Zhou J., Bao G., Coating optimization of superparamagnetic iron oxide nanoparticles for high T2 relaxivity, Nano Lett. **2010**;10(11):4607-4613. doi:10.1021/nl102623x

[61] Ashton E. A., Du T., Semi-automated measurement of anatomical structures using statistical and morphological priors, Proc. SPIE 5372, Medical Imaging **2004**: Image Perception, Observer Performance, and Technology Assessment, https://doi.org/10.1117/12.533047

[62] Ruiz-Cabello J., Barnett B. P., Bottomley P. A., Bulte J. W. M., Fluorine (19F) MRS and MRI in biomedicine, NMR in biomedicine vol. 24,2 **2011**: 114-29. doi:10.1002/nbm.1570

[63] Ward K. M., Aletras A. H., Balaban R. S., A New Class of Contrast Agents for MRI Based on Proton Chemical Exchange Dependent Saturation Transfer (CEST), Journal of Magnetic Resonance, Volume 143, Issue 1, **2000**, Pages 79-87, ISSN 1090-7807, https://doi.org/10.1006/jmre.1999.1956

[64] Zhou J., Payen JF, Wilson DA, Traystman RJ, van Zijl PC., Using the amide proton signals of intracellular proteins and peptides to detect pH effects in MRI, Nat Med. **2003**;9(8):1085-1090. doi:10.1038/nm907

[65] Aime S., Castelli D. D, Fedeli F., Terreno E., A Paramagnetic MRI-CEST Agent Responsive to Lactate Concentration, J. Am. Chem. Soc. **2002**, 124, 32, 9364–9365, https://doi.org/10.1021/ja0264044

[66] P. C. N. van Zijl, Yadav N. N., Chemical exchange saturation transfer (CEST): what is in a name and what isn't?, Magn Reson Med. **2011** Apr;65(4):927-48. doi: 10.1002/mrm.22761

[67] Sherry A. D., Woods M., Chemical exchange saturation transfer contrast agents for magnetic resonance imaging, Annu Rev Biomed Eng. **2008**;10:391-411, doi:10.1146/annurev.bioeng.9.060906.151929

[68] Junt I., Nuclear Magnetic Resonance NMR Spectroscopy, Department of Chemistry, University of Calgary, Available from: https://www.chem.ucalgary.ca/courses/353/Carey5th/Ch13/ch13-nmr-1b.html

[69] Elster A. D., Questions and Answers in MRI: Larmor Frequency, Available from: https://mriquestions.com/who-was-larmor.html

[70] Puiseux T., Sewonu A., Moreno R., Mendez S., Nicoud F., Numerical simulation of time-resolved 3D phase-contrast magnetic resonance imaging, Plos One, 16(3), 2021, doi.: 10.1371/journal.pone.0248816

[71] Free induction decay, in Wikipedia, The Free Enclycopedia, Available from: https://en.wikipedia.org/wiki/Free_induction_decay

[72] Micheau A., Hoa D., MRI instrumentation and MRI safety: Magnetic field gradients, IMAIOS: e-MRI, Available from: https://www.imaios.com/en/e-mri/mri-instrumentation-and-mri-safety/magnetic-field-gradients

[73] McRobbie D. W., Fundamentals of MR Imaging, Comprehensive Biomedical Physics, vol. 3, pages: 1 – 19, **2014**, doi.: https://doi.org/10.1016/B978-0-444-53632-7.00301-4

[74] Collins C. M., Fundamentals of MRI-fields and basic pulse sequences, Available from: https://iopscience.iop.org/book/mono/978-1-6817-4083-6/chapter/bk978-1-6817-4083-6ch1

[75] Stingaciu L. R., Characterization of natural porous media by NMR and MRI techniques High and low magnetic field studies for estimation of hydraulic properties, Available from: http://inis.iaea.org/search/search.aspx?orig_q=RN:42103672

[76] Wawrzyn K., A Pseudo Non-Cartesian Pulse Sequence For Hyperpolarized Xenon-129 Gas MRI of Rodent Lungs At Low Magnetic Field Strength, Electronic Thesis and Dissertation Repository 2606, **2014**, https://ir.lib.uwo.ca/etd/2606

[77] McCullough LD., Liu F., Middle cerebral artery occlusion model in rodents: methods and potential pitfalls. J Biomed Biotechnol. **2011**;2011:1–9.

[78] Fluri F., Schuhmann MK., Kleinschnitz C., Animal models of ischemic stroke and their application in clinical research. Drug Des Devel Ther Dove Press. **2015**;9:3445–54.

[79] Bogousslavsky J, Van Melle G, Regli F. The Lausanne Stroke Registry: analysis of 1,000 consecutive patients with first stroke. Stroke J Cereb Circ. **1988**;19(9):1083–92.https://doi.org/10.1161/ 01.STR.19.9.1083

[80] Warzecha A., Sierżęga M., Rozwiązywanie zagadnień pola elektromagnetycznego, Politechnika Krakowska, **2024**, ISBN 978-83-67188-94-4

[81] Lee RM. Morphology of cerebral arteries. Pharmacol Ther. **1995**;149–73.https://doi.org/10.1016/0163-7258(94)00071-A .

[82] Ruben I. Kuzniecky and Graeme D. Jackson, Magnetic Resonance in Epilepsy, **2005**, https://doi.org/10.1016/B978-0-12-431152-7.X5000-9

[83] Minati L., Węglarz W. P., Physical foundations, models, and methods of diffusion magnetic resonance imaging of the brain: A review., Concepts Magn. Reson., **2007**, 30A: 278-307., https://doi.org/10.1002/cmr.a.20094

[84] Elster A. D., Diffusion: Basic, Available from: https://mriquestions.com/diffusion-basic.html

[85] Elster A. D., Functional Imaging, Available from: https://www.mriquestions.com/hellipfunctional-imaging.html

[86] Kiselev V., On the theoretical basis of perfusion measurements by dynamic susceptibility contrast MRI, Magn Reson Med **2001**; 46:1113-1122, 10.1002/mrm.1307

[87] 0stergaard L., Johannsen P., H¢st-Poulsen P., Vestergaard-Poulsen P., Asboe H., Gee A. D., Hansen S. B., Cold G. E., Gjedde A., Gyldensted C., Cerebral Blood Flow Measurements by Magnetic Resonance Imaging Bolus Tracking: Comparison WIth [15O]H2O Positron Emission Tomography in Humans, J Cerebral Blood Flow Metab **1998**; 18:9353-940

[88] Heye A. K., Culling R. D., Valdés Hernández M. C., Thrippleton M. J., Wardlaw J. M., Assessment of blood-brain barrier disruption using dynamic contrast-enhanced MRI. A systematic review, NeuroImage: CLinical **2014**; 6:262-274, http://dx.doi.org/10.1016/j.nicl.2014.09.002

[89] Manning C., Stringer M., Cickie B., Clancy U., et al., Sources of systematic error in DCE-MRI estimation of low-level blood-brain barrier leakage, Magn Reson Med **2021**, 10.1002/mrm.28833

[90] Tofts P. S., Modeling tracer kinetics in dynamic Gd-DTPA MR imaging, J Magn Reson Imaging **1997**; 7:91-101, 10.1002/jmri.1880070113

[91] Borogovac A., Asllani I., Arterial Spin Labeling (ASL) fMRI: Advantages, Theoretical Constrains and Experimental Challenges in Neurosciences, Int J Biomed Imaging **2012**; Article ID 818456:1-13, doi:10.1155/2012/818456

[92] Diebler A.R., Pollock J.M., Kraft R.A., Tan H., Burdette J. H., Maldjian J. A., Arterial spin-labeling in routine clinical practice, Part 1: techniques and artifacts. AJNR Am J Neuroradiol **2008**; 29:1228-1234, 10.3174/ajnr.A1030

[93] Cordes D.B., Lickiss P.D., Rataboul F. Recent Developments in the Chemistry of Cubic Polyhedral Oligosilsesquioxanes. Chem. Rev. **2010**;110:2081–2173. doi: 10.1021/cr900201r

[94] Laine R.M. Nanobuilding blocks based on the [OSiO1.5] (x = 6, 8, 10) octasilsesquioxanes. J. Mater. Chem. **2005**;15:3725–3744. doi: 10.1039/b506815k

[95] Loman-Cortes P., Binte Huq T., Vivero-Escoto J. L., Use of Polyhedral Oligomeric Silsesquioxane (POSS) in Drug Delivery, Photodynamic Therapy and Bioimaging, Molecules **2021**; 26(21): 6453, doi.: 10.3390/molecules26216453

[96] Zavvari F., Nahavandi A., Shahbazi A., Neuroprotective effects of cerium oxide nanoparticles on experimental stress-induced depression in male rats, Journal of Chemical Neuroanatomy **2020**, https://doi.org/10.1016/j.jchemneu.2020.101799

[97] Rzigalinski B. A., Carfagna C. S., Ehrich M., Cerium oxide nanoparticles in neuroprotective and considerations for efficcacy and safety, Wires Nanomedicine and Nanobiotechnology **2016**, https://doi.org/10.1002/wnan.1444

[98] Gubskiy I. L., Namestnikova D. D., Cherkashova E. A., Chekhonin V.P., Baklaushev V. P., Gubsky L. V., Yarygin K. N., MRI Guiding of the Middle Cerebral Artery Occlusion in Rats Aimed to Improve Stroke Modeling. Transl Stroke Res. **2018** Aug;9(4):417-425. doi: 10.1007/s12975-017-0590-y. Epub 2017 Nov 25. PMID: 29178027; PMCID: PMC6061245.

[99] Navya P. N., Kaphle A., Srinivas S. P., Bhargava SK, Rotello V. M, Daima H. K., Current trends and challenges in cancer management and therapy using designer nanomaterials, Nano Converg. **2019** Jul 15;6(1):23. doi: 10.1186/s40580-019-0193-2. PMID: 31304563; PMCID: PMC6626766.

[100] Pomierny B., Krzyżanowska W., Skórkowska A., Jurczyk J., Budziszewska B., Pera J., Chicago Sky Blue 6B Exerts Neuroprotective and Anti-Inflammatory Effects on Focal Cerebral Ischemia, Biomedicine & Pharmacotherapy, 170 (**2024**) 116102, doi: https://doi.org/10.1016/j.biopha.2023.116102

[101] Mansfield P., Multi-Planar Image Formation Using NMR Spin Echoes, J Phys C: Solid State Phys **1977**; 10:L55-L58

[102] Baskerville T. A., McCabe C., Weir C. J., Macrae I. M., Holmes W. M., Noninvasive MRI measurement of CBF: evaluating an arterial spin labelling sequence with 99mTc-HMPAO CBF autoradiography in a rat stroke model, J Cereb Blood Flow Metab. **2012** Jun;32(6):973-7. doi: 10.1038/jcbfm.2012.19. Epub 2012 Apr 4. PMID: 22472604; PMCID: PMC3367221

[103] Lin Y., Ding Y., Chang S., Ge X., Sui X., Jiang Y., RS2-Net: An End-to-End Deep Learning Framework for Rodent Skull Stripping in Multi-Center Brain MRI, NeuroImage, 298 **2024** 120769, doi: https://doi.org/10.1016/j.neuroimage.2024.120769

[104] Sung-Ho L., Woomi B., Yen-Yu Ian S., BrkRaw/bruker: BrkRaw v0.3.3 (software), doi:10.5281/zenodo.3877179

[105] Basverville T. A., McCabe C., Weir C. J., Macrae I. M., Holmes W. M., Noninvasive MRI measurement of CBF: evaluating an ASL sequence with 99mTc-HMPAO CBF in autoradiography in a rat stroke model, J Cereb Blood Flow Metab. **2012** Jun;32(6):973-7. doi: 10.1038/jcbfm.2012.19

[106] Harris A. D., Coutts S. B., Frayne R., Diffusion and perfusion MR imaging of acute ischemic stroke, Magn Reson Imaging Clin N Am. **2009** May;17(2):291-313. doi: 10.1016/j.mric.2009.02.001. PMID: 19406360

[107] Zhang S., Yao Y., Shi J., Tang X., Zhao L., Zhu W., The Temporal Evolution of Diffusional Kurtosis Imaging in an Experimental Middle Cerebral Artery Occlusion (MCAO) Model, Magnetic Resonance Imaging, Vol 37, **2016**, 889-895, doi.: https://doi.org/10.1016/j.mri.2016.04.016

[108] Karin E. Sandoval, Ken A. Witt, Blood-brain barrier tight junction permeability and ischemic stroke, Neurobiology of Disease, Vol. 32, **2008**, doi.: https://doi.org/10.1016/j.nbd.2008.08.005

[109] Magnetic resonance of the free electron, available in LibreTexts Chemistry

[110] Bietenbeck M., Florian A., Sechtem U., Yilmaz A., The diagnostic value of iron oxide nanoparticles for imaging of myocardial inflammation – quo vadis?, J Cardiovasc Magn Reson 17, 54 (**2015**), https://doi.org/10.1186/s12968-015-0165-6

[111] Buckley D.L., Parker G.J.M., Measuring contrast agent concentration in T1-weighted dynamic contrast-enhanced MRI, Dynamic Contrast-Enhanced Magnetic Resonance Imaging in Oncology, Springer, Berlin, pp. 69-79, **2005**